1-4-2017

Three-Dimensional Manganese Oxide Nanoarray-Based Monolithic Catalysts for Exhaust Gas Treatment

Sheng-Yu Chen
University of Connecticut, csylqy@gmail.com

Three-Dimensional Manganese Oxide Nanoarray-Based Monolithic Catalysts for Exhaust Gas Treatment

Sheng-Yu Chen, Ph.D.

University of Connecticut, 2017

This study focused on the design and synthesis of manganese oxide nanomaterials with nanoarray architectures. First of all, a straightforward synthetic strategy was discovered to fabricate manganese oxide nanoarrays on two-dimensional substrates (e.g. Si wafers and conductive FTO glass). Then, the generic one-pot hydrothermal synthesis route has been successfully utilized to in-situ grow uniform manganese oxide nanoarrays onto the cordierite honeycomb monolithic substrates, forming a series of nanoarray-based monolithic catalysts with different morphology, surface area, and reactivity of carbon monoxide (CO) oxidation., denoted as HM-DCM, HM-PCR, and HM-PSF, respectively. Next, copper manganese oxide ($CuMn_2O_4$) was combined with the manganese oxide nanoarray-based monolithic catalysts to enhance reactivity. Nanosheet layers of $CuMn_2O_4$ were uniformly coated onto the manganese oxide nanoarrays (HM-PCR). Compared to traditional monolithic catalysts with alumina support, the benefit of nanoarray morphology was demonstrated by correlating the variation of surface area with the reactivity. The incorporation of cobalt ions promoted the higher surface area and C_3H_8 conversion as well. Last but not least, a continuous flow synthesis system was attempted to scale-up the size of manganese oxide nanoarray-based monolithic catalysts. Overall, the straightforward synthetic processes of nanoarrays and transition metal oxide coatings show a scalable, low-cost, and template-free method to fabricate monolithic catalysts for exhaust treatment.

Three-Dimensional Manganese Oxide Nanoarray-Based Monolithic Catalysts for Exhaust Gas Treatment

Sheng-Yu Chen

B.S., National Central University, Taiwan, 2004

M.S., National Central University, Taiwan, 2007

A Dissertation

Submitted in Partial Fulfillment of the

Requirements for the Degree of

Doctor of Philosophy

at the

University of Connecticut

2017

APPROVAL PAGE

Doctor of Philosophy Dissertation

Three-Dimensional Manganese Oxide Nanoarray-Based Monolithic Catalysts for Exhaust Gas Treatment

Presented by

Sheng-Yu Chen, M.S.

Major Advisor _____

Steven L. Suib

Associate Advisor _____

Alfredo Angeles-Boza

Associate Advisor _____

Jie He

Associate Advisor _____

Pu-Xian Gao

Associate Advisor _____

Fatma Selampinar

University of Connecticut
2017

Dedicated to my whole family and all my friends

Acknowledgement

I would like to express my sincere gratitude to my advisor Prof. Steven Suib for his generous support of my Ph.D. study and related research, for his patience, motivation, and immense knowledge. His guidance helped me in all the time of research and writing of this thesis. I could never have imagined having a better advisor and mentor for my Ph.D. study.

Besides my advisor, I would like to thank my thesis committee: Prof. Pu-Xian Gao, Prof. Alfredo Angeles-Boza, Prof. Jie He, and Dr. Fatma Selampinar, for their insightful comments and encouragement, but also for the hard questions led me to widen my research from various perspectives. I also thank the chemistry department staffs, Charlene Fuller, Dan Daleb, Emilie Hogrebe, and Dr. You-Jun Fu.

My sincere thanks also goes to Prof. Mu-Ping Nieh, Prof. Chun-Hu Chen, Dr. Francis Galasso, Dr. Hui-Jan Lin, Dr. Ching-Chang Chung, Dr. Chung-Hao Kuo, Dr. Sourav Biswas, Dr. Altug Poyraz, Dr. Zhu Luo, Dr. Wenxiang Tang, Dr. Yanbing Guo, and Dr. Wenqiao Song, who provided me lots of help and collaboration works. I also thank Dr. Marie Cantino, Dr. Xuan-Hao Sun, and Bruce Goodwin for the SEM guidance. Without their precious support, it would not be possible to conduct this research.

I thank my fellow labmates, Ran Miao, Junkai He, Wei Zhong, and Sibo Wang for the stimulating discussions. I am also grateful to Dr. Ming-Chou Chen and Dr. Jiann-T'suen for kindly suggestions and encouragement. Special appreciation to my friends, Dr. Guan-Ting Liao, Dr. Gong-Yi Liao, Dr. Chung Huang, Dr. Wei-Hao Hsu, Chia-Lin Lin, Dr. Dong-Yuan Chen, Hong-Ping Chen, Yi-Syong Huang, Jih-Hsin Chen, Shun-Jie Dai, Chuan-Fang Li, Eason Huang, Yue-Chi Kuo, Dr. Chun-Chih Chang, Yang-Che Liu, Szu-Jui Wu, and all their families.

My deepest gratitude goes to my family, my parents and my brother for supporting me all the time. My deepest appreciation goes to my lovely wife, Ching-Yang Liu, and two kids, Mu-Ja Chen and Mu-Fan Chen, you all complete my life.

Table of Contents

List of Figures

List of Tables

Chapter 1. Introduction

1.1 Aim of Thesis

Deteriorating air pollution is a long-term issue threatening the atmospheric quality and human health.[1] The rapidly decayed air quality due to the fast growth of human activities and industrial development urged each government to legislate stricter regulations for emissions control.[2] However, improvements in extracting shale oil and lowering the price of petroleum also stimulated the daily global consumption of fossil fuels which keeps increasing sharply. The growing demands of fossil fuel reveals the significance of exhaust treatment to reduce the air pollution from automobiles and factories.[3] This challenges the auto industry to develop more efficient catalysts for toxic substances from automobile exhaust, one main source of air pollution, e.g. carbon monoxide (CO), nitrogen oxides (NO_x), sulfur oxides (SO_x), and hydrocarbons (HC).[4] Therefore, state-of-art platinum-group metal (PGM)-based (e.g. Pd, Pt, Rh) catalytic converters face more difficult challenges for a balance between catalytic efficiency and material cost.[5-7] Introducing transition metal oxides (e.g. MnO_2, Co_3O_4, CuO, and CeO_2) is a cost-effective mainstream strategy to improve catalytic converters with enhanced surface area, porosity, reactivity, and thermal stability.[8-11] Perovskite materials also reveal an outstanding conversion of automobile exhaust and positive synergetic effects with noble metals.[12,13]

In this thesis, the major study focused on the design and synthesis of manganese oxide nanomaterials with nanoarray architecture for air purification and exhaust treatment. Compared to traditional powder based catalysts, the design of nanoarray-based catalysts will provide an open surface feature for higher dynamic molecular transfer of reacting gas.[14,15] A general strategy of

synthesizing urchin-like manganese oxide nanoparticles was proposed to form uniform coatings of manganese oxide nanoarrays on diverse substrates, i.e. silicon wafers, fluorine-doped tin oxide glass (FTO), carbon foams, and cordierite honeycomb monoliths. To the best of our knowledge, only a few studies revealed synthetic procedures and applications of manganese oxide nanoarrays as electrochemical supercapacitors and hydrophobic surface coating.[16-18] Gaseous catalytic oxidations, i.e. carbon monoxide (CO) and propane (C_3H_8), will be conducted to evaluate the reactivity of nanoarrays based monolithic catalysts for synthetic optimization. Incorporation of different transition metals into the manganese oxide crystal structure will be able to enhance catalytic reactivity, thermal stability and fabrication rate of nanoarrays.[19,20] Also, a continuous flow synthetic system will be built up to scale-up the hydrothermal synthesis and reach the goal of commercializing the nanoarray-based monolithic catalysts for the automotive industry.

1.2 Manganese Oxide Octahedral Molecular Sieves (OMS) Materials

As one of the most abundant metals in Earth's crust, manganese oxides have attracted a great deal of attention due to their diverse crystal structures, outstanding chemical reactivity, extensive applications, relatively low cost, and structural porosity. Porosity is one important character for nanomaterials applied in specific fields, like heterogeneous catalysis, energy storage, environmental treatments, and sensors, by efficiently increasing surface area and reaction selectivity. Using edge- and corner-shared (MnO_6^{x-}) octahedra as the basic building blocks, various manganese oxide structures are formed with metal cation-stabilized (e.g. K^+, Na^+, and Mg^{2+}) tunnel structures as known as the series of octahedral molecular sieves (OMS).[21-23] As shown in **Figure 1.1,** the series of manganese oxide octahedral molecular sieves (OMS) nanomaterials are well-

studied and applied in industry for decades, e.g. todorokite (OMS-1), cryptomelane (OMS-2), pyrolusite (OMS-7), and birnessite (OL-1).[24,25]

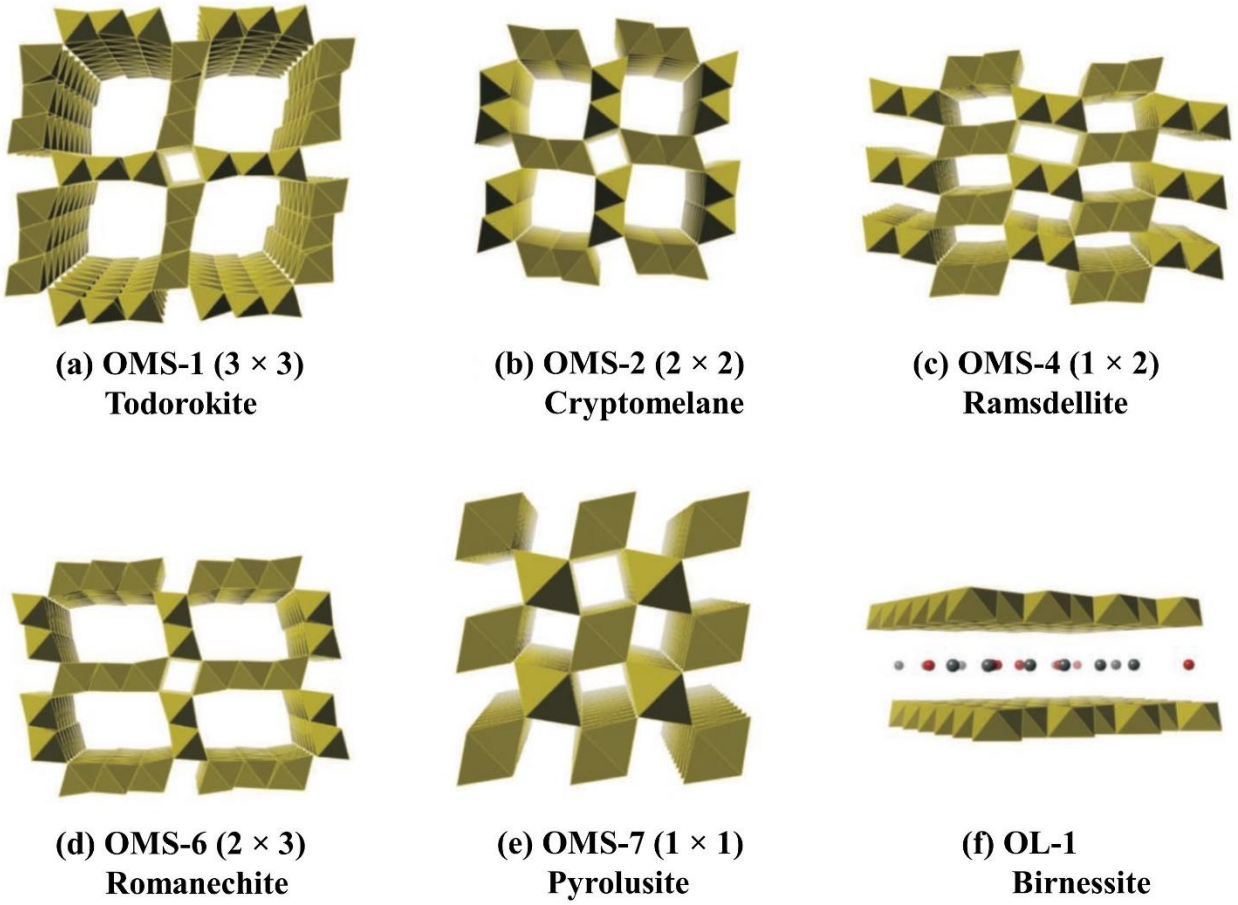

Figure 1.1 Schematic crystal structures of manganese oxide OMS and OL series materials.

Cryptomelane manganese oxide with 2 × 2 tunnels (OMS-2) is a well-known active nanomaterial due to simple synthesis, controllable morphologies, high catalytic performance and selectivity, and widely applications.[26-31] Diverse synthetic approaches have been studied to synthesize cryptomelane manganese oxide in nanoscale. De Guzman et al. used reflux method to produce OMS-2 from Mn^{2+} and Mn^{7+} precursors.[32,33] Giraldo et al. used the sol-gel method and

tetramethyl ammonium (TMA^+) permanganate salts as precursors to self-assemble OMS-2 helices [**Figure 1.2(a)**].[34] Yuan et al. used hydrothermal synthesis at 120°C to obtain cryptomelane nanorods-based urchin-like OMS-2 nanoparticles and ultra-long OMS-2 nanofibers [**Figure 1.2(b)**].[35-37] Lei et al. converted birnessite manganese oxide (OL-1) to cryptomelane (OMS-2) by high-temperature calcination (800°C) [**Figure 1.2(c)**].[38,39] Dharmarathna et al. combined the sonochemical method and cosolvent system to produce OMS-2 nanomaterials with shorter lengths and high surface area [**Figure 1.2(d)**].[40] Huang et al. used microwave reactor to assist the hydrothermal synthesis of OMS-2 [**Figure 1.2(e)**].[26,41] Espinal et al. conducted pulsed-laser deposition (PLD) of OMS-2 on strontium titanate substrates to form cryptomelane manganese oxide with nanostructured array architectures [**Figure 1.2(f)**].[42,43]

Cryptomelane OMS-2 has also been applied in many different areas. As a heterogeneous catalyst, OMS-2 exhibited high conversion and selectivity in organic oxidative reactions, e.g. alcohol oxidation, cyclohexane oxidation, ketone formation, and imine formation.[44-48] For environmental protection, OMS-2 possesses outstanding activity for gaseous treatment, e.g. CO oxidation and volatile organic compounds (VOCs) oxidation, and water treatment, e.g. dye-degradation and oil spill cleanup.[49-54,31] Manganese oxide nanomaterials are considered to be the electrode material for energy storage, i.e supercapacitor.[55-59] Recently, some researches revealed OMS-2 based materials with good potential to be an efficient catalyst for water splitting as well.[60,29]

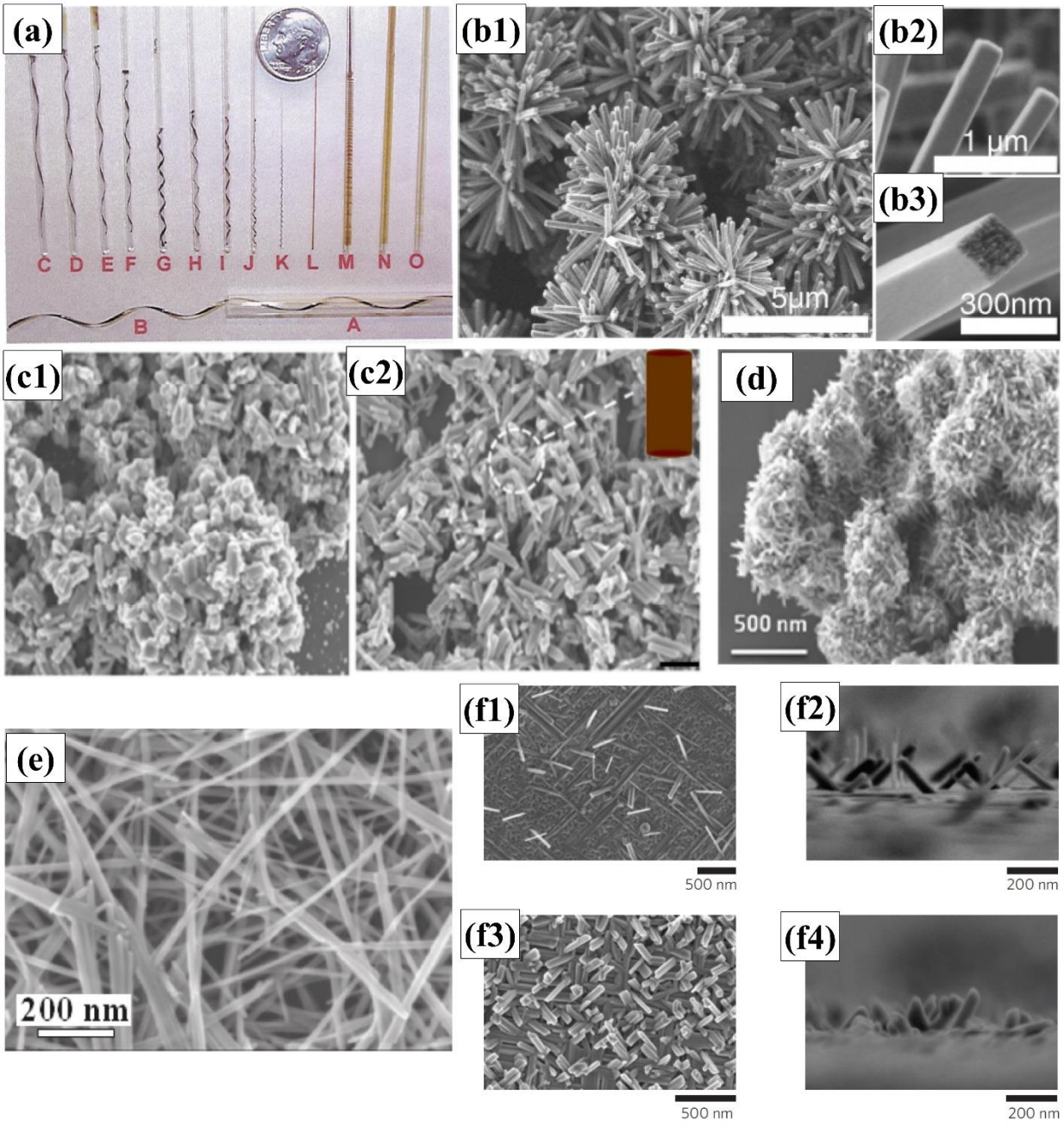

Figure 1.2 (a) Morphology of self-assembled OMS-2 helices.[34] SEM images of (b) OMS-2 urchin-like nanoparticles composed of nanotetragonal prisms obtained from hydrothermal;[37] (c) OMS-2 short rods converted at 500°C;[38] (d) OMS-2 materials prepared by sonochemical method;[40] (e) OMS-2 nanofibers prepared by microwave-assisted hydrothermal synthesis;[26] (f) OMS-2 nanostructured array deposited on a single crystal STO substrate by PLD at 600°C.[43]

1.3 Three-Dimensional (3D) Manganese Oxide Nano-Arrays

During the past decades, one-dimensional (1D) fiber-, wire-, belt-, and rod-like nanomaterials have received great interests and studies due to the special properties, e.g., organized morphology, high surface-to-volume ratio, open surface, limited electron transfer route, high crystallinity, and extensive processability, which contributing to outstanding chemical reactivity, sensitivity, and conductivity.[61,62] Three-dimensional (3D) nanoarrays composed of 1D based nanoparticles have been successfully fabricated using various single metal oxides (e.g., ZnO, TiO_2, Fe_2O_3, and MnO_2),[63-66] mixed metal oxide (e.g., $PbTiO_3$ and $ZnCo_2O_4$),[67,68] and bi-phase metal oxides (e.g., ZnO/MnO_2 and V_2O_5/TiO_2).[69,70] They have shown unique properties such as high surface area, tunable semi-conductivity, field-emission, and easy control of energy transport, as well as amenability to scalable thin-film coating and coaxial deposition. Widespread applications using 3D nanoarrays were reported as solar cells, sensors, field emission transistors, electrochemical capacitors, and water splitting catalysts, etc.[71-75]

Some synthetic methods have been reported to fabricate array structures of manganese oxide rod arrays, with the most popular ones being electrochemical deposition, hydrothermal, and pulsed laser deposition (PLD). The electrochemical deposition route usually involves templates such as anodic aluminum oxide (AAO), carbon nanotube (CNT), and metal oxide nanowires (*e.g.* ZnO and Co_3O_4) to synthesize nanoarray structures. Those fabrication method using varied templates can obtain well-aligned manganese oxide nanoarrays with the requirement of multiple experimental steps. Cui et al. and Liu et al. deposited MnO_2 on the CNT arrays synthesized by chemical vapor deposition (PE-CVD) to form manganese oxide coated CNT arrays.[76,77] Duay et al., Xu et al., and Kim et al. fabricated vertical arrays of MnO_2 with AAO templates for electrochemical capacitors and cathode materials for Li-ion batteries.[78-80] Sun et al. and Liu et al.

coated MnO_2 on ZnO and Co_3O_4 nanowire arrays, respectively, to synthesize manganese oxide arrays with core/shell structures.[81,82] Electrodeposition is a mature technique and able to grow manganese oxides arrays on most conductive substrates, e.g. Pt foils, Ni foams, and conductive glass. Several manganese oxide nanowire arrays have been fabricated by electrodeposition and applied as heterogeneous catalysts for oxygen evolution reduction (OER) and electrodes for supercapacitors and Li-ion batteries.[83-86] As another common method, PLD fabrication of manganese oxide nanoarrays involves the use of costly strontium titanate ($SrTiO_3$) substrates and expensive equipment.[43]

Therefore, facile, cost-effective, and template-free methods are in great demand. However, very limited success has been reported in fabricating manganese oxide rod arrays using non-electrochemical solution chemistry such as hydrothermal deposition.[30] On the other hand, although manganese oxide nanomaterials with array structures had been applied as supercapacitor electrodes and electrocatalysts for water splitting, little has been done through hydrothermal synthesis.[83,87]

1.4 Catalytic converters in automobile for Exhaust Treatment

In catalytic converters, the ceramic cordierite ($2MgO \cdot 2Al_2O_3 \cdot 5SiO_2$) honeycomb monolith is one of the standard substrates for several decades due to its outstanding thermal and mechanical durability, low-pressure-drop, and large open frontal area.[88] In general, slurry wash-coating is an effective and widely-used method to deposit metal or metal oxides on the honeycomb monoliths.[89-92] Incorporation of a mesoporous support like γ-Al_2O_3, and platinum-group-metals (PGM) as active materials, like Pt and Pd, on the cordierite substrates were demonstrated to obtain efficient catalytic

performance for exhaust from incomplete combustion in vehicles and industrial processes, such as carbon monoxide (CO), nitrogen oxide (NO_x), and hydrocarbons (HCs).[93-95,92] Nevertheless, wash-coating based catalysts using powdered structural materials still have some issues that need to be overcome, such as uniformity, coating adhesion effected by size, and usage of noble metals.[14] (i) thicker coating layers are usually observed around the corners than the middle parts of monolith channels.[90] (ii) The size of nanoparticles bigger than 2 μm led to much lower adhesion if no binder was applied.[96] (iii) Loading with platinum-group-metal (PGM) materials increases the overall cost. Therefore, nanomaterials with rod array structures were designed as a powerful alternative to overcome the afore-mentioned problems.

1.5 Copper Manganese Oxide and Hopcalite Catalysts

In industry, copper-manganese mixed oxides were widely used as heterogeneous catalysts with remarkable reactivity at low temperature for several decades.[97-101] Among the various copper manganese oxides, Hopcalite ($CuMn_2O_4$) with spinel structure, is well-known due to the high capability of CO oxidation at low temperature and cheap cost.[97,100,102] The reactivity of copper manganese oxide systems is varied depending on several factors as elemental composition, crystal structure, calcination temperature, surface area, and aging.[97,103-105] The respective reduction of Cu^{2+} and oxidation of Mn^{3+} to Cu^{+} and Mn^{4+} ($Cu^{2+} + Mn^{3+} \rightarrow Cu^{+} + Mn^{4+}$) were commonly proposed as the main factor of high reactivity.[97,101,102] In general, amorphous $CuMn_2O_4$ is considered as the most active copper manganese oxide phase. Partially replacing the tetrahedral site in spinel AB_2O_4 by different transition metals (e.g. Co, Ni, Fe, and Au) might promote the catalytic performance due to enhanced surface lattice oxygen mobility.[103,106]

1.6 Nanoarray-Based Monolithic Catalysts for Exhaust Treatment

Gao and co-workers have developed a series of monolithic nano-array based metal oxide catalysts with uniform nanorods, nanowires, and core-shell nanorod structures exhibiting efficient low-temperature oxidation of carbon monoxide (CO), methane (CH_4), propane (C_3H_8), and nitric oxide (NO) which demonstrates an advanced approach for catalyst fabrication..[14,107-109] In their previous researches, ZnO, TiO_2, CeO_2, and Co_3O_4 with well-defined nanoarray architectures were in situ grown on cordierite and stainless steel honeycomb monoliths and uniformly covered the surface of substrates.[14]

Pt-loaded ZnO nanoarrays display tunable heights between 1 ~ 5 μm with lower light-off temperature (T_{50}) and full conversion temperature (T_{100}) than the powder-based Pt/ZnO catalysts.[14] Uniform Co_3O_4 nanoarrays with average height 10 μm presented outstanding reactivity of CO, NO, and CH_4 oxidations and better catalytic performance than the correlated powder-based Co_3O_4 catalysts.[15,110] The nanoarrays with core/shell structures were revealed by depositing perovskite on ZnO nanoarrays.[111] The ZnO nanoarrays maintained identical morphologies after wash-coating of $LaBO_3$ (B = Co, Ni, and Mn) layers and exhibited enhanced the catalytic performance of propane (C_3H_8) oxidations than the $LaBO_3$ wash-coated cordierite catalysts.[109]

Compared to the wash-coating method, the nanoarrays system exhibited unique features because of the nanoarray architectures. (i) The self-supported nanoarrays have no need of porous alumina powder as supports and reduce the overall weight of monolithic catalysts.[14] (ii) vertical-aligned nanoarrays provide open surfaces for efficient molecular diffusion improving heterogeneous interactions.[109] (iii) Uniform nanoarray coatings with thinner thickness (1-10 μm) inside honeycomb channels than the general active layers in wash-coated catalysts (20-100 μm) avoid additional pressure-drop.[15] (iv) Well-bound nanoarrays on the substrate surface prevent self-

agglomeration at a higher temperature.[111] These characters open potential for applying transition metal oxide nanoarrays on catalytic converters.

1.7 References

(1) *Unep Year Book 2014 Emerging Issues Update - Air Pollution: World's Worst Environmental Health Risk*, United Nations Environment Programme, 2014.

(2) *Adoption of the Paris Agreement*, UNFCCC. Conference of the Parties (COP), 2015.

(3) *Short-Term Energy Outlook June 2015. Http://Www.Eia.Gov/Forecasts/Steo/ (Accessed Jun 11, 2015)*, U.S. Energy Information Administration (EIA).

(4) Pihl, J. A.; Blint, R.; Daw, C. S., *2015 Cleers Industry Priorities Survey Final Report*, U.S. Department of Energy, Advanced Engine Cross-Cutting Technology Development Team, 2016.

(5) Farrauto, R. J.; Hobson, M.; Kennelly, T.; Waterman, E. *Appl. Catal., A* **1992**, *81*, 227-237.

(6) Salasc, S.; Skoglundh, M.; Fridell, E. *Appl. Catal., B* **2002**, *36*, 145-160.

(7) Schoenberger, R., *Getting Platinum out of Catalytic Converters*, 2015, http://www.todaysmotorvehicles.com/article/tmv0915-catalytic-converters-platinum/, Nov 12, 2016

(8) Song, W.; Poyraz, A. S.; Meng, Y.; Ren, Z.; Chen, S.-Y.; Suib, S. L. *Chem. Mater.* **2014**, *26*, 4629-4639.

(9) Xia, G.; Yin, Y.; Willis, W.; Wang, J.; Suib, S. *J. Catal.* **1999**, *185*, 91-105.

(10) Yang, J. S.; Jung, W. Y.; Lee, G. D.; Park, S. S.; Jeong, E. D.; Kim, H. G.; Hong, S.-S. *J. Ind. Eng. Chem.* **2008**, *14*, 779-784.

(11) Yao, H.; Yao, Y. Y. *J. Catal.* **1984**, *86*, 254-265.

(12) Kim, C. H.; Qi, G.; Dahlberg, K.; Li, W. *Science* **2010**, *327*, 1624-1627.

(13) Nishihata, Y.; Mizuki, J.; Akao, T.; Tanaka, H.; Uenishi, M.; Kimura, M.; Okamoto, T.; Hamada, N. *Nature* **2002**, *418*, 164-167.

(14) Guo, Y.; Ren, Z.; Xiao, W.; Liu, C.; Sharma, H.; Gao, H.; Mhadeshwar, A.; Gao, P.-X. *Nano Energy* **2013**, *2*, 873-881.

(15) Ren, Z.; Botu, V.; Wang, S.; Meng, Y.; Song, W.; Guo, Y.; Ramprasad, R.; Suib, S. L.; Gao, P.-X. *Angew. Chem. Int. Ed. Engl.* **2014**, *53*, 7223-7227.

(16) Lu, X.; Zheng, D.; Zhai, T.; Liu, Z.; Huang, Y.; Xie, S.; Tong, Y. *Energy. Environ. Sci.* **2011**, *4*, 2915-2921.

(17) Yu, M.; Zhai, T.; Lu, X.; Chen, X.; Xie, S.; Li, W.; Liang, C.; Zhao, W.; Zhang, L.; Tong, Y. *J. Power Sources* **2013**, *239*, 64-71.

(18) Zhao, X.-D.; Fan, H.-M.; Luo, J.; Ding, J.; Liu, X.-Y.; Zou, B.-S.; Feng, Y.-P. *Adv. Funct. Mater.* **2011**, *21*, 184-190.

(19) Chen, H.; Tong, X.; Li, Y. *Appl. Catal., A* **2009**, *370*, 59-65.

(20) Jones, C.; Taylor, S. H.; Burrows, A.; Crudace, M. J.; Kiely, C. J.; Hutchings, G. J. *Chem. Commun.* **2008**, 1707-1709.

(21) Brock, S. L.; Duan, N.; Tian, Z. R.; Giraldo, O.; Zhou, H.; Suib, S. L. *Chem. Mater.* **1998**, *10*, 2619-2628.

(22) McKenzie, R. *Mineralogical Magazine* **1971**, *38*, 493-502.

(23) Pasero, M. *Rev. Mineral. Geochem.* **2005**, *57*, 291-305.

(24) Chen, C. H.; Suib, S. *J. Chin. Chem. Soc.* **2012**, *59*, 465-472.

(25) Suib, S. L. *Acc. Chem. Res.* **2008**, *41*, 479-487.

(26) Huang, H.; Sithambaram, S.; Chen, C.-H.; King'ondu Kithongo, C.; Xu, L.; Iyer, A.; Garces, H. F.; Suib, S. L. *Chem. Mater.* **2010**, *22*, 3664-3669.

(27) Li, L.; Nan, C.; Lu, J.; Peng, Q.; Li, Y. *Chem. Commun.* **2012**, *48*, 6945-6947.

(28) Makwana, V. D.; Son, Y.-C.; Howell, A. R.; Suib, S. L. *J. Catal.* **2002**, *210*, 46-52.

(29) Meng, Y.; Song, W.; Huang, H.; Ren, Z.; Chen, S.-Y.; Suib, S. L. *J. Am. Chem. Soc.* **2014**, *136*, 11452-11464.

(30) Son, Y. C.; Makwana, V. D.; Howell, A. R.; Suib, S. L. *Angew. Chem.* **2001**, *113*, 4410-4413.

(31) Yuan, J.; Liu, X.; Akbulut, O.; Hu, J.; Suib, S. L.; Kong, J.; Stellacci, F. *Nat. Nanotechnol.* **2008**, *3*, 332-336.

(32) De Guzman, R. N.; Shen, Y. F.; Shaw, B. R.; Suib, S. L.; O'Young, C. L. *Chem. Mater.* **1993**, *5*, 1395-1400.

(33) DeGuzman, R. N.; Shen, Y.-F.; Neth, E. J.; Suib, S. L.; O'Young, C.-L.; Levine, S.; Newsam, J. M. *Chem. Mater.* **1994**, *6*, 815-821.

(34) Giraldo, O.; Brock, S. L.; Marquez, M.; Suib, S. L.; Hillhouse, H.; Tsapatsis, M. *Nature* **2000**, *405*, 38.

(35) Li, W. N.; Yuan, J.; Shen, X. F.; Gomez- Mower, S.; Xu, L. P.; Sithambaram, S.; Aindow, M.; Suib, S. L. *Adv. Funct. Mater.* **2006**, *16*, 1247-1253.

(36) Yuan, J.; Laubernds, K.; Villegas, J.; Gomez, S.; Suib, S. L. *Adv. Mater.* **2004**, *16*, 1729-1732.

(37) Yuan, J.; Li, W.-N.; Gomez, S.; Suib, S. L. *J. Am. Chem. Soc.* **2005**, *127*, 14184-14185.

(38) El-Sawy, A. M.; King'ondu, C. K.; Kuo, C.-H.; Kriz, D. A.; Guild, C. J.; Meng, Y.; Frueh, S. J.; Dharmarathna, S.; Ehrlich, S. N.; Suib, S. L. *Chem. Mater.* **2014**, *26*, 5752-5760.

(39) Jin, L.; Reutenauer, J.; Opembe, N.; Lai, M.; Martenak, D. J.; Han, S.; Suib, S. L. *ChemCatChem* **2009**, *1*, 441-444.

(40) Dharmarathna, S.; King'ondu, C. K.; Pedrick, W.; Pahalagedara, L.; Suib, S. L. *Chem. Mater.* **2012**, *24*, 705-712.

(41) Pahalagedara, L.; Dharmarathna, S.; King'ondu, C.; Pahalagedara, M.; Meng, Y.; Kuo, C.-H.; Suib, S. *J. Phys. Chem. C* **2014**, *118*, 20363-20373.

(42) Espinal, A. E.; Yan, Y.; Zhang, L.; Espinal, L.; Morey, A.; Wells, B. O.; Aindow, M.; Suib, S. L. *Small* **2014**, *10*, 66-72.

(43) Espinal, A. E.; Zhang, L.; Chen, C.-H.; Morey, A.; Nie, Y.; Espinal, L.; Wells, B. O.; Joesten, R.; Aindow, M.; Suib, S. L. *Nat. Mater.* **2010**, *9*, 54-59.

(44) Cao, H.; Suib, S. L. *J. Am. Chem. Soc.* **1994**, *116*, 5334-5342.

(45) Iyer, A.; Galindo, H.; Sithambaram, S.; King'ondu, C.; Chen, C.-H.; Suib, S. L. *Appl. Catal., A* **2010**, *375*, 295-302.

(46) Kumar, R.; Sithambaram, S.; Suib, S. L. *J. Catal.* **2009**, *262*, 304-313.

(47) Opembe, N. N.; Son, Y. C.; Sriskandakumar, T.; Suib, S. L. *ChemSusChem* **2008**, *1*, 182-185.

(48) Sithambaram, S.; Ding, Y.; Li, W.; Shen, X.; Gaenzler, F.; Suib, S. L. *Green Chemistry* **2008**, *10*, 1029-1032.

(49) Chen, C.-H.; Njagi, E. C.; Chen, S.-Y.; Horvath, D. T.; Xu, L.; Morey, A.; Mackin, C.; Joesten, R.; Suib, S. L. *Inorg. Chem.* **2015**, *54*, 10163-10171.

(50) Ching, S.; Kriz, D. A.; Luthy, K. M.; Njagi, E. C.; Suib, S. L. *Chem. Commun.* **2011**, *47*, 8286-8288.

(51) Genuino, H. C.; Dharmarathna, S.; Njagi, E. C.; Mei, M. C.; Suib, S. L. *J. Phys. Chem. C* **2012**, *116*, 12066-12078.

(52) Genuino, H. C.; Meng, Y.; Horvath, D. T.; Kuo, C. H.; Seraji, M. S.; Morey, A. M.; Joesten, R. L.; Suib, S. L. *ChemCatChem* **2013**, *5*, 2306-2317.

(53) Njagi, E. C.; Genuino, H. C.; King'ondu, C. K.; Dharmarathna, S.; Suib, S. L. *Appl. Catal., A* **2012**, *421*, 154-160.

(54) Sriskandakumar, T.; Opembe, N.; Chen, C.-H.; Morey, A.; King'ondu, C.; Suib, S. L. *J. Phys. Chem. A* **2009**, *113*, 1523-1530.

(55) Chen, S.; Zhu, J.; Han, Q.; Zheng, Z.; Yang, Y.; Wang, X. *Cryst. Growth Des.* **2009**, *9*, 4356-4361.

(56) Ragupathy, P.; Park, D. H.; Campet, G.; Vasan, H.; Hwang, S.-J.; Choy, J.-H.; Munichandraiah, N. *J. Phys. Chem. C* **2009**, *113*, 6303-6309.

(57) Truong, T. T.; Liu, Y.; Ren, Y.; Trahey, L.; Sun, Y. *ACS nano* **2012**, *6*, 8067-8077.

(58) Yu, P.; Zhang, X.; Wang, D.; Wang, L.; Ma, Y. *Cryst. Growth Des.* **2008**, *9*, 528-533.

(59) Zhang, X.; Sun, X.; Zhang, H.; Zhang, D.; Ma, Y. *Electrochim. Acta* **2013**, *87*, 637-644.

(60) Iyer, A.; Del-Pilar, J.; King'ondu, C. K.; Kissel, E.; Garces, H. F.; Huang, H.; El-Sawy, A. M.; Dutta, P. K.; Suib, S. L. *J. Phys. Chem. C* **2012**, *116*, 6474-6483.

(61) Hochbaum, A. I.; Yang, P. *Chem. Rev.* **2009**, *110*, 527-546.

(62) Xia, Y.; Yang, P.; Sun, Y.; Wu, Y.; Mayers, B.; Gates, B.; Yin, Y.; Kim, F.; Yan, H. *Adv. Mater.* **2003**, *15*, 353-389.

(63) Espinal, A. E.; Zhang, L.; Chen, C. H.; Morey, A.; Nie, Y.; Espinal, L.; Wells, B. O.; Joesten, R.; Aindow, M.; Suib, S. L. *Nat. Mater.* **2010**, *9*, 54-59.

(64) Liu, B.; Aydil, E. S. *J. Am. Chem. Soc.* **2009**, *131*, 3985-3990.

(65) Pan, Z. W.; Dai, Z. R.; Wang, Z. L. *Science* **2001**, *291*, 1947-1949.

(66) Qin, D.-D.; Tao, C.-L.; In, S.-i.; Yang, Z.-Y.; Mallouk, T. E.; Bao, N.; Grimes, C. A. *Energy Fuels* **2011**, *25*, 5257-5263.

(67) Im, B.; Jun, H.; Lee, K. H.; Lee, S.-H.; Yang, I. K.; Jeong, Y. H.; Lee, J. S. *Chem. Mater.* **2010**, *22*, 4806-4813.

(68) Long, H.; Shi, T.; Jiang, S.; Xi, S.; Chen, R.; Liu, S.; Liao, G.; Tang, Z. *J. Mater. Chem. A* **2014**, *2*, 3741-3748.

(69) Sun, X.; Li, Q.; Lu, Y.; Mao, Y. *Chem. Commun.* **2013**, *49*, 4456-4458.

(70) Yang, Y.; Kim, D.; Yang, M.; Schmuki, P. *Chem. Commun.* **2011**, *47*, 7746-7748.

(71) Kelzenberg, M. D.; Boettcher, S. W.; Petykiewicz, J. A.; Turner-Evans, D. B.; Putnam, M. C.; Warren, E. L.; Spurgeon, J. M.; Briggs, R. M.; Lewis, N. S.; Atwater, H. A. *Nat. Mater.* **2010**, *9*, 239-244.

(72) Law, M.; Greene, L. E.; Johnson, J. C.; Saykally, R.; Yang, P. *Nat. Mater.* **2005**, *4*, 455-459.

(73) Lin, H.-J.; Baltrus, J. P.; Gao, H.; Ding, Y.; Nam, C. Y.; Ohodnicki, P.; Gao, P.-X. *ACS Appl. Mater. Interfaces* **2016**, *8*, 8880-8887.

(74) Oh, I.; Kye, J.; Hwang, S. *Nano Lett.* **2012**, *12*, 298-302.

(75) Zhu, Y. W.; Zhang, H. Z.; Sun, X. C.; Feng, S. Q.; Xu, J.; Zhao, Q.; Xiang, B.; Wang, R. M.; Yu, D. P. *Appl. Phys. Lett.* **2003**, *83*, 144.

(76) Cui, X.; Hu, F.; Wei, W.; Chen, W. *Carbon* **2011**, *49*, 1225-1234.

(77) Liu, J.; Essner, J.; Li, J. *Chem. Mater.* **2010**, *22*, 5022-5030.

(78) Duay, J.; Sherrill, S. A.; Gui, Z.; Gillette, E.; Lee, S. B. *Acs Nano* **2013**, *7*, 1200-1214.

(79) Kim, J.-H.; Ayalasomayajula, T.; Gona, V.; Choi, D. *J. Power Sources* **2008**, *183*, 366-369.

(80) Xu, C.-L.; Bao, S.-J.; Kong, L.-B.; Li, H.; Li, H.-L. *J. Solid State Chem.* **2006**, *179*, 1351-1355.

(81) Liu, J.; Jiang, J.; Cheng, C.; Li, H.; Zhang, J.; Gong, H.; Fan, H. J. *Adv. Mater.* **2011**, *23*, 2076-2081.

(82) Sun, X.; Li, Q.; Lü, Y.; Mao, Y. *Chem. Commun.* **2013**, *49*, 4456-4458.

(83) Chen, S.; Zhai, T.; Lu, X.-H.; Zhang, M.-Z.; Li, Z.-Y.; Xu, C.-W.; Tong, Y. *Int. J. Hydrogen Energy* **2012**, *37*, 13350-13354.

(84) Lee, S. H.; Lee, H.; Cho, M. S.; Nam, J.-D.; Lee, Y. *J. Mater. Chem. A* **2013**, *1*, 14606-14611.

(85) Wu, M.-S.; Chiang, P.-C. J.; Lee, J.-T.; Lin, J.-C. *J. Phys. Chem. B* **2005**, *109*, 23279-23284.

(86) Xia, H.; Feng, J.; Wang, H.; Lai, M. O.; Lu, L. *J. Power Sources* **2010**, *195*, 4410-4413.

(87) Jonathon, D.; Stefanie, A. S.; Zhe, G.; Eleanor, G.; Sang Bok, L. *ACS nano* **2013**, *7*, 1200-1214.

(88) Williams, J. L. *Catal. Today* **2001**, *69*, 3-9.

(89) Armor, J. N. *Chem. Mater.* **1994**, *6*, 730-738.

(90) Hayes, R.; Kolaczkowskib, S.; Li, P.; Awdry, S. *Appl. Catal., B* **2000**, *25*, 93-104.

(91) Tomasic, V.; Gomzi, Z. *Chem. Biochem. Eng. Q.* **2001**, *15*, 109-115.

(92) Zhou, T.; Li, L.; Cheng, J.; Hao, Z. *Ceram. Int.* **2010**, *36*, 529-534.

(93) Bueno-López, A.; Lozano-Castelló, D.; Such-Basáñez, I.; García-Cortés, J. M.; Illán-Gómez, M. J.; Salinas-Martínez de Lecea, C. *Appl. Catal., B* **2005**, *58*, 1-7.

(94) Ribeiro, F.; Silva, J. M.; Silva, E.; Vaz, M. F.; Oliveira, F. A. C. *Catal. Today* **2011**, *176*, 93-96.

(95) Wang, T.; Yang, S.; Sun, K.; Fang, X. *Ceram. Int.* **2011**, *37*, 621-626.

(96) Agrafiotis, C.; Tsetsekou, A.; Ekonomakou, A. *J. Mater. Sci. Lett.* **1999**, *18*, 1421-1424.

(97) Chen, H.; Wang, J.; Li, H.; Wu, D.; Yao, M.; Li, Y. *Appl. Catal., A* **2012**, *427*, 73-78.

(98) Fujita, T.; Abe, H.; Tanabe, T.; Ito, Y.; Tokunaga, T.; Arai, S.; Yamamoto, Y.; Hirata, A.; Chen, M. *Adv. Funct. Mater.* **2016**, *26*, 1609-1616.

(99) Hutchings, G. J.; Mirzaei, A. A.; Joyner, R.; Siddiqui, M.; Taylor, S. H. *Appl. Catal., A* **1998**, *166*, 143-152.

(100) Mirzaei, A. A.; Shaterian, H. R.; Joyner, R. W.; Stockenhuber, M.; Taylor, S. H.; Hutchings, G. J. *Catal. Commun.* **2003**, *4*, 17-20.

(101) Tang, W.; Wu, X.; Li, S.; Shan, X.; Liu, G.; Chen, Y. *Appl. Catal., B* **2015**, *162*, 110-121.

(102) Vepřek, S.; Cocke, D.; Kehl, S.; Oswald, H. *J. Catal.* **1986**, *100*, 250-263.

(103) Hasegawa, Y.; Fukumoto, K.; Ishima, T.; Yamamoto, H.; Sano, M.; Miyake, T. *Appl. Catal., B* **2009**, *89*, 420-424.

(104) Hutchings, G. J.; Mirzaei, A. A.; Joyner, R. W.; Siddiqui, M. R. H.; Taylor, S. H. *Catal. Lett.* **1996**, *42*, 21-24.

(105) Kondrat, S. A.; Davies, T. E.; Zu, Z.; Boldrin, P.; Bartley, J. K.; Carley, A. F.; Taylor, S. H.; Rosseinsky, M. J.; Hutchings, G. J. *J. Catal.* **2011**, *281*, 279-289.

(106) Zhao, H.; Fang, K.; Zhou, J.; Lin, M.; Sun, Y. *Int. J. Hydrogen Energy* **2016**, *41*, 8819-8828.

(107) Guo, Y.; Zhang, Z.; Ren, Z.; Gao, H.; Gao, P.-X. *Catal. Today* **2012**, *184*, 178-183.

(108) Ren, Z.; Botu, V.; Wang, S.; Meng, Y.; Song, W.; Guo, Y.; Ramprasad, R.; Suib, S. L.; Gao, P. X. *Angew. Chem. Int. Ed.* **2014**, *53*, 7223-7227.

(109) Wang, S.; Ren, Z.; Guo, Y.; Gao, P.-X. *CrystEngComm* **2016**, *18*, 2980-2993.

(110) Ren, Z.; Guo, Y.; Zhang, Z.; Liu, C.; Gao, P.-X. *J. Mater. Chem. A* **2013**, *1*, 9897.

(111) Wang, S.; Ren, Z.; Song, W.; Guo, Y.; Zhang, M.; Suib, S. L.; Gao, P.-X. *Catal. Today* **2015**, *258*, 549-555.

Chapter 2. Experimental Techniques

2.1 Fabrication of Manganese Oxide Rod Arrays

By hydrothermal synthesis, manganese oxide rod arrays have been fabricated on diverse substrates, i.e. Si wafers, fluorine-doped tin oxide (FTO) conductive glass, quartz plates, and platinum (Pt) foils. For the Si wafers (University Wafer) with a 50 nm SnO_2 seed layer, the SnO_2 seed layer was deposited on the Si wafers by an RF magnetron sputtering system using a Sn target (99.999%, Stanford Materials). The deposition rate was controlled at 0.3 $Å.s^{-1}$ in 7.0×10^{-3} Torr of argon (Ar, Airgas) plasma and followed by post annealing at 900 °C for 2 h. The SnO_2/Si wafers were washed with distilled de-ionized (DDI) water, acetone (J.T. Baker) and isopropanol (J.T. Baker) in sonication and dried by nitrogen gas before the fabrication. In a typical synthesis, 4.39 g manganese sulfate monohydrate ($MnSO_4 \cdot H_2O$, 26 mmol, Sigma-Aldrich) and 2.56 g potassium dichromate ($K_2Cr_2O_7$, 8.7 mmol, J. T. Baker) were dissolved in 65 mL DDI water. Then, 3.4 mL sulfuric acid (H_2SO_4, 95.0 – 98.0 %, J.T. Baker) was added dropwise into the solution under magnetic stirring. The clear orange solution and Si wafer substrate were transferred into a Teflon-lined autoclave, sealed and heated at 120 °C for 14 h. After the reactor was cooled down to room temperature at ambient conditions, the MORA on Si wafer was rinsed with DDI water and dried in a vacuum oven at 60 °C overnight. The Si wafer can be substituted by other commercial substrates such as FTO glass (MTI corp.), quartz plates (Chemglass Life Sciences) and Pt foils (Alfa Aesar) to obtain similar MORA structures.

2.2 Catalyst Preparation of Manganese Oxide Nanoarray-Based Monolithic Catalysts

A series of manganese oxide nanorods were in-situ grown on the cordierite honeycomb monoliths with uniform array architectures as monolithic catalysts for exhaust after-treatment. Depending on the different oxidants in hydrothermal reactions, $K_2Cr_2O_7$, $KClO_3$, and $K_2S_2O_8$, the monolithic catalysts were denoted as HM-DCM, HM-PCR, and HM-PSF, respectively. All chemicals in this study were purchased from chemical vendors and used directly. The ceramic substrates, cordierite honeycomb monolith, were obtained from Corning Corp. The cordierite substrate was cleaned by sonication in ethanol, water, and acetone for 30 min before reaction.

2.2.1 Hydrothermal Synthesis of Nanoarray-Based Monolithic Catalyst, HM-DCM

22 g manganese sulfate monohydrate ($MnSO_4 \cdot H_2O$, 130 mmol) and 12.8 g potassium dichromate ($K_2Cr_2O_7$, 43.5 mmol) were dissolved in 325 mL Distilled De-ionized (DDI) water. Then, 17 mL sulfuric acid (H_2SO_4, 95.0 – 98.0 %) was added dropwise into the solution. After transferring the solution into a 400 mL capped glass bottle, the cordierite substrate was located on the bottom. The reaction was heated at 90°C in an oil bath for 12 h with a mechanical stirrer from the top. After the reaction, manganese oxide nanorod arrays coated on cordierite honeycomb monoliths were washed with DDI water and dried with nitrogen gas to remove water inside the monolith channels. A further 2 h sonication in water was applied to remove loose powder of manganese oxides on the array surface. Then the coated honeycomb monoliths were dried in a vacuum oven at 60°C for overnight.

2.2.2 Hydrothermal Synthesis of Nanoarray-Based Monolithic Catalyst, HM-PCR

Manganese sulfate monohydrate ($MnSO_4 \cdot H_2O$, 90 mmol, 15.2 g) and potassium chlorate ($KClO_3$, 158 mmol, 19.4 g) dissolved in 300 mL DDI water with 5 mL sulfuric acid and reacted

at 90°C for 12 h. After the reaction, manganese oxide nanorod arrays coated on cordierite honeycomb monoliths were washed with DDI water and dried with nitrogen gas to remove water inside the monolith channels. A further 2 h sonication in water was applied to remove loose powder of manganese oxides on the array surface. Then the coated honeycomb monoliths were dried in a vacuum oven at 60°C for overnight.

2.2.3 Hydrothermal Synthesis of Nanoarray-Based Monolithic Catalyst, HM-PSF

6.62 g manganese acetate tetrahydrate ($Mn(CH_3COO)_2 \cdot 4H_2O$, 27 mmol) and 11.37 g potassium persulfate ($K_2S_2O_8$, 42 mmol) were dissolved in 270 mL DDI water with 4.5 mL sulfuric acid and reacted at 60°C for 6 h. After the reaction, manganese oxide nanorod arrays coated on cordierite honeycomb monoliths were washed with DDI water and dried with nitrogen gas to remove water inside the monolith channels. A further 2 h sonication in water was applied to remove loose powder of manganese oxides on the array surface. Then the coated honeycomb monoliths were dried in a vacuum oven at 60°C for overnight.

2.3 Catalyst Preparation of transition metal oxides/Nanoarray-Based Monolithic Catalysts

Additional hydrothermal reactions were applied to the manganese oxide nanoarray-coated cordierite substrates to fabricate uniform coating layers of different transition metal oxides. Several transition metal oxides as known as highly active heterogeneous catalysts were selected, i.e. birnessite manganese oxide (MnO_2) and copper manganese oxide ($CuMn_2O_4$). The cryptomelane MnO_2 nanoarray HM-PCR, synthesized using manganese sulfate ($MnSO_4$) and potassium chlorate ($KClO_3$), was chosen as the core support due to the high length-to-diameter ratio (average length

of 5 μm and diameter of 50 nm) and good stability in hydrothermal reactions. Microwave reactions were also attempted to fabricate transition metal oxides with nanosheets architecture on the manganese oxide nanoarray-coated cordierite substrates (HM-PCR). Some transition metal oxides were chosen by their well-known nanosheets morphology, i.e. nickel (II) oxide (NiO), spinel cobalt oxide (Co_3O_4) and copper (II) oxide (CuO). The programmable Biotage Initiator microwave synthesizer was used in all microwave synthesis.

2.3.1 Hydrothermal Synthesis of Birnessite MnO_2/Nanoarray-Based Monolithic Catalysts, NA-Birnessite

For birnessite manganese oxide coating, 1.89 g potassium permanganate ($KMnO_4$, 12 mmol) and 0.21 g ammonium fluorite (NH_4F, 6 mmol) were dissolved in 60 mL DDI water. HM-PCR nanoarrays coated cordierite substrates were merged into the solution and heated at 90°C for 16 h. After the reaction, a further 2 h sonication in water was applied to remove loose powder of manganese oxides on the array surface. Then the coated honeycomb monoliths were dried in a vacuum oven at 60°C for overnight.

2.3.2 Hydrothermal Synthesis of Copper Manganese Oxide ($CuMn_2O_4$)/Nanoarray-Based Monolithic Catalysts, HM-$CuMn_2O_4$

For $CuMn_2O_4$ hydrothermal coating reaction, 3.79 g potassium permanganate ($KMnO_4$, 24 mmol) and 2.89 g copper nitrate trihydrate ($Cu(NO_3)_2 \cdot 3H_2O$, 12 mmol) were dissolved in 60 mL DI water. The mixed solution was transferred to a 150 mL glass bottle within a MnO_2 nanoarray-coated honeycomb monolithic substrates (HM-PCR) and heated at 90 °C in a water bath for 30 h. After the reaction, as synthesized monoliths were treated by DI water rinse, 2 h sonication in water,

air blow, and vacuum drying at 60 °C for overnight. Then the monolithic catalysts were calcined at 300 °C for 2 h under atmosphere.

2.3.3 Hydrothermal Synthesis of $Co_{0.36}Cu_{0.64}Mn_2O_4$/Nanoarray-Based Monolithic Catalyst, NA-$Co_{0.36}Cu_{0.64}Mn_2O_4$

3.79 g potassium permanganate ($KMnO_4$, 24 mmol), 2.89 g copper nitrate trihydrate ($Cu(NO_3)_2 \cdot 3H_2O$, 12 mmol), and 0.105 g Cobalt nitrate hexahydrate ($Co(NO_3)_2 \cdot 6H_2O$, 0.36 mmol) were dissolved in 60 mL DI water. The mixed solution was transferred to a 150 mL glass bottle within a nanoarray (HM-PCR) coated honeycomb monolithic substrates and heated at 90 °C in a water bath for 4 h. After the reaction cools down, similar workup as the synthesis of HM-$CuMn_2O_4$ was applied following the order, rinse, sonication, air blow, and vacuum drying. Then the monolithic catalysts were calcined at 300 °C for 2 h under an air atmosphere.

2.3.4 Hydrothermal Synthesis of $Co_{0.53}Cu_{0.47}Mn_2O_4$/Nanoarray-Based Monolithic Catalyst, NA-$Co_{0.53}Cu_{0.47}Mn_2O_4$

3.79 g potassium permanganate ($KMnO_4$, 24 mmol), 2.89 g copper nitrate trihydrate ($Cu(NO_3)_2 \cdot 3H_2O$, 12 mmol), and 0.21 g Cobalt nitrate hexahydrate ($Co(NO_3)_2 \cdot 6H_2O$, 0.72 mmol) were dissolved in 60 mL DI water. The mixed solution was transferred to a 150 mL glass bottle within a nanoarray (HM-PCR) coated honeycomb monolithic substrates and heated at 90 °C in a water bath for 1 h. After reaction cools down, similar workup as the synthesis of HM-$CuMn_2O_4$ was applied following the order, rinse, sonication, air blow, and vacuum drying. Then the monolithic catalysts were calcined at 300 °C for 2 h under an air atmosphere.

2.4 Catalyst Preparation of Manganese oxide (MnO_2) Wash-Coated Monolithic Catalysts

To understand the catalytic performance contributed from nanoarray architecture, monolithic catalysts loaded the same active materials with nanoarray-based catalysts were prepared by a wash-coating method using polymer binder or powder-form support, i.e. polyvinylpyrrolidone (PVP) or alumina powder (α-Al_2O_3). The polymer binder, PVP, was used to deposit manganese oxide powders on the cordierite substrate after a simple calcination for binder removal. The alumina powder was applied as a porous support without providing any reactivity. Commercial manganese oxide (MnO_2) and Palladium mixed alumina solution (Pd/Al_2O_3) were utilized as the state-of-art standard catalysts for comparison.

2.4.1 Wash-Coating of manganese oxide (MnO_2) Powder-Based Monolithic Catalysts, PVP-DCM, PVP-PCR, PVP-PSF, and PVP-C-MnO_2

To prepare the wash-coated monolithic catalysts, commercial MnO_2 powders from Sigma-Aldrich or as-synthesized manganese oxide powders from each hydrothermal reaction (HM-DCM, HM-PCR, and HM-PSF) were mixed with the same weight of polyvinylpyrrolidone (PVP, M.W. 10,000) in ethanol and stirred for 2 h to form a viscous slurry. For each cycle, the cordierite substrate was dipped into the slurry for 20 min and gently treated with nitrogen gas to remove the extra liquid. Then the wet honeycomb monoliths were dried at 120°C for 1 h. The same dipping cycle was repeated until reaching the desired weight loading of MnO_2/PVP. The whole substrate was calcined at 400°C under air for 1 h to burn out the PVP binder. The monolithic catalysts wash-coated corresponding MnO_2 active materials were denoted as PVP-DCM, PVP-PCR, and PVP-PSF, respectively. The commercial MnO_2 powders loaded monolithic catalyst using wash-coated method was denoted as PVP-C-MnO_2 as well.

2.4.2 Wash-Coating of Copper Manganese oxide ($CuMn_2O_4$)/alumina support (α-Al_2O_3) Nanoarray-Based Monolithic Catalyst, WC-$CuMn_2O_4$, WC-$Co_{0.36}Cu_{0.64}Mn_2O_4$, WC-$Co_{0.53}Cu_{0.47}Mn_2O_4$, and WC-Pd.

$CuMn_2O_4$, $Co_{0.36}Cu_{0.64}Mn_2O_4$, and $Co_{0.53}Cu_{0.47}Mn_2O_4$ powder collected from each hydrothermal reaction were loaded on cordierite substrates using wash-coating methods for comparison with nanoarray-based monolithic catalysts. For instance, 0.2 g $CuMn_2O_4$ active material, 0.8 g α-Al_2O_3, and 5 mL DI water were stirred for 2 h to form a slurry with 20% active materials. For each wash-coating cycle, the cordierite substrate was dipped into the slurry for 30 min and blown by nitrogen flow to remove extra slurry. The wet cordierite substrate was dried at 150 °C for 1 h in an oven. Repeated the same procedure for 4 to 5 times to reach the loading amount of $CuMn_2O_4$ materials similar to nanoarray-based catalysts. Each wash-coated substrate was also calcined at 300 °C for 2h before the catalytic test.

Following the same procedure above, a commercial solution of 1% Pd/Al_2O_3 was used to prepare Pd wash-coated monolithic catalysts. The calculated Pd loading amount on cordierite substrates was 1 g/L. The Pd loaded monolithic catalysts were calcined at 500 °C for 2 h before the catalytic test.

2.5 Catalytic Performance Testing

2.5.1 Electrochemical Capacitance

All electrochemical measurements were measured by a three-electrode configuration and conducted with a CHI660A Electrochemical Workstation. The manganese oxide rod arrays coated FTO glass (MORA/FTO, 1.5 x 1.5 cm^2) can be used directly as a working electrode. The counter

and reference electrodes were Pt foil (1.5 x 1.5 cm^2, Alfa Aesar) and saturated calomel electrode (SCE, CH Instruments, Inc.). The electrolyte solution was 1 M Na_2SO_4 solution purged by Argon (Airgas) for 30 min. All electrodes were immersed into the electrolyte solution.

The working electrode for OMS-2 powder sample was prepared by mixing 10 mg of OMS-2 powder, 10 mg of Vulcan carbon, 10 mL DDI water, and 5 drops of 60 % polytetrafluoroethylene (PTFE) solution with 10 min sonication. Then, 20 µL of the mixture was drop on a pyrolytic graphite electrode and dried slowly at atmosphere.

For CV experiments, the measurements were performed in a potential range from 0 to 800 mV (vs. SCE) at different scan rates from 2 to 100 mVs^{-1}.The specific capacitance C ($F.g^{-1}$) was calculated depending on **Equation 2.1**. Q (Coulomb) was the average electric charge calculated from the integrated area of CV curve, ΔV (volt) was the potential window during the CV measurement, and m (g) was the amount of active material (manganese oxide rod arrays) deposited on FTO glass.

$$C = \frac{Q}{\Delta V \times m}$$

(**Equation 2.1**)

The galvanostatic charge-discharge experiments were carried out at different current densities from 1.5 to $A.g^{-1}$ in a potential range from 0 to 800 mV (vs. SCE). The specific capacitance C ($F.g^{-1}$) was calculated by **Equation 2.2**. I (A) was the current density, t (second) was the scan time, ΔV (volt) was the potential window during charge-discharge measurement, and m (g) was the amount of active material (manganese oxide rod arrays) deposited on FTO glass.

$$C = \frac{I \times t}{\Delta V \times m}$$

(**Equation 2.2**)

2.5.1.1. Carbon Monoxide (CO) Oxidations

Carbon monoxide (CO) oxidation is a common reaction to evaluate catalytic performances of heterogeneous catalysts using a continuous flow fixed bed quartz tubular reactor. In the For each catalytic test, 4 pieces of catalysts coated honeycomb substrate with a specific volume (2 mm × 2 mm × 10 mm, W × H × L) were packed in a quartz tubing with 4 mm diameter and located in a tube furnace. The outlet of the quartz tubing was connected to a gas chromatograph with a 6-foot molecular sieve 13X packed column and a thermal conductivity detector (GC-TCD, SKI 8610C Multiple Gas Analyzer) for the quantitation of CO and CO_2. The feed gas was 1% CO, 10% O_2 and balanced by N_2 with a 20 SCCM flow rate and 7,500 h^{-1} space velocity. A pretreatment under nitrogen was applied at 100°C for 1 h before the catalytic tests to remove moisture and impurities adsorbed on the surface of the catalyst.

2.5.2 Propane (C_3H_8) Oxidations

The catalytic performances of all copper manganese oxide coated monolithic catalysts were evaluated by carbon monoxide (CO) and propane (C_3H_8) oxidations using a BenchCAT reactor (Altamira Instruments). A Dycor Dymaxion mass spectrometer and an Agilent MicroGC were used for the analysis and quantification of gas species. For each catalytic test, one piece of the monolithic catalyst with 5 × 5 channels in cross section (5 mm × 5 mm × 10 mm, W × H × L) was packed in quartz tubing. The feed gas was 0.3% C_3H_8, 10% O_2 and balanced by N_2 with a 100 SCCM flow rate and 24,000 h^{-1} space velocity. A pretreatment under nitrogen was applied at 200

°C for 1 h before the catalytic tests to remove surface adsorbed moisture and impurities on the active materials.

2.6 Material Characterization Techniques

2.6.1 X-Ray Diffraction (XRD)

X-ray powder diffraction (XRD) is a nondestructive technique for phase and purity identification of crystalline materials. In an X-ray diffractometer, the cathode ray tube provided a monochromic radiation toward the sample. The incident ray produces constructive interference by certain crystal phases, which is similar to light reflection by a mirror with the incident angle equals to the reflection angle. The constructive interference happens when conditions satisfy Bragg's Law.

$$n\lambda = 2d\sin\theta \qquad \textbf{(Equation 2.3)}$$

In the **Equation 2.3**, n is constant (usually equal to 1), λ is the X-ray wavelength, and θ is the diffraction angle. The lattice space d can be calculated by the wave path-difference ($2d\sin\theta$) in the constructive interference.[2] In this study, all powder X-ray diffraction analyses were conducted using a Rigaku X-ray diffractometer with Cu Kα radiation (λ= 1.5406 Å), operating beam voltage of 40.0 KV, and a beam current of 44 mA.

2.6.2 Scanning Electron Microscopy (SEM) and Energy Dispersive Spectroscopy (EDS)

The accelerated electrons generated by high-voltage electron gun induced varied signals from the surface of solid samples, including secondary electrons, backscattered electrons, diffracted backscattered electrons, photons (characteristic X-rays), Auger electrons, etc. The secondary electrons and backscattered electrons are usually used for morphology and topography

of samples. The diffracted backscattered electrons are applied to determine crystal structures and orientation of minerals by electron backscatter diffraction (EBSD). The characteristic X-rays produced by inelastic collisions can be used to identify elemental analysis. High resolution and large depth of focus are major advantages of SEM. The SEM analysis is also a non-destructive technique to analyze the same material with good conductivity repeatedly.[3] All samples were studied with field emission scanning electron microscopy (FE-SEM) FEI Nova NanoSEM 450 at an accelerating voltage of 2 kV.

2.6.3 Transmission Electron Microscopy (TEM)

The same principles as the light microscope, TEM uses high-voltage electrons with much smaller wavelength instead of light. Therefore, TEM can obtain images with much higher resolution and finest details of internal structure, even individual atoms in some cases. The resolution of TEM depends on acceleration voltage of electron beam and abbreviation. The higher acceleration voltage can shorten the wavelength to increase the resolution and penetrating ability for the thicker specimen.

The condenser lens and apertures are used to focus a beam of electrons from the electron gun and exclude high angle electrons. High-voltage electron beam strikes the specimen and penetrates it depending upon the thickness and electron transparency of the specimen. These transmitted electrons are focused by the objective lens to form an image on phosphorescent screen or charge coupled device (CCD) camera. When passing through the specimen, electrons are scattered by the constituent elements in the sample. The scattered electrons can be collected into individual dots by the electromagnetic objective lens depending on different directions to form the

diffraction pattern.[4] In this study, Transmission electron microscopy (TEM) images were performed using a FEI Talos F200X with an accelerating voltage of 200 kV.

2.6.4 Nitrogen Isothermal adsorption and surface area

Gas isothermal adsorption is a common method to provide consistent results of the specific surface area using nitrogen, which possesses stable and reversible adsorption-desorption properties. The principle of isothermal adsorption is an extension of the Langmuir theory, which is a theory for monolayer molecular adsorption. The Brunauer–Emmett–Teller (BET) theory was published by Stephen Brunauer, Paul Hugh Emmett, and Edward Teller in 1938 to apply the adsorption theory for multilayer molecular adsorption for mesoporous materials with satisfying the three following hypotheses:

(a) Gas molecules can be physically adsorbed on a solid in layers infinitely.

(b) No interaction between each adsorption layer.

(c) The Langmuir theory can be applied to each layer of molecules.

Therefore the BET equation is extended as,

$$\frac{1}{\upsilon[\left(\frac{p_o}{p}\right)-1]} = \frac{c-1}{\upsilon_m c}\left(\frac{p}{p_o}\right) + \frac{1}{\upsilon_m c}$$

(**Equation 2.4**)

Where p is the equilibrium pressure of N_2, p_o is the saturation pressure of N_2 at experimental temperature, υ is the adsorbed volume at p, υ_m is the monolayer adsorbed quantity, and the c is the BET constant.

When the **Equation 2.4** be plotted as a straight line form, y = *a*x + b, the x is (p/p_o), the slope *a* is (c-1)/($\upsilon_m c$), and the intercept *b* is equal to 1/($\upsilon_m c$). The relative (p/p_o) between 0.05 and 0.3 are reliable for the linear equation. Then, the adsorbed monolayer gas quantity υ_m and the BET constant *c* can be the form of *a* and *b* as,

$$\upsilon_m = \frac{1}{a+b} \qquad c = 1 + \frac{1}{b}$$

The BET equation can be further applied to calculate the total surface area S_{Total} and specific surface area S_{BET}.

$$S_{Total} = \frac{\upsilon_m N s}{V}$$

(**Equation 2.5**)

$$S_{BET} = \frac{S_{Total}}{m}$$

(**Equation 2.6**)

In **Equation 2.5**, the υ_m is still the adsorbed monolayer gas quantity, *N* is the Avogadro's number, *V* is the molar volume of the adsorbed gas, and the *m* in **Equation 2.6** is the mass of the sample.

In this study, the surface areas of monolithic and powder-form samples were measured with N_2 isothermal adsorption experiments and Brunauer–Emmett–Teller (BET) method using a Quantachrome Autosorb-1-1C automated adsorption system. Both nanoarray-based and wash-coated monolithic catalysts were degassed at 150 °C for 6 h to remove moisture and other physically adsorbed species. The experiments of N_2 isothermal adsorption were measured at relative pressures (p/p_0) from 0.005 to 0.995 then followed by desorption from 0.995 to 0.12.

2.6.5 Temperature Programmed Reduction (TPR) and Desorption (TPD)

Temperature-programmed reduction (TPR), desorption (TPD) and mass spectrometry analyses were studied using a MKS gas analyzer coupled with a quadrupole mass selective detector. In general, 100 mg sample was loaded in a quartz tubing and located in a tube furnace as illustrated in **Figure 2.1**. A heat pretreatment for samples was applied using an inert gas flow (Ar, 50 SCCM) at 200 °C for 1 h to remove surface adsorbed water molecules and other impurities in the beginning. For hydrogen temperature-programmed reduction (H_2-TPR), a mixed gas of 10% hydrogen (H_2) balanced by nitrogen (N_2) with 200 SCCM flow rate was used in the experiments to reduce samples at the programmed heating process. The mass spectrometry analyzer monitors the varied signal of H_2 to obtain the consumption amount of H_2.

For oxygen temperature-programmed desorption (O_2-TPD), pure oxygen with a 25 SCCM flow rate was purged at room temperature for 1 h before desorption for oxygen molecules adsorbed on the surface defects of catalysts. After O_2 adsorption, the purging O_2 was replaced by pure Ar with a 25 SCCM flow rate accompany the programmed heating process. All evolution of oxygen species including surface adsorbed oxygen and material lattice oxygen is recorded by the mass spectrometry analyzer. All temperature-programmed measurements were performed from room temperature to 800°C with a ramping rate of 10°C/min.

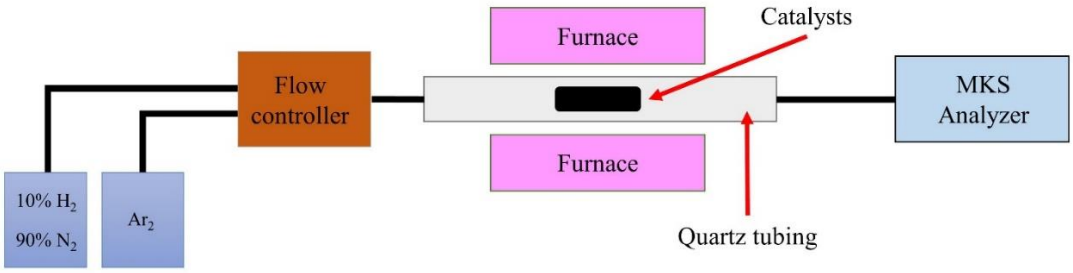

Figure 2.1 Diagram of hydrogen temperature programmed reduction setup.

2.6.6 Inductively Coupled Plasma Mass Spectrometry (ICP-MS)

Inductively coupled plasma mass spectrometry (ICP-MS) is a widely used technique for elemental analysis and determination with superior detection capabilities. ICP-MS has many well-known advantages like high sensitivity (detection limit up to ppt, 10^{-12}), ability to detect most element (except H, C, N, O, and halogens), short detection time, simultaneous analysis of multiple elements, wide range, and low mass overlapping effect. In general, an ICP-MS is composed of three major parts, (i) sample injection system, (ii) inductive coupled plasma source, and (iii) mass spectrometers. The sample injection system sprays aqueous sample solution into the plasma chamber and induction coil. The inductively coupled plasma is used to vaporize, decompose, atomize, and ionize sample at super high-temperature (8000°C). The different ions can be determined by mass spectrometers, which are categorized to three major species, i.e. quadrupole, magnetic sector field, and time-of-flight mass spectrometers. Before injection, solid state samples need to be acid-digested to an aqueous solution using a strong acid like Aqua Regia or hydrofluoric acid. Due to precise quantitative analysis, especially isotope and trace elemental analysis, ICP-MS is extensively applied in many areas, e.g. material science, geology, nuclear engineering, environmental detection, pharmaceutics, and semiconductor manufacturing.

2.6.7 X-Ray Photoelectron Spectroscopy (XPS)

X-ray photoelectron spectroscopy (XPS) is a general technique for analysis of elemental composition, oxidation state, and electronic state near surface of materials (1 – 10 nm). The photo-emitted electrons are collected to measure their kinetic energies by irradiating a focused beam of X-ray (i.e. Al-K_{α}, 1486.7 eV) to the surface of materials. The electron binding energies of each emitted electrons can be obtained using **Equation 2.7** and the known energy of the X-rays.

$$E_b = hv - E_k - \phi$$

(**Equation 2.7**)

In **Equation 2.7**, the E_b is the binding energy of the electron, hv is the energy of the X-rays, E_k is the kinetic energy of the emitted electron, and the ϕ is the work function of spectrometer and materials. In this study, the surface elemental analysis of catalysts was conducted with X-ray photoelectron spectroscopy (XPS) using a PHI Model 590 spectrometer with multiprobes. XPS The binding energies in XPS spectra were calibrated using the signal from adventitious carbon (284.6 eV).

2.6.8 References

(1) Biswas, S.; Poyraz, A. S.; Meng, Y.; Kuo, C.-H.; Guild, C.; Tripp, H.; Suib, S. L. *Appl. Catal., B* **2015**, *165*, 731-741.

(2) Nave, C. R., *Hyperphysics, Bragg's Law*, 2016, http://hyperphysics.phy-astr.gsu.edu/hbase/quantum/bragg.html,

(3) Kaech, A., *An Introduction to Electron Microscopy*, 2013.

(4) Wikipedia, *Transmission Electron Microscopy*, 2016.

Chapter 3. Scalable and Template-Free Synthesis of Highly Ordered Manganese Oxide Rod Arrays

3.1 Introduction

A facile and scalable synthetic strategy was developed to fabricate highly ordered cryptomelane type manganese oxide nanorods with three-dimensional (3D) array architectures. By hydrothermal reactions, manganese oxide (MnO_2) nanoarrays were deposited on Si wafers for investigating growth mechanism and applied on fluorine-doped tin oxide (FTO) glass as supercapacitors. As a generic growth process on this diverse array of solid substrates, a 50 nm thick layer of SnO_2 has been deposited on the substrates using magnetron sputtering or dip-coating before the hydrothermal reaction. The tetragonal rutile SnO_2 seed layer has assisted the preferred orientation growth of OMS-2 rods with good adhesion of rods on the substrates and controlled growth region on the substrate. Seed layers have generally been utilized for the growth of various non-MnO_2 rod arrays.[1,2] In this study, tetragonal SnO_2 (cassiterite, $a = b = 4.737$ Å and $c = 3.185$ Å) was successfully applied as the seed layer due to its similarity to the crystal structure of OMS-2 (cryptomelane, $a = b = 9.82$ Å and $c = 2.85$ Å), which may be advantageous to the epitaxial growth of OMS-2 on the substrate.[3,4] This easy-control and template-free generic procedure could enable a potentially broad use of these manganese oxide arrays in catalysis, sensor, and electrochemical energy storage.[2,5] In the synthesis, manganese sulfate was chosen as a manganese source and potassium dichromate as an oxidant. Sulfuric acid was used to create an acidic environment required for the formation of the OMS-2 structure.[6] The redox potential of $Cr_2O_7^{2-}/Cr^{3+}$ (1.33 V) is slightly higher than Mn^{4+}/Mn^{2+} (1.23 V) which resulted in a controlled reaction

rate. Moreover, the hydrothermal method also provides mild and stable reaction environment for the growth of highly crystalline prism rods. The **Equation 3.1** below shows the balanced chemical reaction of Mn^{4+}/Mn^{2+} and $Cr_2O_7^{2-}/Cr^{3+}$ to form manganese oxide.

$$16\ MnSO_4(aq) + 5\ K_2Cr_2O_7(aq) + 3\ H_2SO_4(l) \rightarrow$$

$$2\ KMn_8O_{16}(s) + 5\ Cr_2(SO_4)_3(aq) + 4\ K_2SO_4(aq) + 3\ H_2O(l) \quad \textbf{(Equation 3.1)}$$

3.2 Characterization Studies of Manganese Oxide Rod Arrays

3.2.1 Morphology Study of Nanorod Arrays

The morphologies of the as-synthesized manganese oxide nanoarrays were investigated by SEM as shown in **Figure 3.1**. The typical top view SEM images of as-prepared manganese oxide rod arrays coated film are shown in **Figure 3.1(a)** and **3.1(b)**. The images show square ended rods formed with merged tiny fibers on top. The cross-sectional SEM image [**Figure 3.1(c)**] showed that this 100 nm wide rods stand vertically on the tin oxide (SnO_2) seeded Si wafer forming large scale and uniform arrays with a typical height of about 1 μm. **Figure 3.1(d)** shows SEM images from the top and side views of rod arrays on the substrate as a function of reaction time. At the beginning (40 min), inclined tiny manganese oxide rods were formed without distinct edges and uniform shape. Then, in 2 h, longer manganese oxide fibers started appearing with sharp tails (40 min – 2 h). At 4 h, all manganese oxide rods have a rectangular structure with an average height of 700 nm and are aligned vertically. The length of rods reaches 1 μm at around 10 h. Longer reaction times (14 h) didn't change the length, but the rods got thicker in diameter with clearer edges. **Figure 3.1(d)** (uncoated) also shows a homogeneous SnO_2 layer covered on the Si-substrate.

The image shows well-deposited and fully covered SnO_2 film on Si wafer. The uniform rod arrays have also been successfully synthesized on different types of large and solid substrates such as honeycomb monolith, fluorine-doped tin oxide (FTO) glass, quartz plate, platinum foil, and cordierite honeycomb monoliths as shown in **Figure 3.2**.

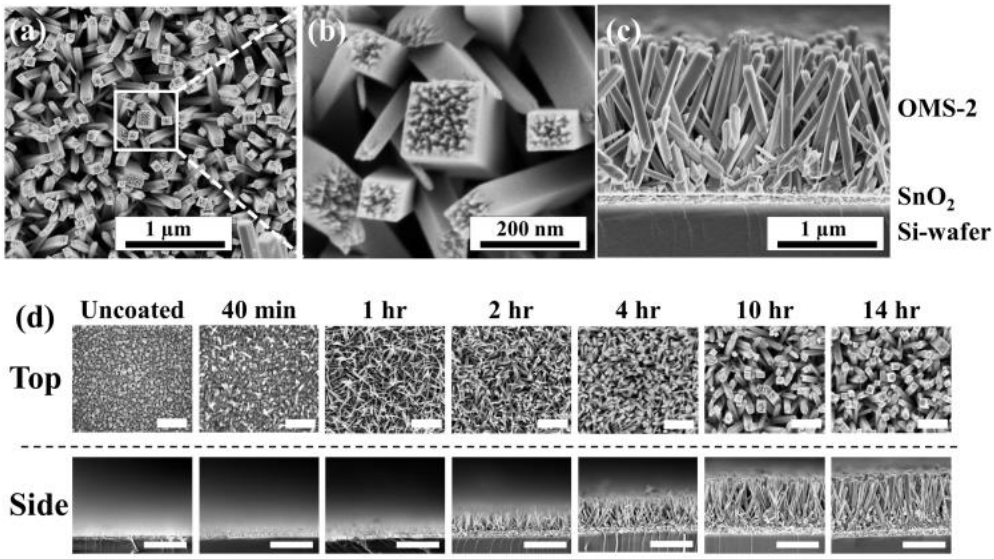

Figure 3.1 SEM images of as-synthesized manganese oxide rod arrays at 120 °C for 14 h: (a), (b) top, and (c) cross-sectional views; (d) SEM images of rod arrays grown on SnO_2/Si wafer with various reaction times (40 min – 14 h), top and side views. Scale bars are unified as 500 nm (top row) and 1 μm (bottom row).

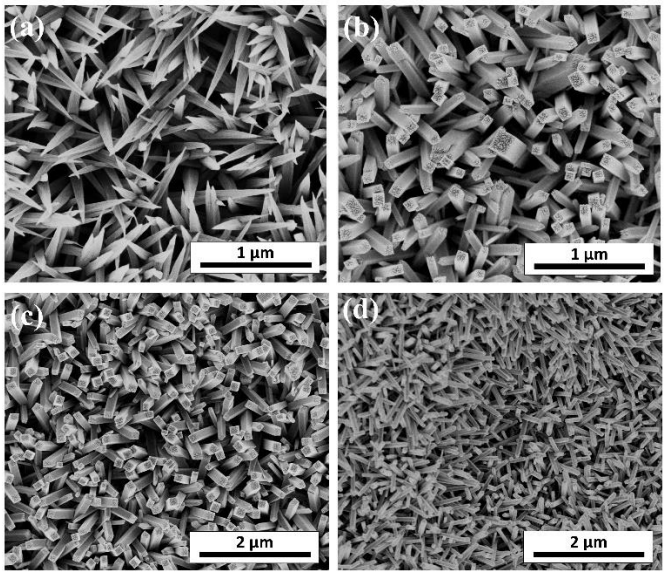

Figure 3.2 SEM images of manganese oxide rod arrays composites fabricated on different substrates: (a) FTO glass, (b) quartz plate at 120 °C, (c) Pt foil at 120 °C, and (d) HM at 120 °C.

3.2.2 Crystal Structure Study of Nanorod Arrays

The powder X-ray diffraction (PXRD) results [**Figure 3.3(a)**] indicate that the powder collected from the hydrothermal reaction solution can be indexed as being a pure tetragonal cryptomelane manganese oxide (OMS-2) (JCPDS No. 29-1020). The lack of (110), (200), and (310) planes of OMS-2 was observed in the XRD pattern of rod arrays, suggesting a preferential orientation in the direction of (hkl) planes. A plausible explanation for the lack of certain planes is that all (hk0) planes aligned vertically on the substrate. A comparable study done by Espinal et al. presented only (hk0) diffraction lines observed in XRD analyses when OMS-2 crystal rods were parallel to the surface of single crystal strontium titanium oxide (STO) substrate.[7] This is also consistent with the SEM observation [**Figure 3.1(c)**] of the rod-like OMS-2 structures along their *c*-axis. In **Figure 3.3(b)**, OMS-2 related diffraction patterns can be seen clearly for manganese

oxide rod arrays grown for 2 h or more time. At longer reaction times, the intensities of (211), (301), and (411) planes increased and became clearer.

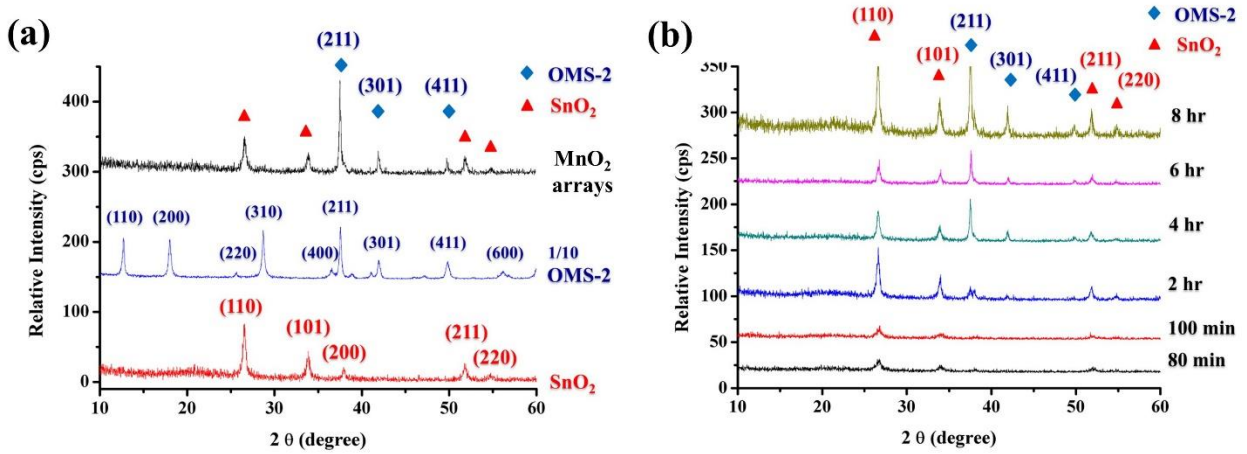

Figure 3.3 (a) X-ray diffraction (XRD) patterns of as-synthesized manganese oxide rod arrays on SnO_2/Si wafer (top), OMS-2 powder collected from the MORA growth solution (middle), and uncoated SnO_2/Si wafer (bottom); (b) XRD diffraction patterns of rod arrays on SnO_2/Si wafer as-synthesized from 80 min to 8 h at 120 °C.

The nature of the rod arrays was further investigated by high-resolution transmission electron microscopy (HR-TEM). **Figure 3.4(a)** shows a tip of an individual OMS-2 rod scratched off from the manganese oxide rod arrays on SnO_2/Si wafer. The image shows that the rectangular rod was composed of many nanocolumns. In **Figure 3.4(b)**, the lattice fringes were indexed as the (200) plane of OMS-2 (cryptomelane) with a consistent interplanar *d*-spacing of 4.87 Å. The HR-TEM image and selected area electron diffraction (SAED) pattern of an individual OMS-2 rod further revealed that the (200) planes are parallel to the long side (*c*-axis) of the rod [**Figure 3.4(c)** and **3.4(d)**]. The results are consistent with the findings by Yuan et al. and Feng et al..[8,9]

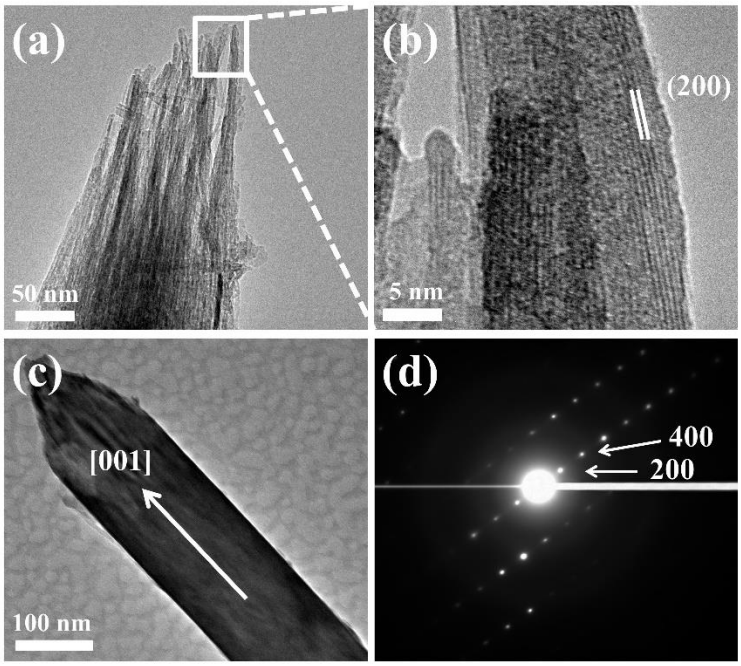

Figure 3.4 TEM images of individual OMS-2 rods scratched off from rod arrays on SnO_2/Si wafer: (a) tip of a rod tail (4 h reaction time), (b) part of a rod tip featuring the fringe of cryptomelane OMS-2 (200) plane; (c) an individual OMS-2 rod and the corresponding selected area electron diffraction (SAED) pattern (d).

3.3 Electrochemical Performance

The manganese oxide rod arrays (MORA) are believed to be a potential energy storage material due to possessing several advantages such as being a scalable coating, the binder-free nature, and the absence of support. Therefore, cyclic voltammetry (CV) was used to measure the specific capacitance of manganese oxide rad arrays coated fluorine-doped tin oxide glass (MORA/FTO) as an electrochemical capacitor. **Figure 3.5(a)** shows the CV characteristics of the MORA/FTO with a potential window of 0.8 Volt at different scan rates (2 - 100 mVs^{-1}). The symmetric and rectangular shapes of resulting CV curves indicate that MORA/FTO possesses

good oxidation-reduction behavior, reversibility, and electrochemical performance, thus a promising capacitor electrode.

Table 3.1 summaries the calculated specific capacitance of both MORA/FRO and OMS-2 powder using different scan rate in CV experiments. The specific capacitance reaches 108 $F.g^{-1}$ at 2 mVs^{-1} scan rate. The maximum specific capacitance drops 40% at high scan rates (100 mVs^{-1}) (capacitance from 108 $F.g^{-1}$ to 65 $F.g^{-1}$). To compare the performance of capacitors between MORA and OMS-2, the powder of OMS-2 (collected from the same hydrothermal reaction) was also tested for its specific capacitance under the same experimental conditions [**Figure 3.5(a)**]. The contribution of capacitance from the FTO substrate was negligible, while the capacitance of the MORA/FTO (108 $F.g^{-1}$) was almost twice that of the OMS-2 powder (60 $F.g^{-1}$). This result suggests that the array architecture of manganese oxide may provide a shorter path for electron transportation and a larger surface area for intercalation of Na^+ ions during the CV scans.[10,5]

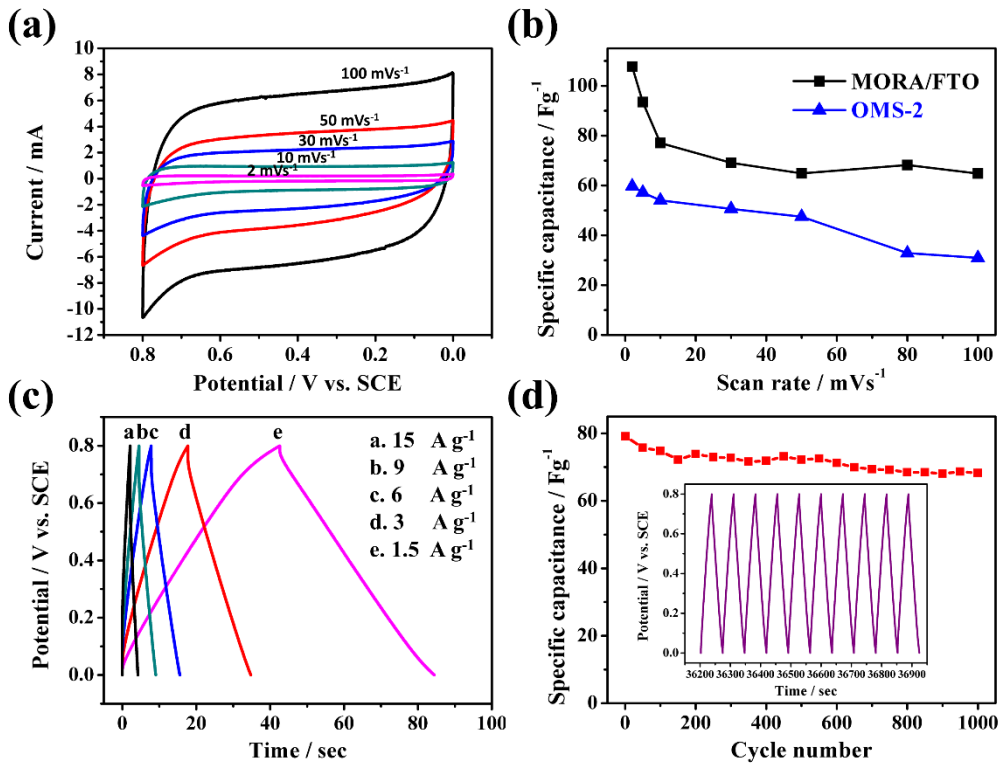

Figure 3.5 The electrochemical performances of manganese oxide rod arrays-based supercapacitors: (a) The cyclic voltammetry (CV) curves at different scan rates; (b) the specific capacitance as a function of the scan rate: MORA/FTO vs. OMS-2; (c) the galvanostatic charge-discharge curves scanned in the potential range from 0 to 0.8 V at different current densities; (d) the test of stability measured for 1000 cyclic charge-discharge scans at 1.5 $A.g^{-1}$ current density, the specific capacitance as a function of the cycle number. The inset shows the last 10 cycles of charge-discharge tests.

Table 3.1 The specific capacitance of MORA/FTO and OMS-2 powder at different scan rates.

Scan rate (mVs^{-1})	2	5	10	30	50	80	100
MORA/FTO	107.68	93.50	77.01	69.11	64.86	68.23	64.74
OMS-2 powder	59.69	57.19	54.06	50.63	47.50	32.84	30.95

The galvanostatic measurements were also performed to evaluate the charge-discharge performances and stabilities of the MORA/FTO composite as an electrode material. The galvanostatic curves were scanned under different current densities as shown in **Figure 3.5(c)**. The symmetric curves revealed a highly linear and consistent charge-discharge property at different current intensities ranging from 1.5 $A.g^{-1}$ to 15 $A.g^{-1}$. **Table 3.2** lists the calculated specific capacitance of both MORA/FRO at different current densities in galvanostatic experiments. The highest obtained specific capacitance is 79 $F.g^{-1}$ at 1.5 $A.g^{-1}$ current density which is still 73% of the capacitance obtained from CV. The lower capacitance is due to the relative higher scan rate in galvanostatic charge-discharge at 1.5 $A.g^{-1}$ than CV at 2 mVs^{-1}. The long-term cyclic stability was also tested and more than 1000 scans were collected at a constant current density of 1.5 $A.g^{-1}$ [**Figure 3.5(d)**]. Although a small decrease at discharge time was observed during charge-discharge tests, even after 1000 cycles, the MORA/FTO electrode still maintained 86% of its specific capacitance (79 $F.g^{-1}$ to 68 $F.g^{-1}$) as shown in **Table 3.3**. The results support the stable structure of OMS-2 and excellent binding of rod arrays on the surface of FTO glass.

Table 3.2 The specific capacitance of as-synthesized MORA/FTO electrode.

Current density ($A.g^{-1}$)	1.5	3	6	9	15
Specific capacitance ($F.g^{-1}$)	78.75	63.75	57.75	50.63	39.38

Table 3.3 The specific capacitance of MORA/FTO electrode for the long-term stability test (1000 cycles).

Cycle number	1st	50th	100th	150th	200th	250th	300th
Specific Capacitance ($F.g^{-1}$)	79.13	75.75	74.81	72.19	73.87	72.94	72.75
	350th	400th	450th	500th	550th	600th	650th
	71.63	71.81	73.13	72.19	72.56	71.25	69.94
	700th	750th	800th	850th	900th	950th	1000th
	69.38	69.19	68.44	68.44	68.06	68.63	68.25

3.4 Conclusion

In summary, octahedral molecular sieve (OMS-2, cryptomelane) nanorods were successfully fabricated as uniform 100 nm wide manganese oxide rod arrays (MORA) with ~1 μm height by a facile, scalable and template-free procedure. The rectangular OMS-2 rods grew with a preferred orientation along the [001] direction (*c*-axis). The manganese oxide rod arrays coated FTO composite (MORA/FTO) exhibited specific capacitance reaching as high as 108 $F.g^{-1}$ at a 1.5 mVs^{-1} scan rate with good reversibility and long-term stability. These results suggest the manganese oxide material with array architectures as a promising material for electrochemical energy storage. Using a similar wet chemical process, these MORAs can be grown on a diverse array of substrates including Si wafers, FTO glass, quartz plates, Pt foils, and honeycomb monoliths, featuring its potential to be utilized in a broad spectrum of areas such as sensors, catalysis, and electrochemical energy storage.

3.5 References

(1) Costa, S. V.; Gonçalves, A. S.; Zaguete, M. A.; Mazon, T.; Nogueira, A. F. *Chem. Commun.* **2013**, *49*, 8096-8098.

(2) Gao, P.-X.; Shimpi, P.; Gao, H.; Liu, C.; Guo, Y.; Cai, W.; Liao, K.-T.; Wrobel, G.; Zhang, Z.; Ren, Z. *Int. J. Mol. Sci.* **2012**, *13*, 7393-7423.

(3) Gao, H.; Cai, W.; Shimpi, P.; Lin, H.-J.; Gao, P.-X. *J. Phys. D: Appl. Phys.* **2010**, *43*, 272002.

(4) Jian, D.; Gao, P.-X.; Cai, W.; Allimi, B. S.; Alpay, S. P.; Ding, Y.; Wang, Z. L.; Brooks, C. *J. Mater. Chem.* **2009**, *19*, 970-975.

(5) Lu, X.; Zheng, D.; Zhai, T.; Liu, Z.; Huang, Y.; Xie, S.; Tong, Y. *Energy. Environ. Sci.* **2011**, *4*, 2915-2921.

(6) Li, W. N.; Yuan, J.; Shen, X. F.; Gomez- Mower, S.; Xu, L. P.; Sithambaram, S.; Aindow, M.; Suib, S. L. *Adv. Funct. Mater.* **2006**, *16*, 1247-1253.

(7) Espinal, A. E.; Yan, Y.; Zhang, L.; Espinal, L.; Morey, A.; Wells, B. O.; Aindow, M.; Suib, S. L. *Small* **2014**, *10*, 66-72.

(8) Yuan, J.; Li, W.-N.; Gomez, S.; Suib, S. L. *J. Am. Chem. Soc.* **2005**, *127*, 14184-14185.

(9) Zhao, X. D.; Fan, H. M.; Luo, J.; Ding, J.; Liu, X. Y.; Zou, B. S.; Feng, Y. P. *Adv. Funct. Mater.* **2011**, *21*, 184-190.

(10) Hochbaum, A. I.; Yang, P. *Chem. Rev.* **2009**, *110*, 527-546.

Chapter 4. Manganese Oxide Nanorod Arrays Based Monolithic Catalysts for CO Oxidations

4.1 Introduction

Herein, a synthetic strategy was applied to *in-situ* grow manganese oxide nanorod arrays on the cordierite honeycomb substrates. This strategy provided a facile method to deposit a robust layer of urchin-like nano-arrays onto the honeycomb monoliths without using any binders. In general, urchin-like manganese oxide can be achieved by slowly oxidizing Mn^{2+} to Mn^{4+} in acidic environment using hydrothermal syntheses.[1-5] Nanowires or nanorods were crystalized radially along the preferred plane of the nuclei aggregated by small nanoparticles to form urchin-like structures. Similarly, with cordierite substrates in solution, heterogeneous nucleation occurred on the surface of substrates to precipitate a seed layer of manganese oxide nanoparticles as nuclei.[6,7] Then, dense manganese oxide nanorods grew perpendicularly on the seed layers to form nano-array architectures. Therefore, three hydrothermal synthetic processes of manganese oxides using different oxidants such as potassium dichromate ($K_2Cr_2O_7$), potassium chlorate ($KClO_3$), and potassium persulfate ($K_2S_2O_8$), were synthesized and denoted to HM-DCM, HM-PCR, and HM-PSF, respectively.[1,2,5] All three manganese oxide catalysts presented cryptomelane as their major crystal structure but had different morphologies of nano-array and catalytic performances due to diverse reduction potentials of oxidants applied in the hydrothermal syntheses. The open surface feature of nanorod arrays also enhanced conversion of CO oxidation compared to dip-coated manganese oxide monolithic catalysts. Studies of O_2-TPD and XPS displayed abundant surface adsorbed oxygen and lattice oxygen contributing to the highest reactivity of HM-PSF. Multiple

correlations among surface area, reducibility, oxidation states and chemical reactivity were discussed in this study as well.

4.2 Characterization Studies of Nano-Arrays Based Monolithic Catalysts

4.2.1 Morphology of Nano-Arrays (SEM)

The SEM images showed manganese oxide aligned vertically on the cordierite substrate (**Figure 4.1(a)-(f)**), and varied morphologies of manganese oxide rods were formed when using different oxidants. All of the three cryptomelane nano-arrays were distributed uniformly in the channels of the monolith substrate. The HM-DCM had sharp pyramidal shapes with average lengths of ~ 2.5 μm and diameters of 50-100 nm as shown in **Figures 4.1(a)** and **4.1(d)**. The nanowire arrays, HM-PCR, presented in **Figures 4.1(b)** and **4.1(e)** had longer lengths ~ 5 μm and smaller diameters ~ 20-50 nm. The HM-PSF nanorods displayed cylindrical shaped shorter lengths ~ 1 μm and a bigger diameter ~ 100 nm, as shown in **Figures 4.1(c)** and **4.1(f)**. Furthermore, a layer with a thickness about 0.5 ~ 1 μm of manganese oxide was deposited above the cordierite substrate during the hydrothermal synthesis for each monolithic catalyst. This deposited layer of manganese oxide played a critical role as the seeds for nanorod growth as a binder between the nano-arrays and the substrate. Each nano-array based monolithic catalyst exhibited good binding on the cordierite substrate and excellent robustness after a 2 h sonication in water to remove detrital nanorods and powder. In **Figures 4.1(g)-(i)**, all manganese oxide powders collected from each reaction exhibited urchin-like structures. The nanoparticles with bigger diameters in the powders can form longer nano-arrays when depositing on cordierite substrates. Therefore, the order of

nano-array lengths was the same as the diameters of urchin-like powders, HM-PCR > HM-DCM > HM-PSF.

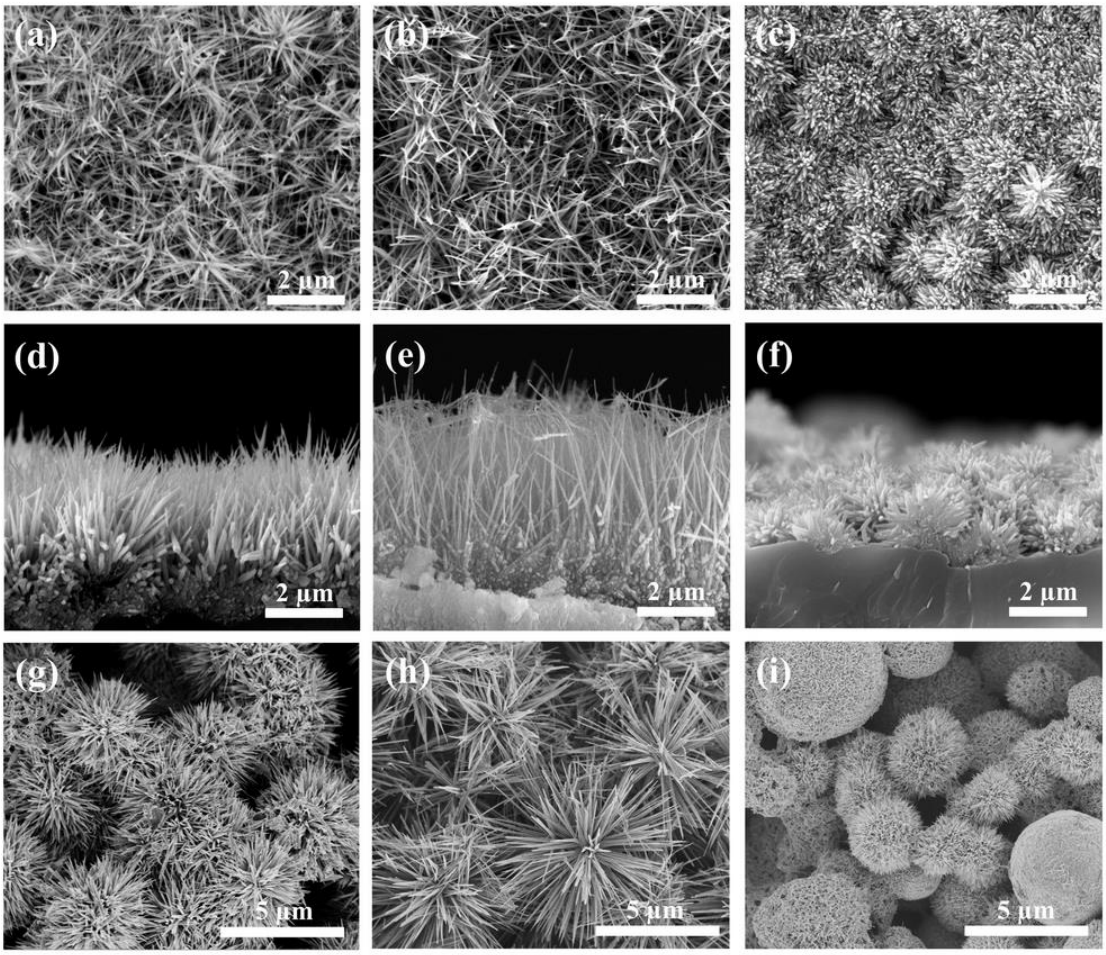

Figure 4.1 SEM images of manganese oxide nanorod arrays on the cordierite substrate: (a) top view and (d) cross-sectional view of HM-DCM; (b) top view and (e) cross-sectional view of HM-PCR; (c) top view and (f) cross-sectional view of HM-PSF. SEM images of as-synthesized manganese oxide powders collected from each reaction: (g) HM-DCM; (h) HM-PCR; (i) HM-PSF.

4.2.2 Crystal Structure (XRD and TEM) & Surface Area (BET)

The crystal structures of all catalysts were identified by powder X-ray diffraction (XRD). The XRD patterns were conducted on both the honeycomb monoliths coated with manganese oxide nanoarrays and the precipitates collected from each hydrothermal reaction [**Figure 4.2(a**)] because the intensities of manganese oxide collected from monolithic catalysts were much lower as compared to the diffraction patterns of cordierite substrates.

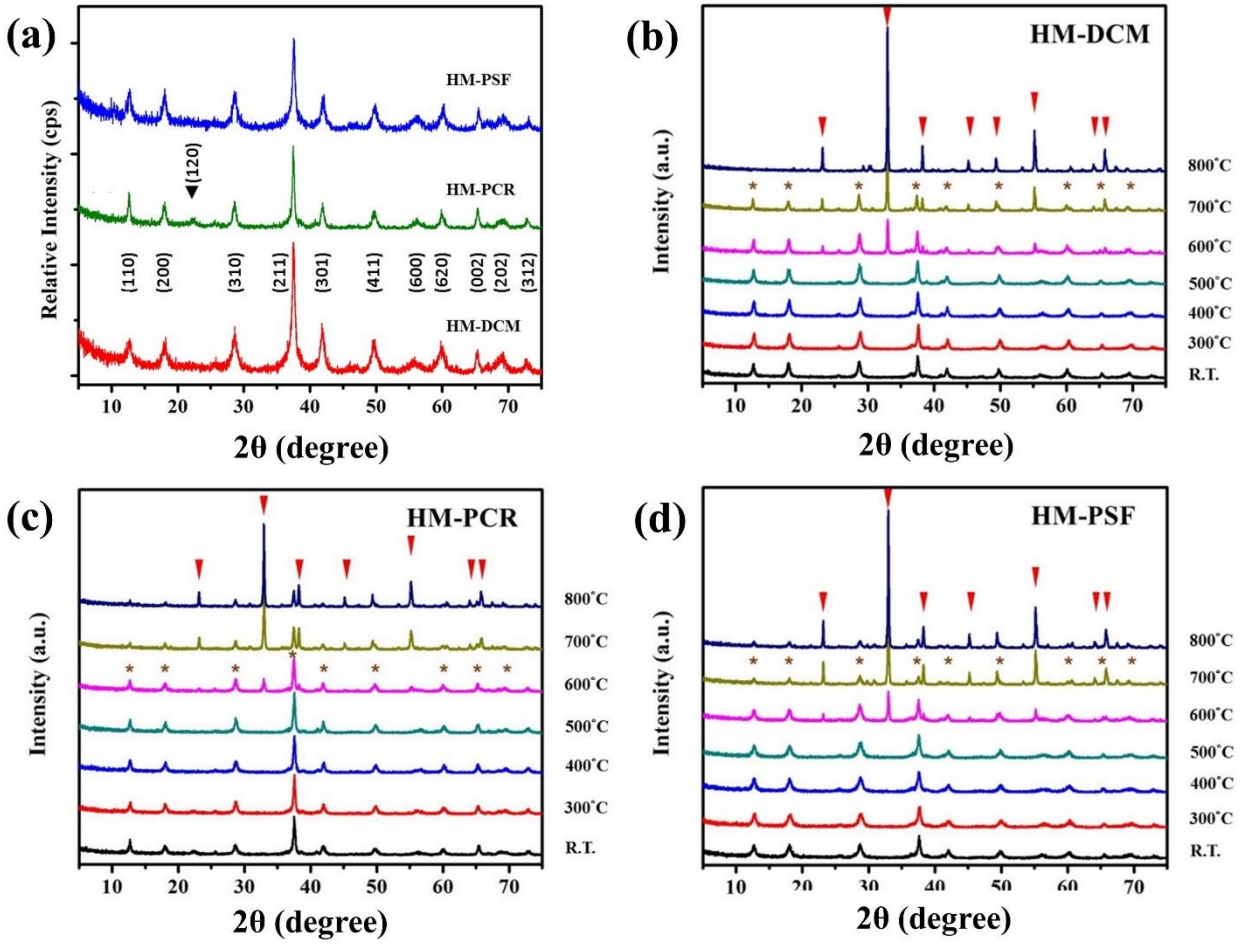

Figure 4.2 The XRD patterns of (a) HM-DCM (cryptomelane), HM-PCR (cryptomelane/nsutite ▼), and HM-PSF (cryptomelane). For (b)-(d), (b) HM-DCM, (c) HM-PCR, and (d) HM-PSF calcined at various temperatures from room temperature (R.T.) to 800°C.

The nano-arrays of HM-DCM and HM-PSF can be indexed to manganese oxide with the cryptomelane structure ($K_{2-x}Mn_8O_{16}$, tetragonal, $a = b = 9.82$ Å and $c = 2.85$ Å, JCPDS: 29-1020). The diffraction patterns of as-synthesized HM-PCR displayed mixed phases of cryptomelane as majority and nsutite (γ-MnO_2, JCPDS: 14-0644) as a minority. XRD patterns of the three catalysts were collected under air at various temperatures from room temperature to 800°C to study the thermal stability of manganese oxide materials. **Figure 4.2(b)-(d)** showed that all three materials maintained the major cryptomelane structure at 500°C and started to have some diffraction patterns of the bixbyite phase at 600°C. At 800°C, each cryptomelane was converted to bixbyite completely. The (120) plane of nsutite in the HM-PCR [**Figure 4.2(c)**] disappeared at 400°C, with the only cryptomelane remaining. The HM-PSF transformed to bixbyite above 600°C, but partial diffraction patterns of cryptomelane still existed at 800°C. The calcination tests indicated that cryptomelane manganese oxide nano-arrays were stable below 500°C.

The crystal nanorod structures of the manganese oxide materials were further investigated by high-resolution transmission electron microscopy (HR-TEM) to prove the structure of cryptomelane. **Figure 4.3** showed the TEM images of HM-DCM, HM-PCR, and HM-PSF. All the three materials showed crystalline structures with clear lattice fringes which can be indexed as the (110) plane of the cryptomelane manganese oxide with a consistent interplanar *d*-spacing of 6.94 Å. The (110) planes parallel to the long side of nanorods revealed that the manganese oxide nanorods grew along the *c*-axis despite no matter what different oxidants were used. This result is consistent with the findings of Yuan et al. and Zhao et al.[5,8]

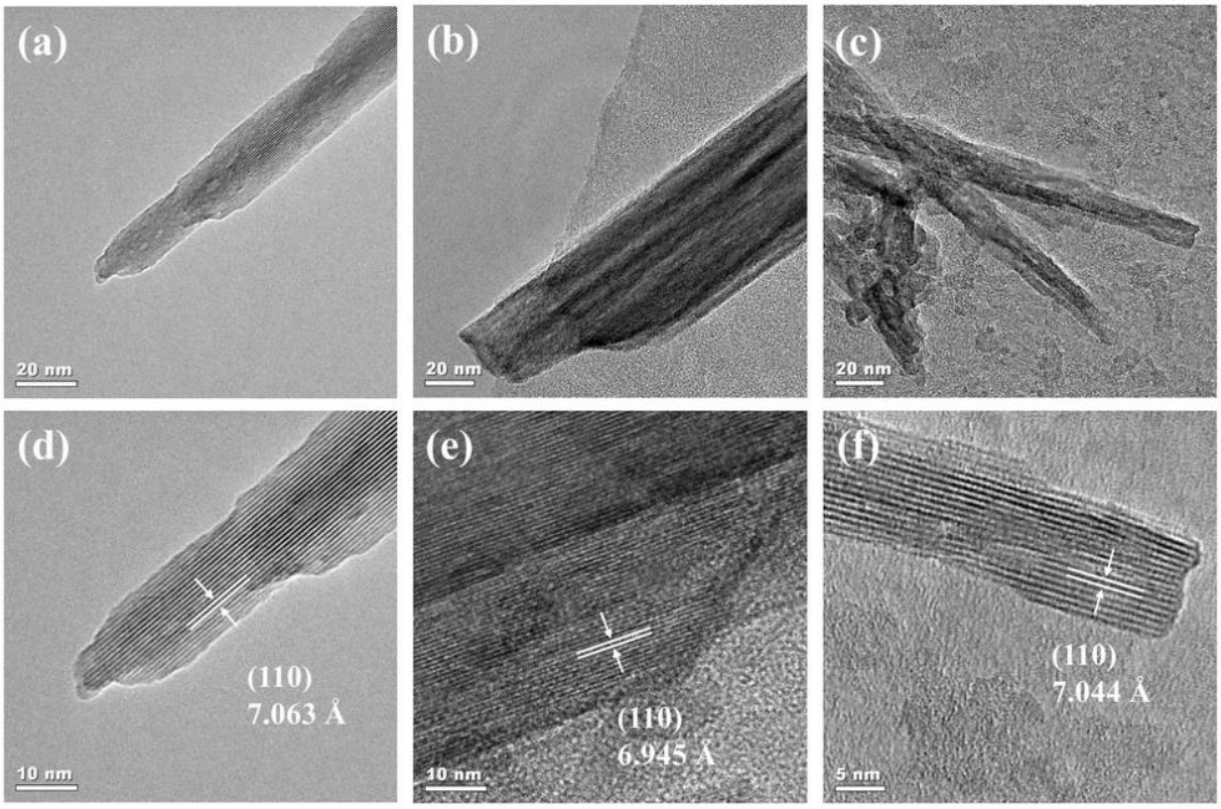

Figure 4.3 HR-TEM images of manganese oxide nanorods scratched from the as-synthesized monolithic cordierite substrate for (a) & (d) HM-DCM, (b) & (e) HM-PCR, and (c) & (f) HM-PSF.

The BET surface areas of all monolithic manganese oxide catalysts and uncoated cordierite honeycomb monolith substrates are listed in **Table 4.1**. Monolithic catalysts, HM-DCM and HM-PCR presented higher surface areas (87 m^2/g and 43 m^2/g) than HM-PSF (7 m^2/g). Because cordierite substrates suffered varying degrees of acid etching during synthesis, the surface area of substrates in each catalyst were measured after removal of coated manganese oxide by the oxalic acid solution. After subtracting the surface area of cordierite substrate using **Equation 4.1**, the nano-array based catalysts, HM-DCM maintained higher surface area (138 m^2/g) from the long

lengths and small diameters. Both nano-array based catalysts, HM-DCM (138 m^2/g) and HM-PSF (54 m^2/g), obtained higher surface areas than their powder based catalysts, PVP-DCM (18 m^2/g) and PVP-PSF (34 m^2/g), indicating the enhanced surface areas from their array architectures. An apparent thick seed layer shown in **Figure 4.1(e)** caused the lower surface area of the HM-PCR (56 m^2/g), which has the longest length and the smallest diameter of nanorods, than the PVP-PCR (97 m^2/g). This kind of seed layer was not shown on the powder based monolithic catalysts, PVP-DCM, PVP-PCR, and PVP-PSF (**Figure 4.4**).

$$S_A = \frac{S_M \times W_M - S_{BC} \times W_{BC}}{W_A} \qquad \textbf{(Equation 4.1)}$$

In the **Equation 4.1**, S_A and W_A are the surface area and weight of manganese oxide nano-array loading on the cordierite substrate, respectively. The S_M and W_M are used for the whole monolithic catalyst, and the S_{BC} and W_{BC} refer to the uncoated cordierite substrate.

Table 4.1 Crystal Information and Brunauer–Emmett–Teller (BET) surface area (S, m^2/g)

	Crystal structure	MnO_x loading on substrate (%)[a]	S_M of monolithic catalyst sample	S_{BC} of MnO_x removed substrate	Calculated S_A of active material
Bare substrate	Cordierite	n/a	0.5	n/a	n/a
HM-DCM	Cryptomelane	13	87	79	138
HM-PCR	Cryptomelane & nsutite	19	43	41	56
HM-PSF	Cryptomelane	8	7	3	54
PVP-DCM	Cryptomelane & Bixbyite	5	11	10	18
PVP-PCR	Cryptomelane	3	12	9	97
PVP-PSF	Cryptomelane	6	22	21	34
PVP-C-MnO_2[b]	Akhtenskite	8	7	6	24

[a] The specific volume of the substrate was 4 pieces of nano-array based monolithic catalysts (2 mm × 2 mm × 10 mm). [b] Commercial manganese oxide. The n/a entries signify not applicable or measured.

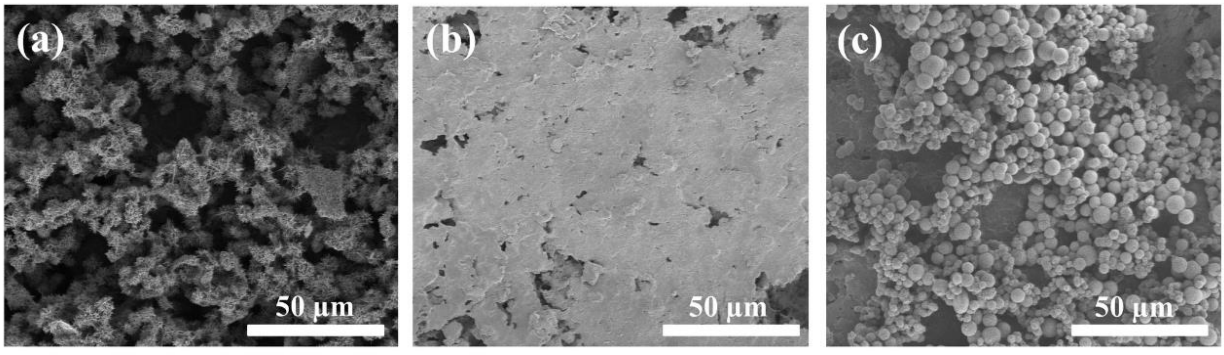

Figure 4.4 SEM images of manganese oxide powders deposited on the cordierite substrates using dip-coating methods: (a) PVP-DCM; (b) PVP-PCR; (c) PVP-PSF.

4.2.3 Surface composition and oxidation state (XPS)

The XPS spectra of surface elemental compositions for Mn 2p and O 1s are illustrated in **Figure 4.5**. The binding energies (BEs) corresponding to the peaks of Mn $2p_{3/2}$, $2p_{1/2}$, and O 1s are summarized in **Table 4.2**. The O 1s peaks were deconvoluted into three oxygen species, lattice oxygen (O_L) from manganese oxide, surface adsorbed oxygen (O_{ads}) in the form of a hydroxyl group (OH^-), and surface adsorbed water molecules (O_W).[9] The average oxidation state (AOS) of Mn in the three materials were calculated from the ratio of Mn $2p_{3/2}$ to O_L. The spectra of Mn $2p_{3/2}$ are difficult to be distinguished between Mn^{3+} and Mn^{4+}, but the increasing BEs for Mn $2p_{3/2}$ signals of the catalysts HM-DCM (642.11 eV), HM-PCR (642.46 eV), and HM-PSF (642.53 eV) agreed with the order of the AOS for Mn, HM-DC (3.67) < HM-PCR (3.74) < HM-PSF (3.83).

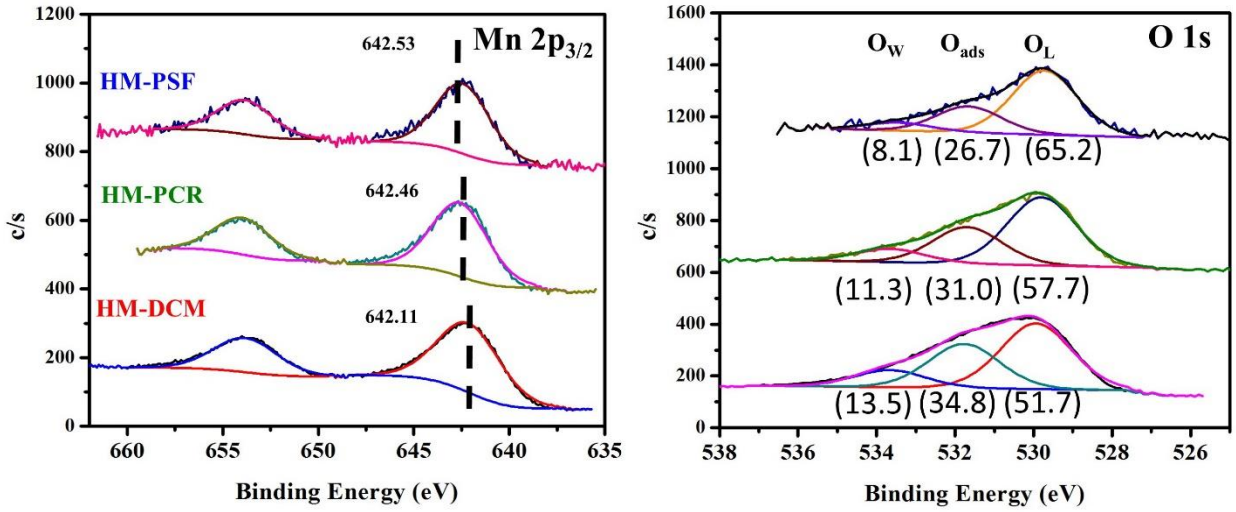

Figure 4.5 X-ray photoelectron spectroscopy (XPS) analysis of (a) Mn 2p and (b) O 1s deconvoluted spectra of manganese oxide collected from each hydrothermal reaction.

Table 4.2 Summary of Binding Energies and Area Percentage of Mn and O Obtained from the Deconvoluted XPS Spectra.

	Binding Energy (eV)						
	Mn 2p		O 1s (%)				
Sample ID	$2p_{3/2}$	$2p_{1/2}$	O_L	O_{ads}	O_W	O/Mn ratio	AOS of Mn
HM-DCM	642.11	653.81	529.94 (51.71)	531.77 (34.83)	533.66 (13.46)	1.84	3.67
HM-PCR	642.46	653.95	529.79 (57.72)	531.69 (31.01)	533.65 (11.27)	1.87	3.74
HM-PSF	642.53	653.83	529.72 (65.18)	531.66 (26.67)	533.45 (8.15)	1.97	3.83

[a] O_L, O_{ads}, and O_W represent the deconvoluted O 1s peak of lattice oxygen, surface adsorbed oxygen species, and surface adsorbed water molecules, respectively.

4.3 Catalytic Performance (CO oxidation)

The catalytic performance of the nano-array based monolithic catalysts was studied by the oxidation of carbon monoxide (CO) with a space velocity of 7,500 h^{-1} as shown in **Figure 4.6(a)**. The HM-PSF catalyst exhibited the best reactivity for CO oxidation with the light-off temperature at 175°C and temperature for 90% conversion (T_{90}) around 200°C. The HM-DCM and HM-PCR catalysts had light-off temperatures around 250°C and 90% conversion (T_{90}) at 300°C & 325°C, respectively. Both HM-PSF and HM-PCR were able to maintain full CO conversion at high temperature (500°C) revealing their good thermal durability. However, for the HM-DCM catalyst, the conversion decreased at 350°C due to the transformation of manganese oxide from the cryptomelane structure (MnO_2) to bixbyite (Mn_2O_3) under feed gas atmosphere.

In order to compare the catalytic performances of catalysts with and without the array structure, the powder based monolithic catalysts loaded with commercial MnO_2 powders and the same manganese oxide materials from hydrothermal reactions were dip-coated with polyvinylpyrrolidone (PVP) as a binder, respectively. The polymer binder was used to deposit manganese oxide powders on the cordierite substrate after a simple calcination for binder removal. Compared with the dip-coated commercial MnO_2 (PVP-C-MnO_2), nano-array based monolithic materials exhibited better catalytic performance than the commercial MnO_2 material. HM-DCM and HM-PSF showed 25°C and 125°C lower conversion temperatures (T_{90}) than the commercial PVP-C-MnO_2, respectively. As shown in **Figure 4.6(a)**, the other three powder based catalysts, PVP-DCM, PVP-PCR, and PVP-PSF showed relative lower reactivity than those of the nano-array based catalysts. The temperature at which PVP-PSF reached full conversion was 100°C higher than the HM-PSF. The other catalysts, PVP-DCM and PVP-PCR have a maximum CO conversion of only ~47% and ~26% before 500°C.

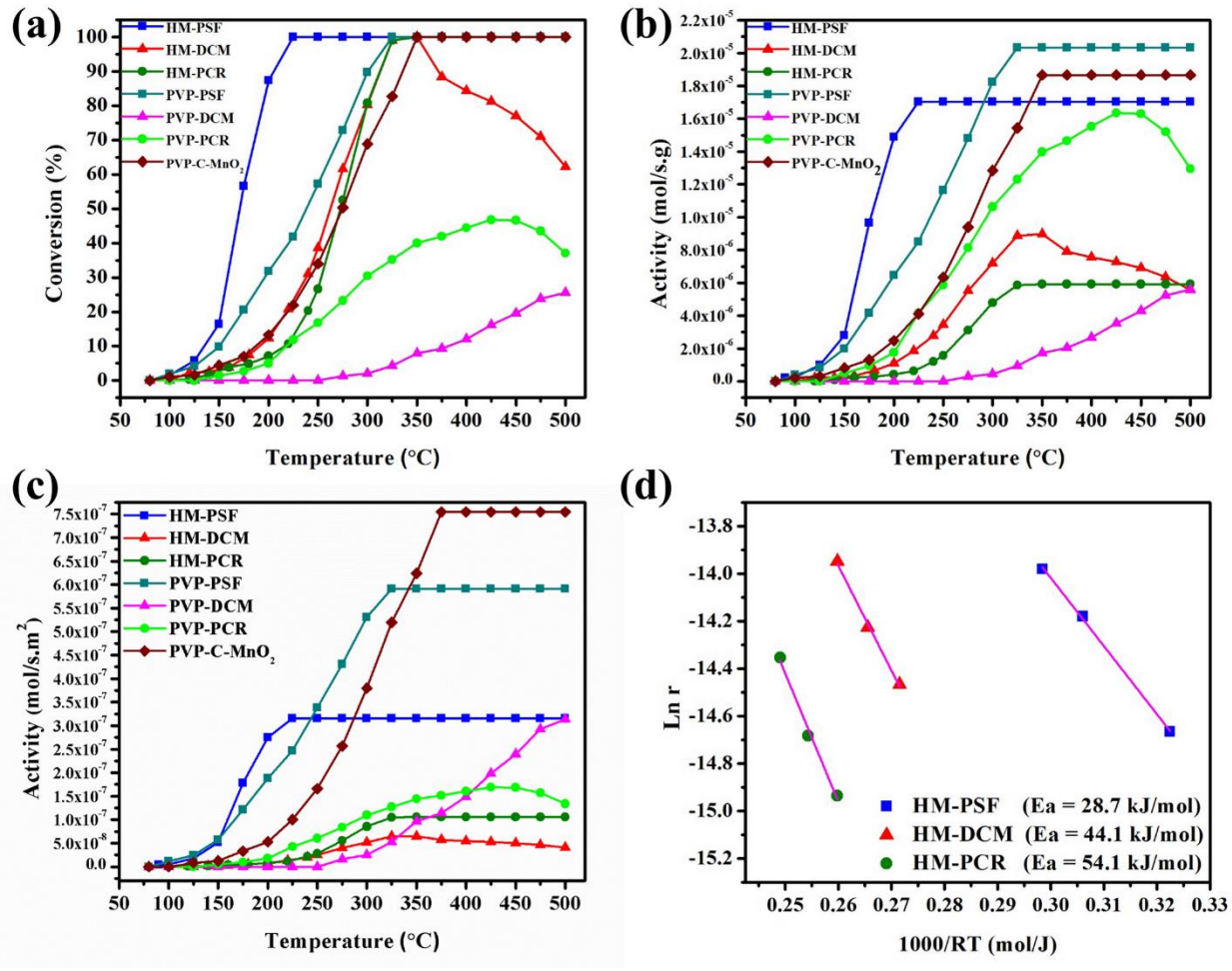

Figure 4.6 (a) Catalytic performance of manganese oxide nano-array based and dip-coated monolithic catalysts for CO oxidation; (b) the calculated activities as a function of the temperature; (c) the calculated activities normalized by surface area as a function of the temperature; (d) the Arrhenius plot of the reaction kinetics and the calculated activation energies.

The loading ratios and surface area of manganese oxides on the cordierite substrates were varied due to different synthetic processes, with HM-PCR (~19%, 56 m^2/g) > HM-DCM (~13%, 138 m^2/g) > HM-PSF (~8%, 54 m^2/g). Therefore, their activities were compared after normalization with the exact weight [**Figure 4.6(b)**] and surface area [**Figure 4.6(c)**]. As shown

in **Figure 4.6(b)**, the calculated activity order of nano-array based catalysts was HM-PSF > HM-DCM > HM-PCR. The HM-PSF and HM-DCM catalysts both displayed higher activities than their powder based counterparts, PVP-PSF and PVP-DCM, indicating the beneficial function of open surfaces due to the array architectures. The two catalysts synthesized using potassium persulfate, HM-PSF, and PVP-PSF, obtained the highest reactivity for CO oxidation. The plot of activities normalized by the surface area in **Figure 4.6(c)** revealed the activity of the HM-PCR catalyst had a similar activity to the PVP-PCR catalyst.

The Arrhenius plots in **Figure 4.6(d)** provided calculated activation energies of the three catalysts from 15% conversions in the sequence of HM-PSF > HM-DCM > HM-PCR. The HM-PSF catalyst showed smaller activation energy (~ 28.7 kJ/mol) than HM-DCM (~ 44.1 kJ/mol) and HM-PCR (~ 54.1 kJ/mol) which correlates with the order of both catalytic performance and calculated activities.

4.4 Temperature Programmed Reduction and Desorption Studies (TPR and TPD)

Hydrogen Temperature Programmed Reduction (H_2-TPR)

As reduction catalysts for CO oxidation, the reactivity of catalysts can be evaluated by their reducibility under hydrogen atmosphere.[10,11] Therefore, temperature programmed reduction (TPR) experiments were conducted to study the relative reducibility among the three monolithic catalysts. As shown in **Figure 4.7(a)**, the TPR profile of the catalyst HM-PSF exhibited a starting temperature of the hydrogen consumption at around 200°C. Two major reduction peaks corresponding to temperatures at 375°C and 500°C can be attributed to the two-step reduction of MnO_2 to Mn_2O_3 ($Mn^{4+} \rightarrow Mn^{3+}$) and Mn_2O_3 to Mn_3O_4 ($Mn^{3+} \rightarrow Mn^{2+}$), respectively.[11] For HM-

DCM, the TPR profile showed only one broad peak of hydrogen consumption between 425 - 550°C, which can be considered as the overlap of the two-step reductions, and higher starting temperature than HM-PSF at around 275°C. The HM-PCR catalyst showed a slight H_2 consumption between 350 - 550°C and a major consumption peak after 550°C, which indicated the lowest reducibility and reactivity of HM-PCR among the three catalysts. Overall, the results of reducibility also showed agreement with the reactivity following the order of HM-PSF > HM-DCM > HM-PCR.

Oxygen Temperature Programmed Desorption (O_2-TPD)

The oxygen desorption tests of each manganese oxide catalyst were characterized with temperature programmed desorption (TPD) to study the desorbed oxygen species from the active materials. In general, the oxygen peak in the TPD profile can be classified as low temperature (200-400°C), medium temperature (400-600°C), and high temperature (above 600°C).[12] As shown in **Figure 4.7(b)**, the oxygen peak in the low-temperature region was ascribed to the evolution of chemisorbed oxygen species weakly bonded on the material surface (O^- and O_2^-). The oxygen peak shown in the medium and high-temperature regions were due to the oxygen evolved from the lattice layer near the catalyst surface and bulk lattice oxygen, respectively.[13] In the medium temperature region, a clear broad peak was observed for HM-PSF from 400 to 575°C, which revealed a dominant amount of near-surface lattice oxygen. The profile of HM-DCM also showed a small peak at around 500°C. For HM-PCR, the oxygen peak was visible but weakly resolved. In the high-temperature region, the bulk lattice oxygen peaks for three catalysts were detected in the sequence of HM-PSF (630°C) < HM-PCR (670°C) < HM-DCM (675°C), which could be related to the Mn-O bond strengths of these catalysts.[14]

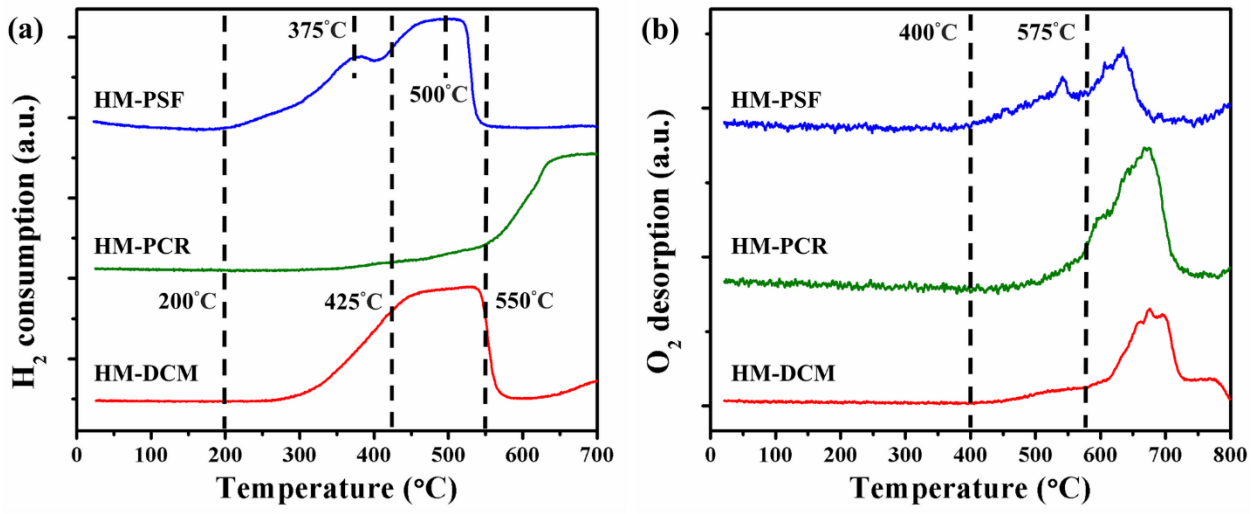

Figure 4.7 (a) H_2-TPR profiles and (b) O_2-TPD profiles of HM-DCM, HM-PSF, and HM-PSF.

4.5 Robustness Test

All nano-array based and powder based monolithic catalysts were sonicated in water for 10 h using a Branson 3210 Ultrasonic Cleaner with 50 kHz frequency. As shown in **Figure 4.8**, the three nano-array based monolithic catalysts maintained 90% coating of active materials on the substrates even after 10 h sonication, but the three dip-coated monolithic catalysts lose more than 65% of the coated materials with only 2 h sonication.

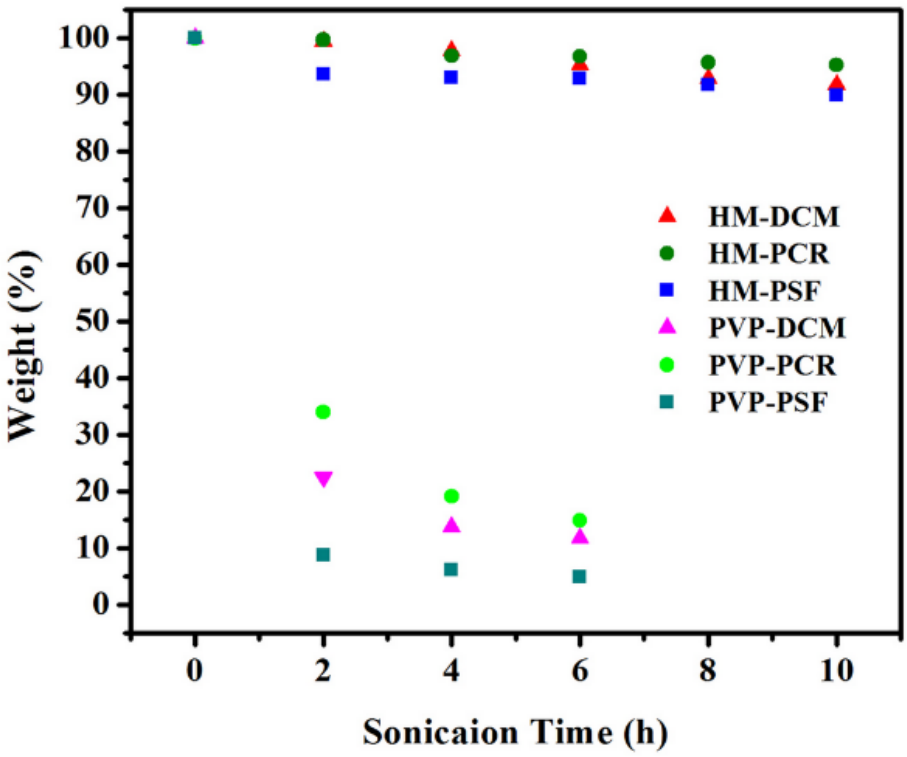

Figure 4.8 Weight measurement of nano-array based and powder based monolithic catalysts after sonication in water.

4.6 Preliminary Study of Continuous Flow Synthesis for Scaling-up Nanoarray-Based Monolithic Catalysts

In general, manganese oxide nanoarrays can be synthesized using chemical vapor deposition (CVD), electrochemical deposition (ED), and chemical bath deposition (CBD) with or without templates, e.g. anodic aluminum oxide (AAO) and carbon nanotubres (CNTs). Those synthetic techniques limit the sizes of the desired devices due to the volume of reactors, like heating chamber of CVD, and solution bath of ED and CBD. For the nanoarray-based monolithic catalysts, the sizes of monolithic catalysts are also depending on the capacity of the reactor used in the designed hydrothermal reactions. In order to fit pratical industrial manufactorring process,

a scalable synthetic strategy is important for the fabrication of nanoarrays on the cordierite substrates. Compared to CVD and ED techniques, solution process is usually considered as a more cost-effective and scalable method for nanomaterial synthesis.[15] Therefore, a system of continuous flow synthesis based on a water bath heator was designed by Gao and co-workers in order to scale-up reaction for bigger cordierite substrates.[16] By this continuous flow system, uniform ZnO nanoarrays with average lengths ~ 10 μm were in situ grown on cordierite substrates with diameters ~ 5 inch using a continuous flow synthesis and homogeneously covered inside the channels of honeycomb monoliths.

The manganese oxide nanoarrays grown by solution based reactions were already demonstrated by our previous results. A similar equipmental setup of continuous flow synthesis as shown in **Figure 4.9** was built up for continuous flow synthesis of MnO_2 nanoarrays.

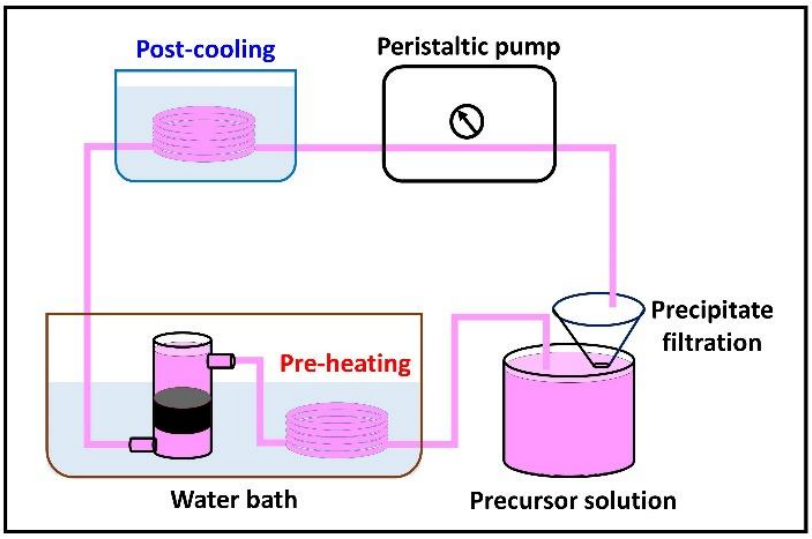

Figure 4.9 Schematic diagram of the continuous flow synthetic system.

Figures 4.10(a) and **4.10(b)** exhibited the size and exterior of cordierite substrate used in the continuous flow synthesis of manganese oxide nanoarrays. The cordierite substrate was shaped to a cylindrical monolith with a 2 inch (~ 5.08 cm) diameter and 1 inch (~ 2.54 cm) height. In **Figures 4.10(c)-(f)**, the random picked four spots of manganese oxide nanoarrays grown on cordierite display consistent morphologies, which indicate the setup of continuous flow synthesis can scale-up the synthetic process of MnO_2 nanoarrays.

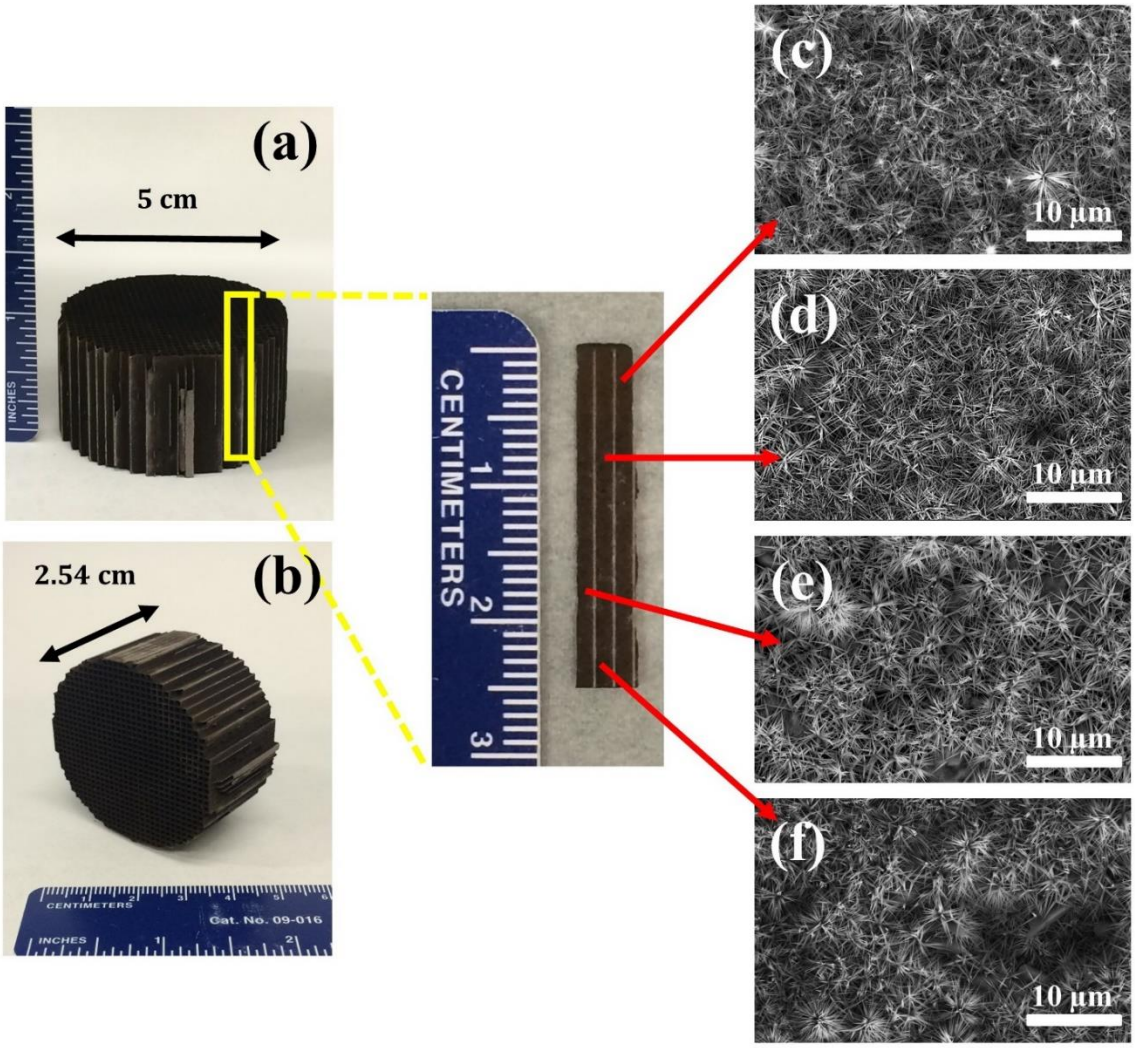

Figure 4.10 (a) and (b) the exterior of cylindrical cordierite honeycomb monoliths. (c) - (f) SEM images of uniformly covered MnO_2 nanoarrays the monolithic substrate synthesized by continuous flow synthesis.

4.7 Discussion

Different oxidants significantly influenced the morphology, crystal structure, and catalytic performance of manganese oxide nanorods. The differences in redox potential between manganese ion and oxidants determined the growth rate of manganese oxide crystals. The redox potential of $Cr_2O_7^-/Cr^{3+}$ (1.33V) which was slightly higher than Mn^{4+}/Mn^{2+} (1.23 V) resulted in a slow reaction rate. The hydrothermal method also provided a mild and stable environment for the growth of highly crystalline prism rods. The chlorate anion had a higher reduction potential (ClO_3^-/Cl_2, 1.49 V) than the dichromate and prompted the faster growing rate. Among the three oxidants, manganese oxides with the longest nanorods (~ 5 μm) were synthesized using potassium chlorate. Potassium persulfate can synthesize nanorods in a shorter time (< 6 h) by its high reduction potential ($S_2O_8^{2-}/SO_4^{2-}$, 2.01 V).

Among all the monolithic catalysts under study, the nano-array based catalysts presented better CO reactivity than the powder based catalysts as shown in **Figure 4.6(a)**. The thermal removal of polymer binder using dip-coating methods might lead to an insufficient loading of manganese oxides on cordierite substrates and thus decreased CO conversion of the catalysts of PVP-DCM and PVP-PCR. Even with normalization by the loading weight in **Figure 4.6(b)**, the catalysts HM-PSF and HM-DCM still exhibited higher activities than PVP-PSF and PVP-DCM, respectively. These results indicated that the open access feature of the nano-array based catalysts is helpful to promote the catalytic performance of monolithic catalysts compared to the dip-coated catalysts. The lower activity of HM-PCR than PVP-PCR shown in **Figure 4.6(b)** is due to a thick seed layer deposited on the cordierite substrate, which was clearly shown in the array structure [**Figure 4.1(e)**] while barely seen in the powder structure [**Figure 4.1(h)**]. The seed layer occupied the majority of manganese oxide weight loading and contributed little activity to CO oxidation.

The normalized activity of HM-PCR in **Figure 4.6(c)** was higher than most catalysts revealing the significant effect from material loading and surface area. For the DCM series, the declined activity of HM-DCM after 350°C was due to its lower thermal stability and structural transformation from cryptomelane to bixbyite. This phenomenon explained the low activity of PVP-DCM after the removal of the binder at 400°C.

For nano-array based monolithic catalysts, the HM-PSF catalyst presented superior reactivity with a 100°C lower light-off temperature around 175°C than HM-DCM and HM-PCR (275°C). The HM-DCM presented higher reactivity than HM-PCR after their activities were normalized by the loading weight and surface area of active materials in **Figure 4.6(c)**. The order of reactivity is HM-PSF > HM-DCM > HM-PCR. Morphology and surface areas of monolithic catalysts did not show direct relationships to the order of catalytic performance. The HM-DCM with the highest surface area (138 m^2/g) revealed lower reactivity for CO oxidation than HM-PSF with the lowest surface area (54 m^2/g). This result indicated there are more factors that control the reactivity of the monolithic catalysts in this study.

In **Figure 4.7(a)**, the H_2-TPR profiles revealed that the initial consumption of hydrogen for HM-PSF started at a lower temperature (~200°C) than HM-DCM (~300°C) and HM-PCR (~400°C) and demonstrated that HM-PSF possesses higher reducibility of lattice oxygen and reactivity for CO. The sequence of reducibility agreed with the normalized reactivity profiles [**Figure 4.6(b)**] and the calculated activation energies in **Figure 4.6(d)** [HM-PSF (28.7 kJ/mol) < HM-DCM (44.1 kJ/mol) < HM-PCR (54.1 kJ/mol)].

Further studies of O_2-TPD and XPS provided more information to investigate the superior catalytic reactivity of HM-PSF. As revealed in former research on CO oxidation by manganese

oxides, the reactivity was influenced by multiple factors, e.g. surface adsorbed oxygen, oxidation states of manganese, and lattice oxygen.[17,18] Physically adsorbed oxygen species on the surface of the catalyst, e.g. O^{2-}, O^{-}, and O_2^{2-}, were usually considered as an aid for the gaseous oxidation.[19] The O_2-TPD profile of the HM-PSF in Figure 5(b) presented a clear desorption peak between 400 - 575°C indicating higher amounts of surface adsorbed oxygen than the other two catalysts which benefitted the reactivity of CO oxidation. The other intense peaks in the higher temperature region (above 575°C) corresponded to desorption of lattice oxygen from manganese oxides. The lower releasing temperature of lattice oxygen for HM-PSF exhibited weaker Mn-O bonding strengths and labile lattice oxygen which also led to the higher reducibility and CO reactivity.

The XPS results listed in **Table 4.2** summarizes the binding energies (BEs) of Mn $2p_{3/2}$ and the oxygen components for each manganese oxide catalyst. Although the spectra of the Mn $2p_{3/2}$ were difficult to identify the amounts of Mn^{2+}, Mn^{3+}, and Mn^{4+}, the increasing BEs of Mn $2p_{3/2}$ for HM-DCM (642.11 eV), HM-PCR (642.46 eV), and HM-PSF (642.53 eV) had the same tendency as the ratios between Mn and O, HM-DCM (1.84), HM-PCR (1.87), and HM-PSF (1.97), which suggested the O/Mn ratios and average oxidation states of manganese oxide increased with the reduction potential of oxidant. Meanwhile, the higher manganese valence (Mn^{4+}) led to more surface adsorbed oxygen species and contributed to the CO oxidation.[9] Data for HM-PSF with the highest manganese state and obvious surface adsorbed oxygen from the O_2-TPD test among the three catalysts are in line with this correlation of oxidation state and activity. Comparing the deconvoluted lattice oxygen signals (O_L) from O 1s spectra, the descending BEs and ascending percentages for HM-DCM (529.94 eV, 51.71%), HM-PCR (529.79 eV, 57.72%), and HM-PSF (529.72 eV, 65.18%) demonstrated that increasing reduction potentials of oxidants cause certain effects on the lattice oxygen in manganese oxide crystals. The higher percentages and lower

binding energies of surface lattice oxygen in HM-PSF showed weaker Mn-O bonding strengths important for CO oxidation, which agrees with the Mars-van-Krevelen mechanism that the surface lattice oxygens of manganese oxide should be the major oxygen source in CO oxidation.[20,21]

Preliminary attempts of continuous flow synthesis for nanoarray fabrication showed promising results to scale up the manganese oxide nanoarray-based monolithic catalysts. However, extra precipitation of manganese oxide was found in the solution transferring tubing and the bottom of the reactor. This phenomenon indicates the nucleation of manganese oxide not only occurred on the cordierite substrates but also within precursor solution, which might be due to the lengthy tubing and a higher temperature. Therefore, the flow rate and bath temperature of continuous flow synthesis should be adjusted to narrow the region of nucleation and grow nanoarrays on the substrates more precisely.

4.8 Conclusion

A synthetic strategy was developed to integrate nanorod arrays based on urchin-like manganese oxide nanostructures onto channeled cordierite honeycomb monoliths. This one-pot hydrothermal synthesis displayed the great potential to fabricate promising monolithic catalysts for exhaust removal with good catalytic performance, high robustness, and scalability. Compared to powder based manganese oxide monolithic catalysts, a series of nano-array based catalysts, i.e., HM-DCM, HM-PCR and HM-PSF possessed promoted catalytic performance due to increased surface areas from their array architectures. The HM-PSF catalyst synthesized using potassium persulfate as oxidant showed high reducibility with a low activation energy (28.7 kJ/mol), and 90% conversion of CO oxidation before 200°C (T_{90}). The HM-DCM and HM-PCR can also reach

full conversion at 325°C. Correlating the results of O_2-TPD and XPS to the CO oxidation tests, the relative higher ratio of the amount of lattice oxygen to that of surface adsorbed oxygen was found to be the dominant factor, which contributed to the highest reactivity of HM-PSF among the three manganese oxide monolithic catalysts.

4.9 References

(1) Li, D.; Yang, J.; Tang, W.; Wu, X.; Wei, L.; Chen, Y. *RSC Adv.* **2014**, *4*, 26796-26803.

(2) Sun, M.; Lan, B.; Lin, T.; Cheng, G.; Ye, F.; Yu, L.; Cheng, X.; Zheng, X. *CrystEngComm* **2013**, *15*, 7010-7018.

(3) Wu, C.; Xie, Y.; Wang, D.; Yang, J.; Li, T. *J. Phys. Chem. B* **2003**, *107*, 13583-13587.

(4) Wu, Q.; Tao, H.; Xie, K.; Liu, N.; Yu, L.; Hu, Z. *J. Mater. Chem.* **2011**, *21*, 17904-17908.

(5) Yuan, J.; Li, W.-N.; Gomez, S.; Suib, S. L. *J. Am. Chem. Soc.* **2005**, *127*, 14184-14185.

(6) Guo, Y.; Ren, Z.; Xiao, W.; Liu, C.; Sharma, H.; Gao, H.; Mhadeshwar, A.; Gao, P.-X. *Nano Energy* **2013**, *2*, 873-881.

(7) Sibo, W.; Zheng, R.; Wenqiao, S.; Yanbing, G.; Mingwan, Z.; Steven, L. S.; Pu-Xian, G. *Catal. Today* **2015**, *258*, 549-555.

(8) Zhao, X. D.; Fan, H. M.; Luo, J.; Ding, J.; Liu, X. Y.; Zou, B. S.; Feng, Y. P. *Adv. Funct. Mater.* **2011**, *21*, 184-190.

(9) Tang, W.; Wu, X.; Li, D.; Wang, Z.; Liu, G.; Liu, H.; Chen, Y. *J. Mater. Chem. A* **2014**, *2*, 2544.

(10) Liang, S.; Teng, F.; Bulgan, G.; Zong, R.; Zhu, Y. *J. Phys. Chem. C* **2008**, *112*, 5307-5315.

(11) Poyraz, A., S.; Song, W.; Kriz, D.; Kuo, C.-H.; Seraji, M. S.; Suib, S. L. *ACS Appl. Mater. Interfaces* **2014**, *6*, 10986-10991.

(12) Yin, Y.-G.; Xu, W.-Q.; DeGuzman, R.; Suib, S. L.; O'Young, C. *Inorg. Chem.* **1994**, *33*, 4384-4389.

(13) Iyer, A.; Galindo, H.; Sithambaram, S.; King'ondu, C.; Chen, C.-H.; Suib, S. L. *Appl. Catal., A* **2010**, *375*, 295-302.

(14) Makwana, V. D.; Garces, L. J.; Liu, J.; Cai, J.; Son, Y.-C.; Suib, S. L. *Catal. Today* **2003**, *85*, 225-233.

(15) Gao, P.-X.; Shimpi, P.; Gao, H.; Liu, C.; Guo, Y.; Cai, W.; Liao, K.-T.; Wrobel, G.; Zhang, Z.; Ren, Z. *Int. J. Mol. Sci.* **2012**, *13*, 7393-7423.

(16) Wang, S.; Ren, Z.; Guo, Y.; Gao, P.-X. *CrystEngComm* **2016**, *18*, 2980-2993.

(17) Njagi, E. C.; Chen, C.-H.; Genuino, H.; Galindo, H.; Huang, H.; Suib, S. L. *Appl. Catal., B* **2010**, *99*, 103-110.

(18) Ramesh, K.; Chen, L.; Chen, F.; Liu, Y.; Wang, Z.; Han, Y.-F. *Catal. Today* **2008**, *131*, 477-482.

(19) Song, W.; Poyraz, A. S.; Meng, Y.; Ren, Z.; Chen, S.-Y.; Suib, S. L. *Chem. Mater.* **2014**, *26*, 4629-4639.

(20) Luo, Y.; Deng, Y.-Q.; Mao, W.; Yang, X.-J.; Zhu, K.; Xu, J.; Han, Y.-F. *J. Phys. Chem. C* **2012**, *116*, 20975-20981.

(21) Xie, Y.; Yu, Y.; Gong, X.; Guo, Y.; Guo, Y.; Wang, Y.; Lu, G. *CrystEngComm* **2015**, *17*, 3005-3014.

Chapter 5. Copper Manganese Oxide Enhanced Nanoarray-Based Monolithic Catalysts for Hydrocarbons Oxidations

5.1 Introduction

In this study, copper manganese oxide ($CuMn_2O_4$) and nanoarray architecture were combined to form $CuMn_2O_4$/nanoarray-based monolithic catalysts and evaluated by propane (C_3H_8) oxidation. The previously reported manganese oxide nanoarray, HM-PCR, was grown on the cordierite substrate as core supports without using any binder.[1] $CuMn_2O_4$ and cobalt ion (Co^{2+}) doped $CuMn_2O_4$ were precipitated on HM-PCR nanoarrays by mild hydrothermal reactions for uniform coatings and denoted as NA-$CuMn_2O_4$, NA-$Co_{0.36}Cu_{0.64}Mn_2O_4$, and NA-$Co_{0.53}Cu_{0.47}Mn_2O_4$ depending on the composition tests by inductively coupled plasma-mass spectrometry (ICP-MS). All three catalysts possessed $CuMn_2O_4$ based compositions with low crystallinity and nearly amorphous phases and high conversion of hydrocarbon oxidations. Incorporation of trace cobalt ions led to Cu replacement by Co, enhanced reactivity at low temperature, increased surface area, faster precipitation rate, and compromised thermal stability. To understand the catalytic contribution from nanoarray structures, monolithic catalysts loaded with the same $CuMn_2O_4$ and $Co_xCu_{1-x}Mn_2O_4$ materials were prepared by a wash-coating method using alumina powder (α-Al_2O_3) as support. An additional Pd-loaded catalyst was used to compare with PGMs-based catalysts as well. Further studies of nitrogen isothermal adsorption, X-ray photoelectron spectroscopy (XPS), and hydrogen temperature-programmed reduction (H_2-TPR) showed that there was increased surface area and lattice oxygen mobility of Co-doped $CuMn_2O_4$ catalysts that were correlated closely to the catalytic performance.

5.2 Characterization Studies of $CuMn_2O_4$ Coated Nano-Arrays Based Monolithic Catalysts

5.2.1 Morphology of Nano-Arrays (SEM)

The core manganese oxide nanoarrays, HM-PCR, were fabricated on the cordierite honeycomb monoliths following previous work as shown in **Figure 5.1(a)**, **5.1(e)**, and **5.1(i)**. The HM-PCR nanoarrays had average lengths of ~ 5 μm and diameters of ~ 50 nm. Through hydrothermal reactions, transition metal oxide layers of $CuMn_2O_4$, and Co-doped $CuMn_2O_4$ ($Co_{0.36}Cu_{0.64}Mn_2O_4$ and $Co_{0.53}Cu_{0.47}Mn_2O_4$) were coated uniformly on the HM-PCR nanoarrays without influencing the array architectures, **Figure 5.1(b)-(d)** and **Figure 5.1(f)-(h)**. The cross-section SEM images shown in **Figure 5.1(j)-(l)** revealed that all three $CuMn_2O_4$ materials were coated uniformly upon each nanorod of HM-PCR nanoarrays from top to bottom. All HM-PCR nanorod arrays inside the channels of cordierite substrates were fully covered by the coatings. The thickness of all of the $CuMn_2O_4$ coatings is controllable by adjusting reaction conditions of hydrothermal synthesis, i.e. temperature, time, concentration, and Co amount. In general, the average thickness of the $CuMn_2O_4$ coating can reach 100 nm with 30 h hydrothermal reaction, but only 4 h with addition of 1% Co and 1 h with 2% Co, respectively. Both core nanoarrays and $CuMn_2O_4$ coatings were stable on cordierite substrates without obvious detachment after 2 h of sonication in water.

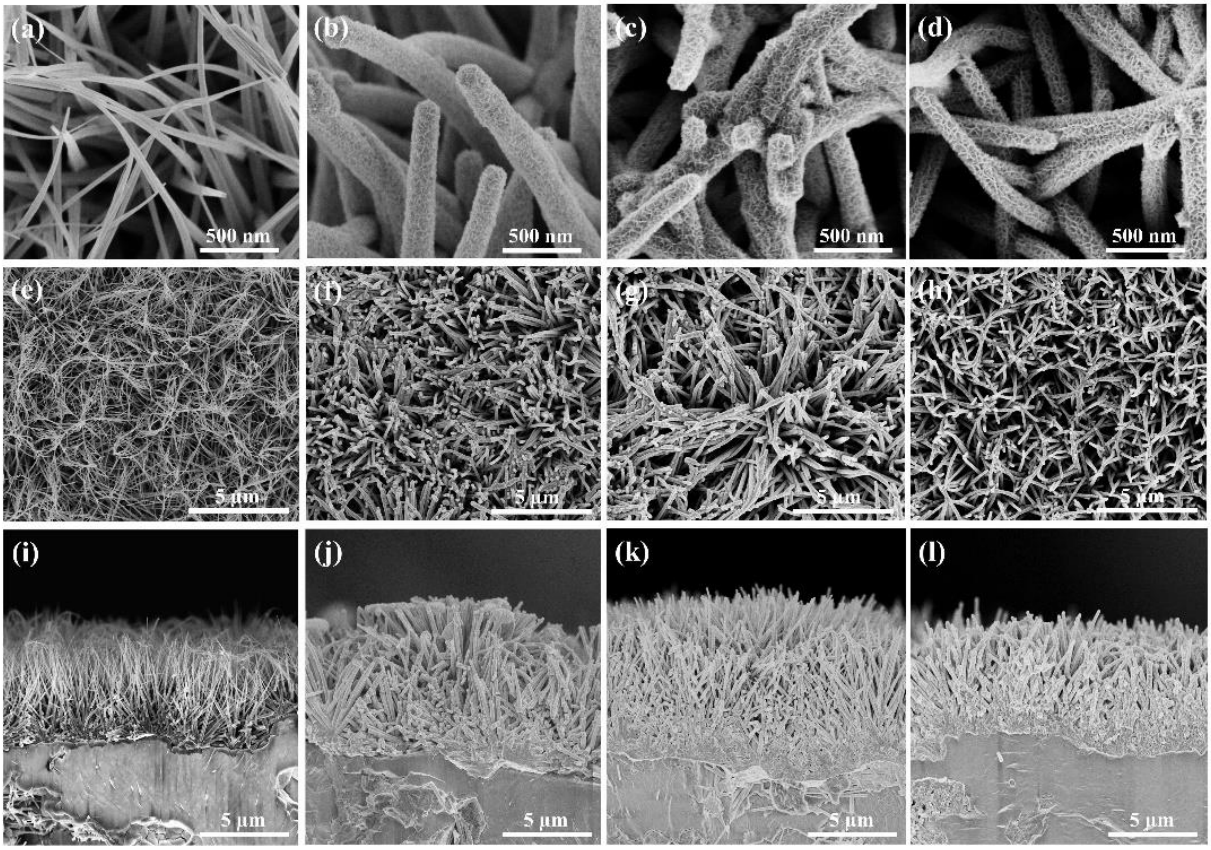

Figure 5.1 SEM images of nanoarrays HM-PCR with and without $CuMn_2O_4$ coatings by on the cordierite substrate. Column (a) HM-PCR, (b) NA-$CuMn_2O_4$, (c) NA-$Co_{0.36}Cu_{0.64}Mn_2O_4$, and (d) NA-$Co_{0.53}Cu_{0.47}Mn_2O_4$. Upper and middle rows showed top-view images; lower row showed cross-section images.

5.2.2 Crystal Structure (XRD & TEM)

X-ray diffraction (XRD) was conducted on the powders collected from each hydrothermal reaction to identify their crystal structures (**Figure 5.2**), because the intensities of the diffraction patterns from the cordierite substrate were much stronger than the diffraction patterns from the manganese oxide arrays, HM-PCR, and coating material, $CuMn_2O_4$. XRD patterns **Figure 5.2(a)** reveals that the core nanoarrays grown on the cordierite substrates can be indexed to the cryptomelane manganese oxide ($K_{2-X}Mn_8O_{16}$, tetragonal, $a = b = 9.82$ Å and $c = 2.85$ Å, JCPDS: 29-1020). The XRD patterns of $CuMnO_x$ series only display two diffraction peaks at around 36°

and 66° (2θ angle) respectively indexed to the (311) and (531) planes as cubic $CuMn_2O_4$ (JCPDS: 74-2422). With heat treatment to 400 °C, the series of $CuMn_2O_4$ materials still maintained relatively low crystallinity as compared to a traditional spinel crystal structure indicating their near-amorphous structures.[2,3] The XRD patterns of each catalyst calcined at a varied temperature from 300 to 500 °C were shown in **Figure 5.2(b)-(d)**. All three materials started to reveal full diffraction patterns of the hopcalite structure after calcination at 500 °C for 2 h. Two diffraction peaks of MnO_2 at around 13° and 66° respectively indexed to the (110) and (310) planes were only shown in the two Co-doped catalysts.

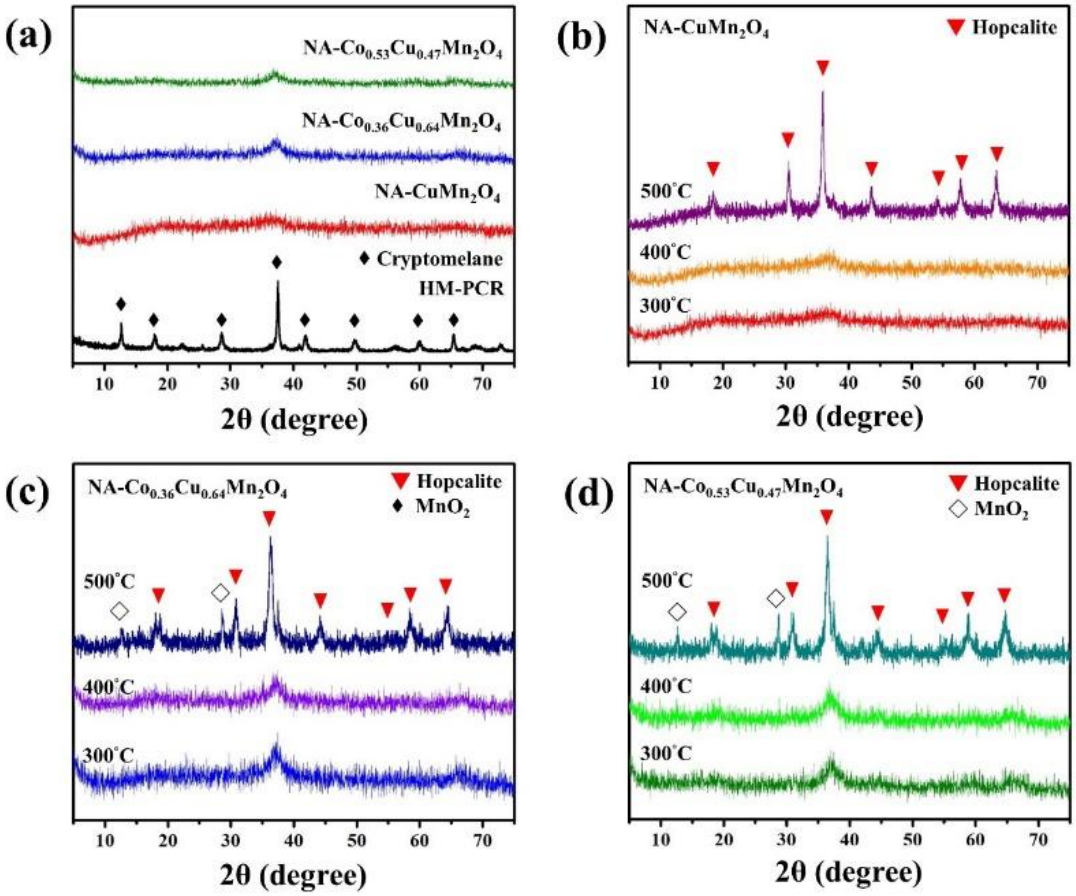

Figure 5.2 (a) XRD patterns of each powder collected from HM-PCR, NA-$CuMn_2O_4$, NA-$Co_{0.36}Cu_{0.64}Mn_2O_4$, and NA-$Co_{0.53}Cu_{0.47}Mn_2O_4$ coating reactions. And XRD patterns of (b) NA-$CuMn_2O_4$, (c) NA-$Co_{0.36}Cu_{0.64}Mn_2O_4$, and (d) NA-$Co_{0.53}Cu_{0.47}Mn_2O_4$, calcined at 300, 400, and 500 °C.

In **Figures 5.3(a) – (c)**, the transmission electron microscopy (TEM) studies exhibit that all three $CuMn_2O_4$ coatings were composed by tiny nanosheets and grown uniformly along the nanorods of HM-PCR. **Figures 5.3(d) – (f)** reveal that the average sizes of nanosheets are bigger with an increasing amount of Co ions. The TEM images confirm that $CuMn_2O_4$ coatings are not completely amorphous but still difficult to measure the lattice fringes of $CuMn_2O_4$ nanosheets.

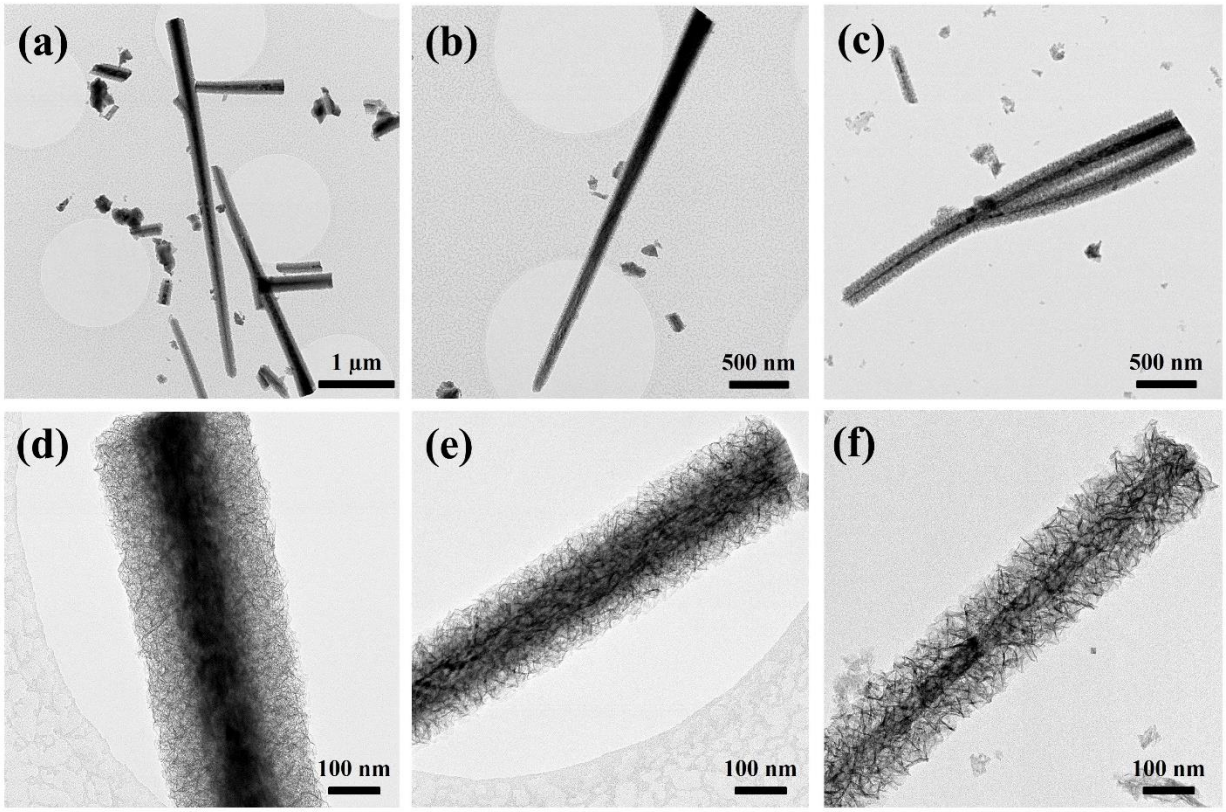

Figure 5.3 HR-TEM images of manganese oxide nanorods scratched from the as-synthesized monolithic cordierite substrate for (a) & (d) NA-$CuMn_2O_4$, (b) & (e) NA-$Co_{0.36}Cu_{0.64}Mn_2O_4$, and (c) & (f) NA-$Co_{0.53}Cu_{0.47}Mn_2O_4$.

5.2.3 Elemental Compositions (ICP-MS)

Studies of XRD and TEM reveal all three copper manganese oxides from hydrothermal reactions possessing low crystallinity and are nearly amorphous. ICP-MS tests were conducted to analyze the elemental ratios between Cu and Mn of each copper manganese oxides. **Table 5.1** lists elemental ratios (Mn, Cu, K, and Co) of each copper manganese oxide material. The Cu to Mn ratio of undoped copper manganese oxide (NA-$CuMn_2O_4$) was closed to 1 : 2, which indicated its chemical formula should be identified as $CuMn_2O_4$. For the Co-doped $CuMn_2O_4$ materials, the percentage of Cu decreased dramatically with an increasing amount of Co ions, but the percentage of Mn only had a slight change. The detected Co ions from NA-$Co_{0.36}Cu_{0.64}Mn_2O_4$ and NA-$Co_{0.53}Cu_{0.47}Mn_2O_4$ are almost ten times the designed amounts showing that the Co-O-Mn was preferred to be formed during the hydrothermal reaction rather than Cu-O-Mn. These results are consistent with the general concept that Co^{2+} can replace Cu^{2+} in tetrahedral sites and Co^{3+} can substitute for Mn^{3+} in octahedral sites of the $CuMn_2O_4$ lattice.[4]

Table 5.1 Elemental components of $CuMn_2O_4$ based coating layers (%).

Sample ID	Mn	Cu	Co	Total
NA-$CuMn_2O_4$	64.9	35.1	-	100.0
NA-$Co_{0.36}Cu_{0.64}Mn_2O_4$	65.7	22.1	12.3	100.0
NA-$Co_{0.53}Cu_{0.47}Mn_2O_4$	64.0	16.9	19.2	100.0

The - entries signify not applicable or measured.

5.2.4 Surface Area (BET)

Table 5.2 Average Weight (W, g/L), loading percentages (%) of active materials, and Brunauer–Emmett–Teller (BET) surface areas (SA, m^2/g)

Sample ID	Support material type	Average W of monolith catalysts (g/L)	W% of materials loading on monolithic substrates (%) [a]			SA of monolithic catalysts (m^2/g)	SA of MO removed substrates (m^2/g)	SA' of active materials (m^2/g)
			$CuMn_2O_4$	Support	Total			
Uncoated cordierite substrate	-		-	-	-	0.5	-	-
MnO_2 array (HM-PCR)	-	492	-	-	15	36	40	10
NA-$CuMn_2O_4$	HM-PCR	596	12	15	27	35	35	63
NA-$Co_{0.36}Cu_{0.64}Mn_2O_4$	HM-PCR	612	9	13	22	37	31	126
NA-$Co_{0.53}Cu_{0.47}Mn_2O_4$	HM-PCR	564	9	9	18	43	27	218
α-Al_2O_3 powder (commercial)	-	-	-	-		-	-	26
WC-$CuMn_2O_4$	α-Al_2O_3	808	8	31	39	12	-	46
WC-$Co_{0.36}Cu_{0.64}Mn_2O_4$	α-Al_2O_3	852	8	34	42	15	-	75
WC-$Co_{0.53}Cu_{0.47}Mn_2O_4$	α-Al_2O_3	806	8	31	39	17	-	113

[a] All MnO_2 and $CuMn_2O_4$ materials were removed by aqueous oxalic acid solution.

The - entries signify not applicable or measured.

Table 5.2 summarizes the weight loading percentages and surface areas (SA) of both nanoarray-based monolithic catalysts and wash coated monolithic catalysts. Nanoarray-based monolithic catalysts with $CuMn_2O_4$ coatings have surface areas between 35-43 m^2/g, and wash coated monolithic catalysts are around 12-17 m^2/g. Overall, the surface areas of all monolithic catalysts follow the order of NA-$Co_{0.53}Cu_{0.47}Mn_2O_4$ > NA-$Co_{0.36}Cu_{0.64}Mn_2O_4$ > NA-$CuMn_2O_4$.

However, both nanoarray-based and wash coated monolithic catalysts have a portion of the surface area contributed by their core support, MnO_2 nanoarrays, and α-Al_2O_3, respectively. The cordierite substrates of nanoarray core, HM-PCR also have a partial etching by acid during hydrothermal reactions. Therefore, the surface areas of the core supports and uncoated substrates (cordierite) were subtracted from the surface area of nanoarray-based and wash-coated monolithic catalysts using respectively **Equations 5.1** and **5.2** to obtain the recalculated surface area of $CuMn_2O_4$ coatings and powders (SA').

$$S_{Array} = \frac{S_M \times W_M - S_{BC} \times W_{BC} - S_{PCR} \times W_{PCR}}{W_{Array}} \quad \textbf{(Equation 5.1)}$$

$$S_{WC} = \frac{S_M \times W_M - S_{BC} \times W_{BC} - S_{AlO} \times W_{AlO}}{W_{WC}} \quad \textbf{(Equation 5.2)}$$

In **Equations 5.1** and **5.2**, S_{Array} and W_{Array} are the surface areas and weights of $CuMn_2O_4$ material coatings on the HM-PCR core nanoarrays, respectively; S_{WC} and W_{WC} are used for the wash coated monolithic catalysts; S_M and W_M are used for the whole monolithic catalysts; S_{BC} and W_{BC} refer to the uncoated cordierite substrate; S_{PCR} and W_{PCR} refer to the core nanoarrays, HM-PCR; S_{AlO} and W_{AlO} refer to the α-Al_2O_3 support powder.

After subtraction of core supports and cordierite substrates, the recalculated surface area of the $CuMn_2O_4$ coatings show the same trend as monolithic catalysts, NA-$Co_{0.53}Cu_{0.47}Mn_2O_4$ > NA-$Co_{0.36}Cu_{0.64}Mn_2O_4$ > NA-$CuMn_2O_4$, but the surface areas of $CuMn_2O_4$ coatings applied on nanoarray-based monolithic catalysts are much higher than $CuMn_2O_4$ powders on wash coated monolithic catalysts, i.e. NA-$Co_{0.53}Cu_{0.47}Mn_2O_4$ (218 m^2/g) > WC-$Co_{0.53}Cu_{0.47}Mn_2O_4$ (113 m^2/g). Correlating the surface areas to their morphologies in **Figure 5.1**, the results indicates that the

$CuMn_2O_4$ coatings on nanoarray architectures are able to maintain high surface-to-volume ratio (**Figure 5.1(d)-(f)**) rather than aggregation to large particles as shown in **Figures 5.1(g)-(i)**.

5.2.5 Surface composition and oxidation state (XPS)

XPS was used to obtained detailed valence states of the major component in these catalysts. Spectra in **Figure 5.4** illustrate the surface elemental compositions of the powder collected from hydrothermal coating reactions of NA-$CuMn_2O_4$, NA-$Co_{0.36}Cu_{0.64}Mn_2O_4$, and NA-$Co_{0.53}Cu_{0.47}Mn_2O_4$. All binding energies (BEs) correspond to the peaks of Mn 2p, Cu 2p, Co 2p, and O 1s and are summarized in **Table 5.3**. In **Figure 5.4(a)**, the Mn $2p_{3/2}$ peaks at around 641 eV indicate that the Mn^{3+} is the majority of Mn in each $CuMn_2O_4$ material.[5] The Cu 2p spectra in **Figure 5.4(b)** are characterized by the peaks of Cu $2p_{3/2}$ (932 eV) and Cu $2p_{1/2}$ (952 eV), and observable satellite peaks at around 940 eV and 962 eV, which correspond to Cu^{2+}; with no obvious peaks from Cu^0 and Cu^+ detected.[6,7] In **Figure 5.4(c)**, the respective Co $2p_{3/2}$ and Co $2p_{1/2}$ peaks at around 780 eV and 795 eV are accompanied with satellite peaks at 786 eV and 806 eV due to the major valence of Co to Co^{2+}.[7] Detectable shoulders at around 782 eV indicate the minor existence of Co^{3+} in catalysts. The Shirley function was not applied to correct the background of Cu 2p and Co 2p spectra due to the overlap of Mn LMM (945 eV) and Mn 2s peaks (772 eV), respectively. The O 1s spectra in **Figure 5.4(d)** were deconvoluted into three Gaussian peaks due to oxygen bonding of Cu-O (529.4 eV), Mn-O (531.4 eV), and surface adsorbed oxygen species (532.5 eV, i.e. OH^-).[5]

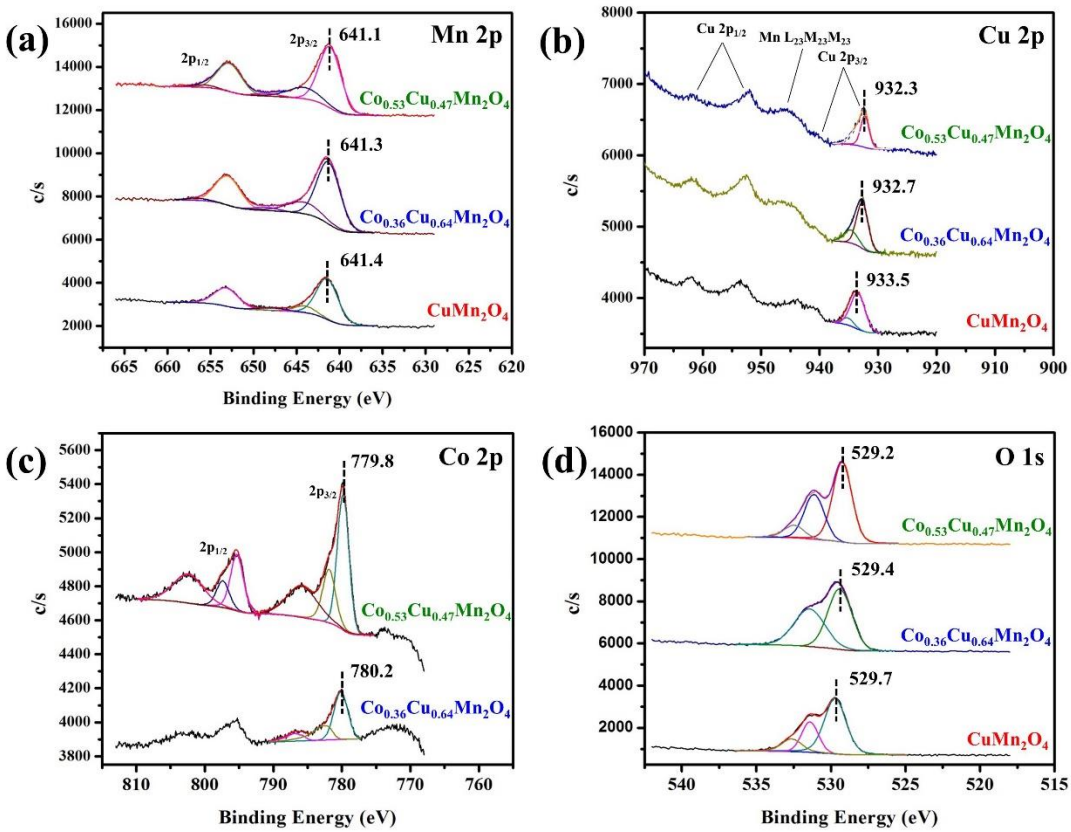

Figure 5.4 X-ray photoelectron spectroscopy (XPS) analysis of (a) Cu 2p and (b) Mn 2p of $CuMn_2O_4$ and $Co_{0.36}Cu_{0.64}Mn_2O_4$ collected from each hydrothermal reaction.

Table 5.3 Summary of Binding Energies (BEs) of Cu, Mn, and Co from the XPS Spectra

Sample ID	Binding Energy (eV)							
	Mn $2p_{3/2}$ (%)		Cu $2p_{3/2}$	Co $2p_{3/2}$ (%)		O 1s (%)		
	Mn^{3+}	Mn^{4+}	Cu^{2+}	Co^{2+}	Co^{3+}	O_{Cu}	O_{Mn}	O_{Mn}
NA-$CuMn_2O_4$	641.4 (85.2)	644.0 (14.8)	933.5	-	-	529.7 (62.2)	531.4 (24.1)	532.6 (13.7)
NA-$Co_{0.36}Cu_{0.64}Mn_2O_4$	641.3 (76.3)	644.2 (23.7)	932.7	780.2 (68.3)	782.2 (31.7)	529.4 (54.6)	531.4 (45.4)	-
NA-$Co_{0.53}Cu_{0.47}Mn_2O_4$	641.1 (76.9)	644.1 (23.1)	932.3	779.8 (67.6)	781.9 (32.4)	529.2 (58.5)	531.1 (32.1)	532.5 (9.4)

The - entries signify not applicable or measured.

5.2.6 Thermal Stability (TGA)

Thermogravimetric analysis (TGA) studies of the three powder-form materials collected from each hydrothermal reaction are shown in **Figure 5.5** with sample weight percentage as a function of temperature. The TGA profiles show a weight loss between 25 and 200 °C that is due to the release of physisorbed water molecules. The slight weight change between 200 and 400 °C is due to the evolution of lattice oxygen near the surface. The weight loss between 450 and 550 °C was caused by the crystallization of hopcalite ($CuMn_2O_4$) and spinel (Mn_3O_4) according to XRD patterns at high temperature. $Co_{0.36}Cu_{0.64}Mn_2O_4$ shows more weight loss as compared to $CuMn_2O_4$ and $Co_{0.53}Cu_{0.47}Mn_2O_4$ indicating lower thermal stability among the three materials.

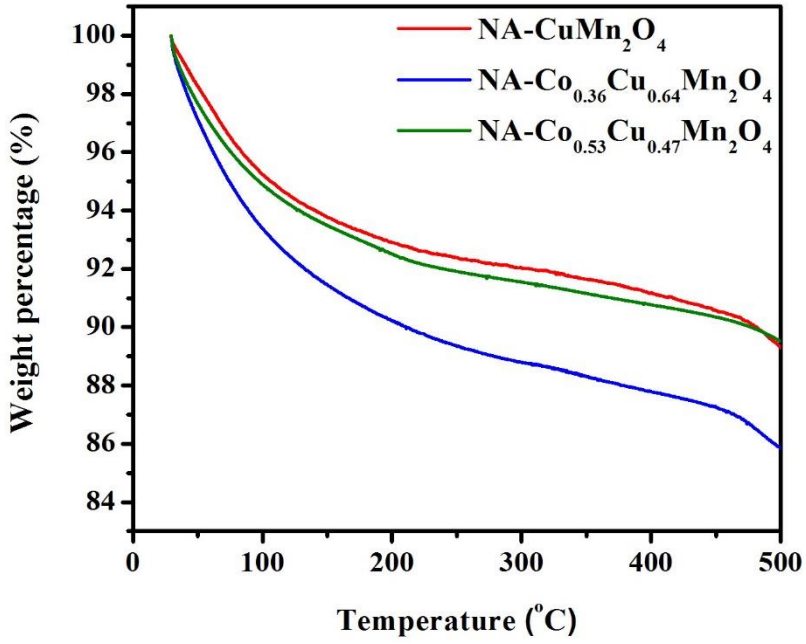

Figure 5.5 Thermogravimetric analysis (TGA) of coating materials, $CuMn_2O_4$, $Co_{0.36}Cu_{0.64}Mn_2O_4$, and $Co_{0.53}Cu_{0.47}Mn_2O_4$ collected from each hydrothermal reaction.

5.3 Catalytic Performance (C_3H_8 Oxidations)

The catalytic performance of the $CuMn_2O_4$ coated nanoarray-based, and wash-coated monolithic catalysts were studied using propane (C_3H_8) with a space velocity of 24,000 h^{-1} as shown in **Figure 5.6(a)** compared to a Pd/α-Al_2O_3 wash-coated monolithic catalyst and core array, HM-PCR. In general, the nanoarray-based monolithic catalysts had better catalytic performance than both Pd and $CuMn_2O_4$ wash-coated monolithic catalysts. All the three $CuMn_2O_4$ coated nanoarray-based monolithic catalysts, NA-$CuMn_2O_4$, NA-$Co_{0.36}Cu_{0.64}Mn_2O_4$, and NA-$Co_{0.53}Cu_{0.47}Mn_2O_4$ possessed good reactivity with light-off temperature (T_{50}) around 300°C, 25 °C lower than the wash-coated catalysts, WC-$Co_{0.36}Cu_{0.64}Mn_2O_4$ (325°C) and 50 °C lower than NA-$CuMn_2O_4$ and the Pd loaded catalyst, WC-Pd (350°C). Among the three nanoarray-based monolithic catalysts, the NA-$CuMn_2O_4$ presented the highest reactivity to C_3H_8 oxidation and reached 90% conversion at 400°C, which was 50 °C lower than the Co-doped catalysts, NA-$Co_{0.36}Cu_{0.64}Mn_2O_4$ and NA-$Co_{0.53}Cu_{0.47}Mn_2O_4$ (450°C).

For a comparison among wash-coated monolithic catalysts, the catalyst loaded $CuMn_2O_4$ powders also revealed better catalytic performance than the Pd loaded catalyst. The wash-coated catalyst, WC-$CuMn_2O_4$, had similar T_{50} with WC-Pd around 360°C, but lower T_{90} (450 °C < 500°C). The catalysts with Co doping were able to increase conversion at the lower temperature region and obtain a T_{50} at 325°C. The temperature of nanoarray-based catalysts for 90% conversion (T_{90}) was around 400°C, at least 25 °C lower than the wash-coated catalysts, WC-$CuMn_2O_4$ (450°C), WC-$Co_{0.36}Cu_{0.64}Mn_2O_4$ (475°C), and WC-Pd (475°C).

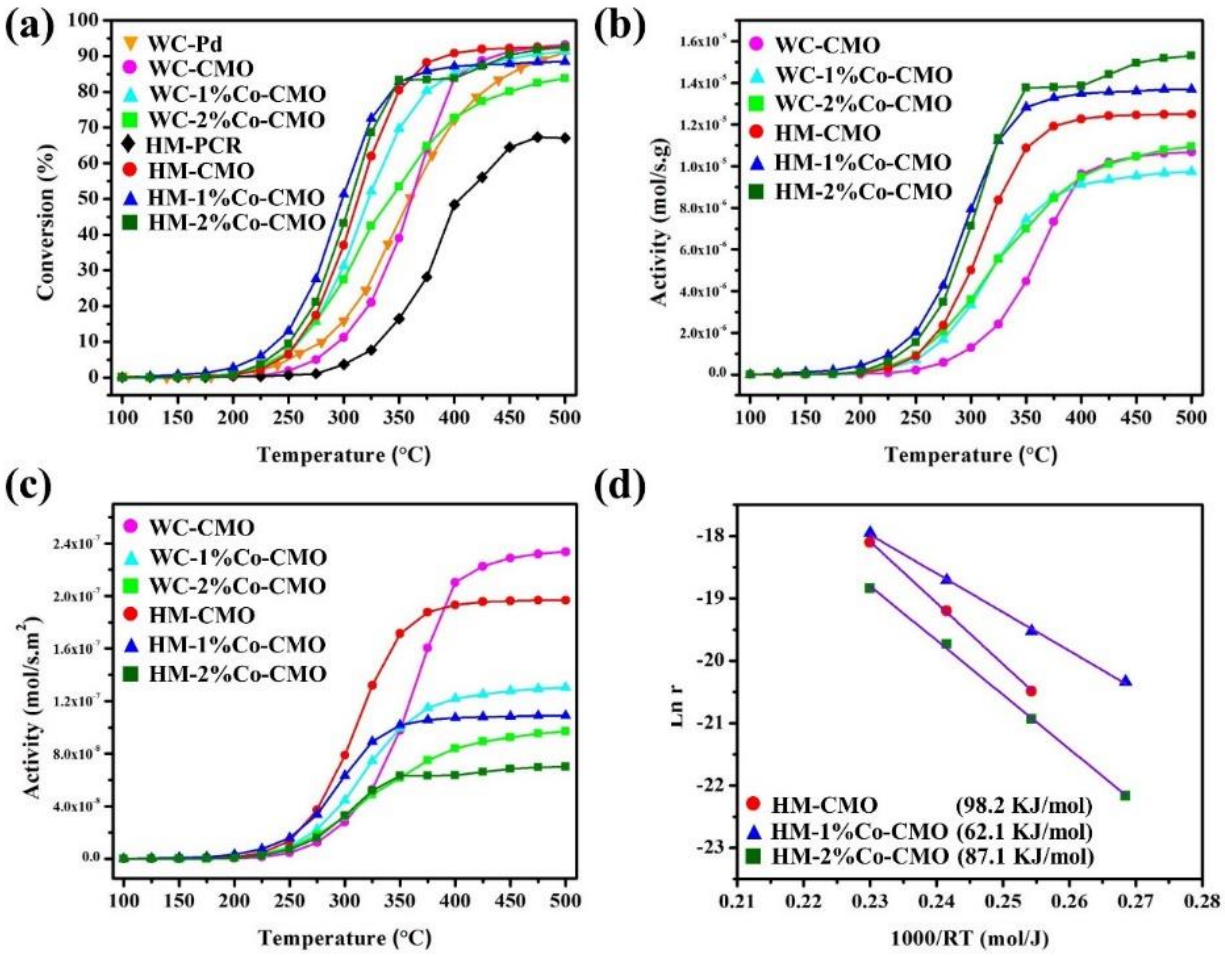

Figure 5.6 (a) Catalytic performance of nanoarray-based and wash-coated monolithic catalysts for C_3H_8 oxidation; (b) the calculated activities as a function of temperature; (c) the calculated activities normalized by surface area as a function of temperature; (d) the Arrhenius plot of the reaction kinetics and the calculated activation energies.

Due to different precipitation, rates and the loading ratio of $CuMn_2O_4$ from hydrothermal reactions and wash-coating, the conversion curves of monolithic catalysts were normalized by loading weight as shown in **Figure 5.6(b)**. With normalization using the exact coating weight, the order of normalized activity was NA-$Co_{0.53}Cu_{0.47}Mn_2O_4$ > NA-$Co_{0.36}Cu_{0.64}Mn_2O_4$ > NA-$CuMn_2O_4$.

Each $CuMn_2O_4$ coated nanoarray-based catalysts still possess higher activities than their wash-coated catalysts, which proves that the nanoarray morphology is enhanced the catalytic performance of C_3H_8 oxidations.

For further comparison among the $CuMn_2O_4$ and Co-doped $CuMn_2O_4$ materials, their activities were normalized simultaneously with both surface area and weight loading amount. **Figure 5.6(c)** shows a totally opposite trend of normalized activities, and NA-$CuMn_2O_4$ reveals a higher activity than Co-doped $CuMn_2O_4$. The order of normalized activity became NA-$CuMn_2O_4$ > NA-$Co_{0.36}Cu_{0.64}Mn_2O_4$ > NA-$Co_{0.53}Cu_{0.47}Mn_2O_4$, which is opposite the order of surface area indicating the importance of the surface area to the catalytic performance in this study.

The calculated activation energies of each monolithic catalyst were summarized in the Arrhenius plot, **Figure 5.6(d)**. Overall, for both nanoarray-based or wash-coated catalysts, monolithic catalysts with cobalt ions doping have lower activation energies than the pure $CuMn_2O_4$ catalysts. For wash-coated catalysts, the activation energies decrease with the increasing doping amount of cobalt ions, WC-$CuMn_2O_4$ (93.1 KJ/mol) > WC-$Co_{0.36}Cu_{0.64}Mn_2O_4$ (90.9 KJ/mol) > WC-$Co_{0.53}Cu_{0.47}Mn_2O_4$ (84.6 KJ/mol). For nanoarray-based catalysts, the order of their activation energies is NA-$CuMn_2O_4$ (98.2 KJ/mol) > NA-$Co_{0.53}Cu_{0.47}Mn_2O_4$ (87.1 KJ/mol) > NA-$Co_{0.36}Cu_{0.64}Mn_2O_4$ (62.1 KJ/mol). The 1% Co-doped nanoarray-based catalyst possesses the lowest activation energy among all catalysts, which agrees with its lowest light-off temperature (~300°C) as shown in **Figure 5.6(a)**.

5.4 Temperature Programmed Reduction and Desorption (TPR & TPD)

Hydrogen Temperature Programmed Reduction (H_2-TPR)

The hydrogen temperature programmed reduction (H_2-TPR) was conducted to study the relative effect of cobalt ion doping on the reducibility of $CuMn_2O_4$ based monolithic catalysts. The two typical consecutive peaks at around 260 °C and 350 °C in **Figure 5.7(a)** show an H_2-TPR profile that is consistent with the results of Jones et al. and Cai et al. and attributed to the reduction of $Cu^{2+} \rightarrow Cu^{+}$ and $Mn^{3+} \rightarrow Mn^{2+}$, respectively.[8,4] The broadened reduction peaks compared to those results is due to the open channel configuration of monolithic samples. In **Figures 5.7(b)** and **4.7(b)**, the reduction of cobalt ions ($Co^{3+} \rightarrow Co^{2+}$) slightly changed the profile shape of $CuMn_2O_4$ and led to diminished troughs around 300 °C and small humps around 350°C. With Co doping, NA-$Co_{0.36}Cu_{0.64}Mn_2O_4$ and NA-$Co_{0.53}Cu_{0.47}Mn_2O_4$ showed relatively lower starting temperatures in H_2-TPR tests, which followed the same tendency as their activation energies, NA-$Co_{0.36}Cu_{0.64}Mn_2O_4$ < NA-$Co_{0.53}Cu_{0.47}Mn_2O_4$ < NA-$CuMn_2O_4$.

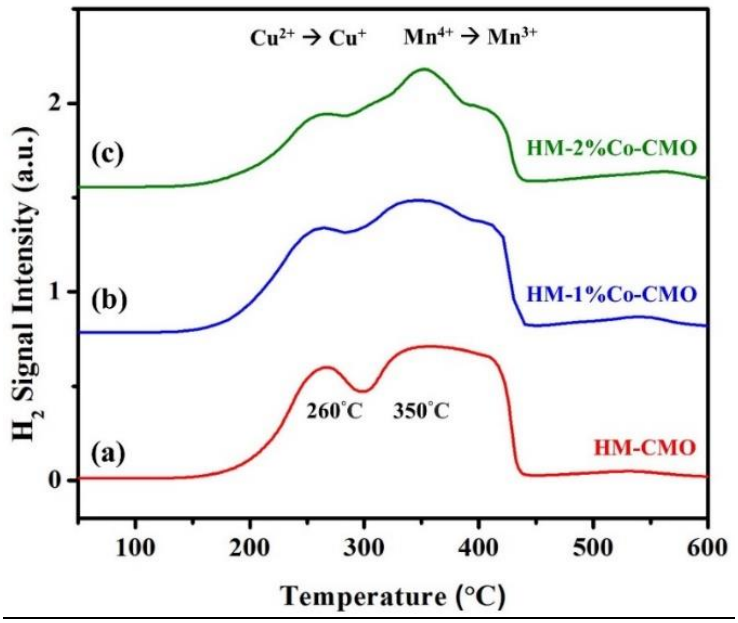

Figure 5.7 H_2-TPR profiles of monolithic catalysts, (a) NA-$CuMn_2O_4$, (b) NA-$Co_{0.36}Cu_{0.64}Mn_2O_4$, and (c) NA-$Co_{0.53}Cu_{0.47}Mn_2O_4$.

Oxygen Temperature Programmed Oxidation (**O_2-TPD**)

The nature of oxygen species in coated $CuMn_2O_4$ materials was investigated using oxygen temperature programmed desorption (O_2-TPD) experiments. Overall, the three catalysts had similar starting temperatures of oxygen evolution around 350°C. Between 350-750°C, each O_2-TPD profile can be separated into three regions: (I) 350-540°C, (II) 540-660°C, and (III) 660-750°C, according to the major desorption peaks.

Figure 5.8(a) of $CuMn_2O_4$ only presents two oxygen desorption peaks in regions I and II, which are due to bulk lattice oxygen evolution from metal-oxygen bonding, Cu-O_L and Mn-O_L. But **Figures 5.8(b)** and **5.8(c)** show that Co-doped $CuMn_2O_4$ catalysts have clear desorption peaks in Region III indicating oxygen evolution from Co-O_L bonding. The relative intensities of desorption peaks in the region I and region III also varied with the change of Cu and Co amounts in the catalysts NA-$Co_{0.36}Cu_{0.64}Mn_2O_4$ and NA-$Co_{0.53}Cu_{0.47}Mn_2O_4$. For example, the NA-$Co_{0.53}Cu_{0.47}Mn_2O_4$ catalyst possesses the smallest amount of copper and highest amount of cobalt compared to the NA-$Co_{0.36}Cu_{0.64}Mn_2O_4$ catalyst. Then the O_2-TPD profile shows a lower intensity peak in the region I and a higher peak in region III as well. Morales et al. also showed an analogous result of the varied ratio between Cu and Mn in Mn_xCu_y mixed oxides.[9] These results indicate that the three regions of lattice oxygen evolution in those O_2-TPD profiles could be distinguished as follows, (i) region I (350-540°C): Cu-O_L, (i) region I (540-660°C): Mn-O_L, and (i) region I (660-750°C): Co-O_L.

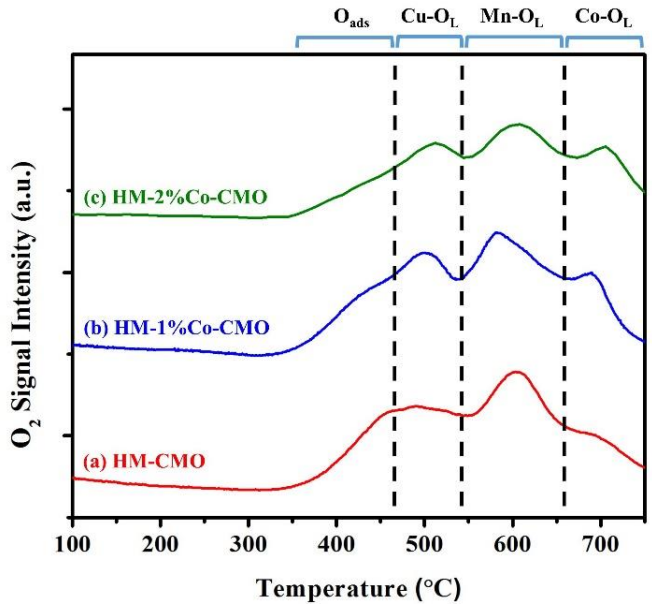

Figure 5.8 O_2-TPD profiles of monolithic catalysts, (a) NA-$CuMn_2O_4$, (b) NA-$Co_{0.36}Cu_{0.64}Mn_2O_4$, and (c) NA-$Co_{0.53}Cu_{0.47}Mn_2O_4$.

5.5 Discussion

5.5.1 Synthesis and morphologies

The cryptomelane MnO_2 nanoarray HM-PCR, synthesized using manganese sulfate ($MnSO_4$) and potassium chlorate ($KClO_3$), was chosen as the core support due to the high length-to-diameter ratio (average length of 5 µm and diameter of 50 nm). The appropriate interspace between the rods provided enough room for the growth of $CuMn_2O_4$ layers without sacrificing the active surface. Additional advantages, like the simple procedure, potential scalability, high robustness, and good stability in hydrothermal reactions ensured that nanoarray HM-PCR never affected the secondary transitional metal oxide coatings during the synthesis.

The mild conditions of the hydrothermal coating synthesis of NA-$CuMn_2O_4$, e.g. neutral solution, low temperature, and slow precipitation rate, led to the uniform and tunable thickness of $CuMn_2O_4$ layers from top to bottom of the whole HM-PCR nanoarrays. The introduction of cobalt ions accelerated the precipitation rate to obtain the same thickness of coating layers in a shorter reaction time. Correlating the elemental ratio between Co and Cu ions in NA-$Co_{0.36}Cu_{0.64}Mn_2O_4$ and NA-$Co_{0.53}Cu_{0.47}Mn_2O_4$ from ICP-MS tests (**Table 5.1**), Co ions replaced the Cu ions in the $CuMn_2O_4$ system due to the more energetically favorable formation of Co-O bonds (ΔH_f = 368 KJ/mol) than Cu-O bonds (ΔH_f = 343 KJ/mol). This resulted in more Co observed in the materials than expected.

5.5.2 Catalytic performance

Propane (C_3H_8) oxidations were conducted to evaluate the catalytic performance of all nanoarray-based and wash-coated monolithic catalysts as shown in **Figure 5.1**. The Pd/Al_2O_3 wassh-coated catalyst (WC-Pd) was used as a state-of-art monolithic catalyst to compare with our $CuMn_2O_4$ coated catalysts. In **Figure 5.6(a)**, all $CuMn_2O_4$ based monolithic catalysts exhibit lower light-off temperatures (T_{50}) and 90% conversion temperatures (T_{90}) than the Pd loaded catalyst, WC-Pd, indicating the high reactivity to hydrocarbons of the $CuMn_2O_4$ coatings.

The promoted activities by open surfaces of nanoarray architectures were examined by comparing the normalized weight activities of both nanoarray-based and wash-coated catalysts shown in **Figure 5.6(b)**. The three nanoarray-based catalysts revealed higher activities of C_3H_8 oxidation than each correlated wash-coated monolithic catalyst. Among the nanoarray-based catalysts, the order of reactivity is NA-$Co_{0.53}Cu_{0.47}Mn_2O_4$ ~ NA-$Co_{0.36}Cu_{0.64}Mn_2O_4$ > NA-$CuMn_2O_4$, as the same tendency as wash-coated catalysts. The two Co-doped catalysts have similar

reactivity but higher than the pure $CuMn_2O_4$ catalyst below 350 °C showing the enhanced reactivity by the incorporation of Co ions in the low-temperature region.[10]

To understand the effect from increased surface area, the reactivity in **Figure 5.6(b)** was further normalized by recalculating the surface area in **Table 5.2** and is illustrated in **Figure 5.6(c)**. The opposite trend of normalized reactivity in **Figure 5.6(c)** indicated that the promoted reactivity of the two Co-doped catalysts was due to the increase of surface area, which was proportional to the amount of Co incorporation.

The calculated activation energies (E_a) were listed in **Figure 5.6(d)** with the increasing order NA-$Co_{0.36}Cu_{0.64}Mn_2O_4$ (62.1 KJ/mol) < NA-$Co_{0.53}Cu_{0.47}Mn_2O_4$ (87.1 KJ/mol) < NA-$CuMn_2O_4$ (98.2 KJ/mol), which has the same tendency with the study of Salker et al. in 2000.[11] $Co_xCu_{1-x}Mn_2O_4$ catalysts were tested with varied Co/Cu ratios (x = 0.0, 0.3, 0.5, 0.7, and 1.0) and indicated the catalysts with x = 0.3 and 0.7 show a relatively higher reactivity than catalysts with x = 0.0, 0.5, and 1.0. Correlating the activation energies of nanoarray-based catalysts to the H_2-TPR profiles, the reduction peak of Co ions (Co^{2+} and Co^{3+}) between Cu^{2+} and Mn^{3+} indicated higher reducibility and oxygen mobility contributing to the lower E_a of Co incorporated catalysts supported by O_2-TPD results. The O_2-TPD study not only shows the relative ratios of Cu-O_L, Mn-O_L, and Co-O_L but are also related to the thermal stability of the catalysts. In **Figure 5.8**, the evolution temperature of the Mn-O_L lattice oxygen from $Co_{0.36}Cu_{0.64}Mn_2O_4$ (583 °C) is lower than the other two materials (604 °C). These results agree with the TGA profiles in **Figure 5.5** showing that the $Co_{0.36}Cu_{0.64}Mn_2O_4$ material with 12% Co exhibited lower thermal stability than the material with higher ($Co_{0.53}Cu_{0.47}Mn_2O_4$, 19%) and lower ($CuMn_2O_4$, 0%) amounts of Co incorporation. The lower evolution temperature of lattice oxygen is due to weaker Mn-O_L bond

strength and higher oxygen mobility, both beneficial to propane oxidations which follow the Mars-van Krevelen mechanism.[12]

Utilizing different supports and preparation methods, the nanoarray-based catalysts showed higher monolithic SA (35 – 43 m^2/g) with less weight percentage of the core nanoarrays (9 – 15%) compared to the wash-coated catalysts with alumina powder support (SA: 12 – 17 m^2/g, loading: 31 – 34%). In addition, the recalculated SA of NA-$Co_{0.53}Cu_{0.47}Mn_2O_4$ from the nanoarray-based catalyst (218 m^2/g) is almost double the SA than the wash-coated catalyst (113 m^2/g). This result indicates that the core nanoarrays provide a good template for $CuMn_2O_4$ to prevent aggregation and efficiently maintain the high surface area, maximizing active sites.

5.5.3 Oxidation States

The XPS study reveals the oxidation states of metal elements near the surface, which play an important role influencing catalytic reactivity. The major oxidation states of Mn, Cu, and Co were determined as Mn^{3+}, Cu^{2+}, and Co^{2+}, respectively, depending on their binding energies (BEs) and corresponding satellite peaks as shown in **Figures 5.4(a)-(c)**. The BEs of Mn^{3+}, Cu^{2+}, and O^{2-} for all catalysts decreased with increased contents of Co^{2+} suggesting that the incorporation of Co might enhance the mobility of lattice oxygen.

For the two Co-doped catalysts, $Co_{0.36}Cu_{0.64}Mn_2O_4$ and $Co_{0.53}Cu_{0.47}Mn_2O_4$, the existence of Mn LMM peaks in Cu 2p spectra [**(Figure 5.4(b)**] and Mn 2s peaks in Co 2p spectra [**(Figure 5.4(c)**] made it more difficult to distinguish the composition of Cu $2p_{3/2}$ and Co $2p_{3/2}$ peaks. However, as shown in **Figure 5.4(c)**, the relatively higher intensity of the Mn 2s signal was obtained from the $Co_{0.36}Cu_{0.64}Mn_2O_4$ catalyst than for $Co_{0.53}Cu_{0.47}Mn_2O_4$ showing that the $Co_{0.36}Cu_{0.64}Mn_2O_4$ material possessed a higher surface concentration of Mn.

In **Figure 5.4(d)**, the O 1s peak of $Co_{0.36}Cu_{0.64}Mn_2O_4$ was only deconvoluted to two well-fitting peaks for lattice oxygens of Cu-O and Mn-O rather than three peaks as with $CuMn_2O_4$ and $Co_{0.53}Cu_{0.47}Mn_2O_4$. This result suggests that the $Co_{0.36}Cu_{0.64}Mn_2O_4$ material had trace surface adsorbed hydroxyl species (OH^-) but a relatively higher percentage of Mn-O (45.4%) than the other two catalysts, $CuMn_2O_4$ and $Co_{0.53}Cu_{0.47}Mn_2O_4$. The order of Mn-O percentage in catalysts, $Co_{0.36}Cu_{0.64}Mn_2O_4$ (45.4%) > $Co_{0.53}Cu_{0.47}Mn_2O_4$ (32.1%) > $CuMn_2O_4$ (24.1%), revealed a reversed tendency of activation energies of monolithic catalysts shown in **Figure 5.4(d),** $Co_{0.36}Cu_{0.64}Mn_2O_4$ (62.1 KJ/mol) < $Co_{0.53}Cu_{0.47}Mn_2O_4$ (87.1 KJ/mol) < $CuMn_2O_4$ (98.2 KJ/mol).

5.6 Conclusion

A series of $CuMn_2O_4$/nanoarray-based monolithic catalysts were successfully fabricated by applying $CuMn_2O_4$ nanosheets to the HM-PCR nanoarrays. The new catalysts have hydrothermal durability and loading capability of HM-PCR nanoarrays for an additional transitional metal oxide layer. The $CuMn_2O_4$/nanoarray-based monolithic catalysts combined the high reactivity of $CuMn_2O_4$ materials and open surface effect of nanoarray architecture to provide better catalytic performance for C_3H_8 oxidation. Compared to wash-coated catalysts, nanoarrays replaced the use of alumina supports and efficiently reduced the integrated weight of monolithic catalysts. The incorporation of cobalt ions increased the material surface area (63 m^2/g → 218 m^2/g) and lower activation energies (98.2 KJ/mol → 62.1 KJ/mol) but compromised the thermal stability. The XPS study showed that the NA-$Co_{0.36}Cu_{0.64}Mn_2O_4$ catalyst had a higher concentration of Mn-O bonding near the material surface, which might contribute to its better catalytic performance. Different from traditional hydrothermal syntheses, all procedures were

conducted in an open system reactor at atmospheric pressure revealing the potential of scalability for industrial manufacturing processes.

5.7 References

(1) Chen, S.-Y.; Song, W.; Lin, H.-J.; Wang, S.; Biswas, S.; Mollahosseini, M.; Kuo, C.-H.; Gao, P.-X.; Suib, S. L. *ACS Appl. Mater. Interfaces* **2016**, *8*, 7834-7842.

(2) Hasegawa, Y.; Fukumoto, K.; Ishima, T.; Yamamoto, H.; Sano, M.; Miyake, T. *Appl. Catal., B* **2009**, *89*, 420-424.

(3) Tang, W.; Wu, X.; Li, S.; Shan, X.; Liu, G.; Chen, Y. *Appl. Catal., B* **2015**, *162*, 110-121.

(4) Jones, C.; Taylor, S. H.; Burrows, A.; Crudace, M. J.; Kiely, C. J.; Hutchings, G. J. *Chem. Commun.* **2008**, 1707-1709.

(5) Zhao, H.; Fang, K.; Zhou, J.; Lin, M.; Sun, Y. *Int. J. Hydrogen Energy* **2016**, *41*, 8819-8828.

(6) Choi, K.-H.; Lee, D.-H.; Kim, H.-S.; Yoon, Y.-C.; Park, C.-S.; Kim, Y. H. *Industrial & Engineering Chemistry Research* **2016**, *55*, 4443-4450.

(7) Wagner, C. D.; Muilenberg, G. *Handbook of X-Ray Photoelectron Spectroscopy*; Perkin-Elmer, 1979.

(8) Cai, L.; Hu, Z.; Branton, P.; Li, W. *Chinese Journal of Catalysis* **2014**, *35*, 159-167.

(9) Morales, M. R.; Barbero, B. P.; Cadús, L. E. *Fuel* **2008**, *87*, 1177-1186.

(10) Lin, H.-J.; Baltrus, J. P.; Gao, H.; Ding, Y.; Nam, C. Y.; Ohodnicki, P.; Gao, P.-X. *ACS Appl. Mater. Interfaces* **2016**, *8*, 8880-8887.

(11) Salker, A.; Gurav, S. *Journal of materials science* **2000**, *35*, 4713-4719.

(12) Ren, Z.; Wu, Z.; Song, W.; Xiao, W.; Guo, Y.; Ding, J.; Suib, S. L.; Gao, P.-X. *Appl. Catal., B* **2016**, *180*, 150-160.

Chapter 6. Conclusions

In this study, a synthetic strategy based on urchin-like manganese oxide nanostructures was developed to synthesize manganese oxide nanoarrays on 2D and 3D substrates. Two series of nanoarray-based monolithic catalysts were fabricated using cryptomelane nanoarrays and $CuMn_2O_4$-coated MnO_2 nanoarrays as major active materials and evaluated by CO and C_3H_8 oxidations, respectively. This research exhibits several features of the transition metal oxide nanoarray system and demonstrates a great potential to be applied in catalytic converters for exhaust gas treatment.

(a) Simple fabrication for industry process

The one-pot hydrothermal synthetic strategy was first revealed for coating of manganese oxide nanorod arrays on the cordierite honeycomb monolithic substrates. This synthetic strategy can in-situ grow uniform manganese oxide nanorod arrays on cordierite substrates without using mesoporous aluminum oxide as support.

(b) Material and weight saving

The manganese oxide nanorod arrays can directly bind on the substrates without applying additional binders or supports, which can reduce cost, process steps, and materials.

(c) **Enhancing catalytic performance**

The nanorod array structures provide open surfaces to reagents, which can accelerate the surface reaction and promote dynamic mass transfer to obtain a higher catalytic conversion.

(d) **Acidic and hydrothermal tolerances**

The synthesis procedures of nanoarrays and the $CuMn_2O_4$ coatings reveal the good acidic and hydrothermal tolerances of the manganese oxide nanoarrays to bear further synthetic process.

(e) **Robust structures**

Well-binding manganese oxide nanoarrays have great robustness with more than 90% coating remained after 10 h sonication.

(f) Preventing nanoparticles aggregation

Highly-ordered manganese oxide nanorod arrays can be grown on the surface of 3D cordierite substrates, even filled the holes on the ceramic walls, without any aggregation of active nanomaterials around corners causing uneven coating thickness.

(g) Promising processability

Applying additional hydrothermal reactions, various metal oxides (e.g. cobalt oxide, copper oxide, nickel oxide, manganese oxide, and copper manganese oxide) with tunable thickness and morphology can be coated upon the manganese oxide nanoarrays to promote physical and chemical properties

(h) Core supporting

As a support or template, nanoarrays benefit the $CuMn_2O_4$ nanosheet coatings to maintain the high surface area and avoid nanoparticles agglomeration.

(i) Removable active materials

All manganese oxide nanoarrays can be removed from honeycomb monoliths by simple oxalic acid etching for recycling purpose.

Appendix

Journal Articles

(1) Biswas, S.; Mullick, K.; **Chen, S.-Y.**; Gudz, A.; Carr, D. M.; Mendoza, C.; Angeles-Boza, A. M.; Suib, S. L. Facile Access to Versatile Functional Groups from Alcohol by Single Multifunctional Reusable Catalyst. *Appl. Catal., B* **2017**, *203*, 607-614.

(2) Song, W.; Ren, Z.; **Chen, S.-Y.**; Meng, Y.; Biswas, S.; Nandi, P.; Elsen, H. A.; Gao, P.-X.; Suib, S. L. Ni-and Mn-Promoted Mesoporous Co3o4: A Stable Bifunctional Catalyst with Surface-Structure-Dependent Activity for Oxygen Reduction Reaction and Oxygen Evolution Reaction. *ACS Appl. Mater. Interfaces* **2016**, *8*, 20802-20813.

(3) Pahalagedara, M. N.; Pahalagedara, L. R.; Kriz, D.; **Chen, S.-Y.**; Beaulieu, F.; Thalgaspitiya, W.; Suib, S. L. Copper Aluminum Mixed Oxide (Cual Mo) Catalyst: A Green Approach for the One-Pot Synthesis of Imines under Solvent-Free Conditions. *Appl. Catal., B* **2016**, *188*, 227-234.

(4) Miao, R.; Luo, Z.; Zhong, W.; **Chen, S.-Y.**; Jiang, T.; Dutta, B.; Nasr, Y.; Zhang, Y.; Suib, S. L. Mesoporous Tio 2 Modified with Carbon Quantum Dots as a High-Performance Visible Light Photocatalyst. *Appl. Catal., B* **2016**, *189*, 26-38.

(5) Luo, Z.; Cetegen, S. A.; Miao, R.; Jiang, T.; **Chen, S.-Y.**; Jafari, T.; Zhang, Y.; Suib, S. L. Structure–Property Relationships of Copper Modified Mesoporous Tio 2 Materials on Alkyne Homocoupling Reactions. *J. Catal.* **2016**, *338*, 94-103.

(6) **Chen, S.-Y.**; Song, W.; Lin, H.-J.; Wang, S.; Biswas, S.; Mollahosseini, M.; Kuo, C.-H.; Gao, P.-X.; Suib, S. L. Manganese Oxide Nanoarray-Based Monolithic Catalysts: Tunable Morphology and High Efficiency for Co Oxidation. *ACS Appl. Mater. Interfaces* **2016**, *8*, 7834-7842.

(7) Biswas, S.; Mullick, K.; **Chen, S.-Y.**; Kriz, D. A.; Shakil, M.; Kuo, C.-H.; Angeles-Boza, A. M.; Rossi, A. R.; Suib, S. L. Mesoporous Copper/Manganese Oxide Catalyzed Coupling of Alkynes: Evidence for Synergistic Cooperative Catalysis. *ACS Catal.* **2016**, *6*, 5069-5080.

(8) Kuo, C.-H.; Mosa, I. M.; Poyraz, A. S.; Biswas, S.; El-Sawy, A. M.; Song, W.; Luo, Z.; **Chen, S.-Y.**; Rusling, J. F.; He, J. Robust Mesoporous Manganese Oxide Catalysts for Water Oxidation. *ACS Catal.* **2015**, *5*, 1693-1699.

(9) Chen, C.-H.; Njagi, E. C.; **Chen, S.-Y.**; Horvath, D. T.; Xu, L.; Morey, A.; Mackin, C.; Joesten, R.; Suib, S. L. Structural Distortion of Molybdenum-Doped Manganese Oxide Octahedral Molecular Sieves for Enhanced Catalytic Performance. *Inorg. Chem.* **2015**, *54*, 10163-10171.

(10) Song, W.; Poyraz, A. S.; Meng, Y.; Ren, Z.; **Chen, S.-Y.**; Suib, S. L. Mesoporous Co3o4 with Controlled Porosity: Inverse Micelle Synthesis and High-Performance Catalytic Co Oxidation at− 60 C. *Chem. Mater.* **2014**, *26*, 4629-4639.

(11) Meng, Y.; Song, W.; Huang, H.; Ren, Z.; **Chen, S.-Y.**; Suib, S. L. Structure–Property Relationship of Bifunctional Mno2 Nanostructures: Highly Efficient, Ultra-Stable Electrochemical Water Oxidation and Oxygen Reduction Reaction Catalysts Identified in Alkaline Media. *J. Am. Chem. Soc.* **2014**, *136*, 11452-11464.

(12) Kuo, C.-H.; Poyraz, A. S.; Jin, L.; Meng, Y.; Pahalagedara, L.; **Chen, S.-Y.**; Kriz, D. A.; Guild, C.; Gudz, A.; Suib, S. L. Heterogeneous Acidic Tio 2 Nanoparticles for Efficient Conversion of Biomass Derived Carbohydrates. *Green Chemistry* **2014**, *16*, 785-791.

(13) Luo, Z.; Poyraz, A. S.; Kuo, C.-H.; Miao, R.; Meng, Y.; **Chen, S.-Y.**; Jiang, T.; Wenos, C.; Suib, S. L. Crystalline Mixed Phase (Anatase/Rutile) Mesoporous Titanium Dioxides for Visible Light Photocatalytic Activity. *Chem. Mater.* **2014**, *27*, 6-17.

(14) Meng, Y.; Genuino, H. C.; Kuo, C.-H.; Huang, H.; **Chen, S.-Y.**; Zhang, L.; Rossi, A.; Suib, S. L. One-Step Hydrothermal Synthesis of Manganese-Containing Mfi-Type Zeolite, Mn–Zsm-5, Characterization, and Catalytic Oxidation of Hydrocarbons. *J. Am. Chem. Soc.* **2013**, *135*, 8594-8605.

(15) Chen, Y. C.; Chou, H. H.; Tsai, M. C.; **Chen, S.- Y.**; Lin, J. T.; Yao, C. F.; Chen, K. Thieno [3, 4- B] Thiophene- Based Organic Dyes for Dye- Sensitized Solar Cells. *Chemistry–A European Journal* **2012**, *18*, 5430-5437.

(16) Chen, M.-C.; Chiang, Y.-J.; Kim, C.; Guo, Y.-J.; **Chen, S.-Y.**; Liang, Y.-J.; Huang, Y.-W.; Hu, T.-S.; Lee, G.-H.; Facchetti, A. One-Pot [1+ 1+ 1] Synthesis of Dithieno [2, 3-B: 3 ´ , 2 ´ -D] Thiophene (Dtt) and Their Functionalized Derivatives for Organic Thin-Film Transistors. *Chem. Commun.* **2009**, 1846-1848.

(17) Chen, M.-C.; Kim, C.; **Chen, S.-Y.**; Chiang, Y.-J.; Chung, M.-C.; Facchetti, A.; Marks, T. J. Functionalized Anthradithiophenes for Organic Field-Effect Transistors. *J. Mater. Chem.* **2008**, *18*, 1029-1036.

Patent applications

(1) Sheng-Yu Chen, Steven L. Suib, Pu-Xian Gao, and Junkai He "*Fabrication of manganese oxide based nanorod arrays on 3D substrates*." In press.